THESIS

LINKING RIPARIAN VEGETATION TO PRECIPITATION USING NDVI AT

YUMA PROVING GROUND, ARIZONA

Submitted by

Amy N Birtwistle

Graduate Degree Program in Ecology

In partial fulfillment of the requirements

For the Degree of Master of Science

Colorado State University

Fort Collins, Colorado

Fall 2015

Master's Committee:

    Advisor: Melinda Laituri

    Brian Bledsoe
    Jonathan Friedman

ABSTRACT

LINKING RIPARIAN VEGETATION TO PRECIPITATION USING NDVI AT

YUMA PROVING GROUND, ARIZONA

Measuring precipitation in semi-arid landscapes is important for understanding the processes

related to rainfall and run-off. However, rain gauges are sparsely distributed. Linear regressions

comparing rain gauge and RADAR precipitation estimates revealed that RADAR data is often misleading

especially for monsoon type storms. This study investigates an alternative way to map the spatial and

temporal variation of precipitation inputs along ephemeral stream channels using NDVI derived from

Landsat TM imagery. NDVI was derived on 26 pre- and post-monsoon season Landsat images across

Yuma Proving Ground (YPG) in southwestern Arizona. The mean NDVI values along ephemeral stream

channels explained 73% of the variance in precipitation totals from a nearby rain gauge for 25 monsoon

seasons. A 0.0006 increase in NDVI per day between pre- and post-monsoon season imagery was found

to indicate high precipitation inputs and possibly indicate flow events.

A second set of Landsat TM imagery were used to relate gains in NDVI during seven winter seasons

to precipitation recorded from a nearby NEXRAD radar station. The NEXRAD Stage IV radar data were

found to be more accurate during winter precipitation events when associated with rain gauge stations

(adjusted R^2: 0.81 & 0.84). High correlations were found between NDVI and precipitation at the 32, 48,

64 and 96d time intervals, though each season varied. The number of precipitation events with >5mm

at the 96d interval showed significant correlation (0.63 & 0.77) while the number of events with >10mm

had less correlation. Moreover, the combination and analysis of these two NDVI datasets revealed that

wet winters may influence the vegetation for more than four years into the future.

ACKNOWLEDGMENTS

TABLE OF CONTENTS

LIST OF TABLES

LIST OF FIGURES

CHAPTER 1: INTRODUCTION

The goal of this research is to investigate the influences of precipitation on vegetation and to use vegetation to detect precipitation inputs along ephemeral stream channels. This was done by using vegetation indices from Landsat TM time series on a semi-arid ecosystem that experiences two rainy seasons: summer monsoon and winter frontal storms. The first objective of this research was to measure the change in NDVI values between pre- and post-monsoon season Landsat 5 & 7 TM imagery for 26 years. These data have recorded the intensity and spatial distribution of plant growth (i.e. an increase in chlorophyllic content; Pettorelli et al., 2005) from monsoon season rain events at YPG and the distribution and length of droughts (i.e. little to no increase in chlorophyllic content). The second objective was to relate the response in vegetation to winter precipitation events using NEXRAD radar data and NDVI derived from Landsat 5 TM imagery. For this objective, I hypothesize that: 1) winter precipitation is highly correlated to increases in NDVI along ephemeral stream channels at YPG and 2) there is an associated lag time between the precipitation event and the NDVI response along ephemeral stream channels and this lag-time varies depending upon the amount and timing of precipitation. Furthermore, the agglomeration of both datasets may indicate climatic or environmental trends and possibly better explain the vegetation along the ephemeral stream channels at YPG and the effects of antecedent precipitation events.

This manuscript also includes Appendices A-E which supports the main objectives of this study. Appendix A documents the data used. Appendix B expands upon the methods that are described in the main document. Appendix C is devoted entirely to the statistical analysis used in comparing rain gauge and the NEXRAD and PRISM datasets. The results shown in Appendix C guided this research by evaluating the precipitation data among the monsoon and winter seasons. Appendix D illustrates the NEXRAD radar daily precipitation totals, the PRISM temperature means, and the change in NDVI using

the MTT values for each of the seven winter seasons. Appendix E documents the change in NDVI/day

across the Riparian Area Polygons for each of the 26 monsoon seasons. Appendix F is independent from

the main document and Appendices A-E. Appendix F contains a GIS tutorial created in coordination with

the Strategic Environmental Research and Development Program (SERDP) RS-1727 grant funded project

and explains the creation of various geomorphic parameters at three hierarchal scales (Reach, Valley,

and Watershed). These parameters were created at four DoD installations: Fort Irwin, Fort Bliss, Fort

Huachuca, and Yuma Proving Ground.

CHAPTER 2: LITERATURE REVIEW

Measuring precipitation in semi-arid regions is necessary for understanding the abiotic and biotic components within these landscapes. Vegetation in semi-arid landscapes has been shown to be inextricably linked to precipitation events most of which tend to be local and infrequent (Huxman et al., 2004). The changing climate further warrants improving upon the ways in which we map and monitor vegetation and precipitation in semi-arid regions. Measuring precipitation in these areas has many associated problems that cause spatial and temporal discontinuity in datasets. Long-term rain gauge data exists, but are scarce, spatially disparate and hard to find (Goodrich et al., 2008). Advances in radar technology have allowed for spatially continuous precipitation data, but they lack the historic record to observe long-term trends of multiple decades or more. In addition, the accuracy is often contingent upon the storm type and topography making these data, at times, unreliable. In water-limiting systems, where the relationship between precipitation influence and the vegetation response is robust, precipitation may indirectly be measured through satellite imagery to improve upon discontinuous datasets (Barbosa et al., 2006).

Many factors influence vegetation in arid ecosystems such as geomorphology, soil, and land use history, but the primary determinant of plant productivity in arid landscapes is the availability and timing of water (Huxman et al., 2004; Brooks et al., 2011). The vegetation within these environments often survives by small and infrequent rain events of 2mm or less (Collins et al., 2008). Higher intensity precipitation events tend to create runoff and short-lived flow events during convective monsoon season storms, but are even more infrequent (Snyder & Tartowski, 2006; Shaw & Cooper, 2007; Lichvar et al., 2009; Svoray & Karnieli, 2011). Much of the precipitation delivered from these rain events flows into the associated riparian areas, while, strong transmission losses within the ephemeral stream

channels often keep these runoff events local (Goodrich et al., 2008). Furthermore, monsoon season

precipitation can be highly variable for the Southwest region (National Weather Service, n.d.).

In contrast, precipitation delivered from winter frontal storms tends to be more widespread and

longer lasting than monsoon season events. These storm types generally contribute to higher

infiltration depths and have lower runoff potential consequently keeping much of the precipitation in

the uplands instead of the ephemeral stream channels (Snyder & Tartowski, 2006, Goodrich, et al.

2008). Winters that experience significant precipitation and moderate temperatures (often linked with

the El Niño Southern Oscillation (ENSO); Goodrich et al., 2008) can promote higher densities of

herbaceous annuals (Bowers, 2005; Kimball et al., 2010). For example, the 2004-05 winter in

southwestern Arizona experienced above average precipitation and caused herbaceous annuals to

proliferate. The greater quantities of above ground biomass fueled a fire that swept through Yuma

Proving Ground (YPG) and KOFA National Wildlife Refuge preserve in October of the following year

(Esque et al., 2013). This event demonstrates the importance of monitoring precipitation inputs and

vegetation responses of both the summer monsoon and winter frontal seasons.

Vegetation in arid climates responds to rainfall by producing biomass to such an extent that it can

be detected by satellite imagery, however, not all rain events produce enough precipitation to be

utilized by plants. The fraction of rain that is available to plants varies depending on the type, quantity,

and timing of precipitation since rain is lost to many other hydrologic processes (Brooks et al., 2011).

Small rain events (<2mm) may only influence the microbial community which aids in the production of

carbon and nitrogen that are necessary for other biological processes (Collins et. al., 2008). Some plants

will only respond to substantial rain events such as pulse events that may initiate growth, while other

vegetation will respond better to rainfall divided amongst several rain events (Ogle & Reynolds, 2004).

However, larger plants and higher vegetation densities that exist within the ephemeral stream network

are dependent on the high runoff from infrequent monsoon season storms that funnel water into these channels (Shaw & Cooper, 2008). A study in the Chihuahuan Desert found that one large rain event of 20mm per month produced more aboveground net primary productivity on a C4 grass than did four 5mm rain events distributed over a month during the 2007 and 2008 monsoon seasons (Thomey et al., 2011). Moreover, a large rain event may produce more runoff, less evaporation, and larger infiltration depths than the same amount of rain that occurs over multiple events (Reynolds et al., 2004). However, Huxman et al. (2004) found that within the Mohave, Sonoran and Chihuahuan desert regions, carbon fluxes within the microbial and vascular plants communities were positively affected by the quantity of precipitation pulses of 5mm or larger.

Furthermore, an associated lag time exists between the rain event and the production of chlorophyllic biomass (Richard & Poccard, 1998; Wang et al., 2003; Ogle & Reynolds, 2004; Svoray & Karniel, 2010). Svoray and Karniel (2010) found that the parameter that quantified the previous month's precipitation value was the most significant in explaining the response in vegetation cover through Normalized Difference Vegetation Index (NDVI) derived from SPOT XS imagery (20m resolution). Richard & Poccard (1998) and Barbosa (2004) not only found that rainfall totals for the previous 30d showed a strong linear correlation to the NDVI values in Southern Africa and Northeast Brazil, but also the previous 60d as well, suggesting that the time-lag can be upwards of 2 months. Similarly, Wang et al. (2003) used NDVI to observe a 2-4 week delay in a vegetation response following a major precipitation event in Kansas and described the precipitation to NDVI response relationship as "strong and predictable when viewed at the appropriate spatial scale." Even so, the strength and delay in response to precipitation is contingent upon the vegetation type (Ogle & Reynolds, 2004).

Remote sensing imagery is used in studies that investigate and classify vegetation spatially and temporally. Landsat 5 TM has demonstrated its efficacy through its long-term accessibility, moderate

spatial and temporal resolution, multispectral sensors, and low cost. For these reasons, Landsat 5 TM

has been widely used as a successful tool in countless research studies, such as vegetation classification

and change detection (Kerr & Ostrobsky, 2003), vegetation health (Vogelmann et al., 2009), long-term

land cover analyses (Nguyen et al., 2014; Wang et al., 2003), and ecosystem responses (Pettorelli et al.,

2005; Barbosa et al., 2006). NDVI, which uses the Red and Near Infrared (NIR) bands, has been

recognized as the most used vegetation index (Kerr & Ostrobsky, 2003; Brown et al., 2006) and can be

explicitly related to vegetation productivity (Richard & Poccard, 1998; Ichii et al., 2002; Pettorelli et al.,

2005, Brooks et al., 2011) and precipitation influences (Nicholson & Farrar, 1994; Wang et al., 2003;

Barbosa et al., 2006).

   Many studies have related precipitation data to vegetation characteristics, but usually using discrete

precipitation measurement stations (Wang et al., 2002, Huxman et al., 2004; Reynolds et al., 2004;

Goodrich et al., 2008; Svoray & Karnieli, 2010). Another option is using radar precipitation data such as

NEXRAD or PRISM data that uses a combination of radar data with local rain gauge data or other

relevant precipitation data (Brunsell & Young, 2008). Radar infrastructure has been available since the

early 1990s. Historically, many radar-only products have had problems often rendering previous

versions of the technology ineffectual, especially in the Western half of the US. More recent increases in

infrastructure (post 1997) have shown noticeable differences in the accuracy of radar data (Xie et al.,

2006). Further development of the Multisensor Precipitation Estimator (MPE) product in 2002 and

Mountain Mapper has increased the accuracy of the NEXRAD product by incorporating rain gauge data

as ground truth and bias control, especially in the western half of the US (Wang et al., 2008; Wu &

Kitzmiller, 2011). Wu & Kitzmiller (2011) used MPE products to assess the less sophisticated, radar only

precipitation products for the entire US from April 2009 to March of 2010. Even though the NEXRAD

datasets have improved dramatically since their first inception, they are still affected by spotty, mix

intensity rain events, mountainous terrain, and storm type (i.e. Orographic, Convective, or Frontal) and

should be used carefully to address these effects.

CHAPTER 3: STUDY SITE

The Department of Defense (DOD) manages approximately 35,600 km^2 of US land in the arid and semi-arid southwest harboring a higher density of threatened and endangered species than is found on land of any other federal agency (Stein et al., 2008). This research took place at the DOD installation, Yuma Proving Ground (YPG; Figure 1), located in the Sonoran Desert in southwestern Arizona. YPG encompasses 3,367km^2 of semi-arid landscape with elevations ranging from 54 to 870m (Figure 2; DEM). YPG receives an average of 95mm of precipitation a year during two separate rainy seasons - monsoon and winter season (Western Regional Climate Center, 2012). This bimodal pattern leads to scattered rain events throughout the year, allowing for a unique and diverse plant community that can support larger woody species, such as ironwood (*Olneya tesota*), paloverde (*Parkinsonia spp.*), acacia (*Acacia greggi)*, and mesquite (*Prosopis spp.*), as well as columnar cacti (Sutfin et al., 2014; NPS, n.d.).

Summer precipitation is driven by monsoon rains that originate over the Mexican Plateau located to the southeast and create localized, high intensity storms (NPS, n.d.; National Weather Service, n.d.). Large swaths of desert pavement coupled with low vegetation densities within the uplands allow rain water to move easily into stream channels (Figure 2), causing short-lived flow events. In contrast, winter precipitation originates from frontal storms typically from December to March that develop over the Pacific Ocean and tend to deliver more widespread, less intense and longer-lasting rainfall events, leading to higher infiltration rates with less runoff (Snyder & Tartowski, 2006; Stromberg et al., 2007). An increase in cloud cover coupled with cooler temperatures decreases the evapotranspiration rates allowing rain water to remain available to vegetation for a longer time. Many plant and animal species rely on the combination of these two rainy seasons that result in varying degrees of dependence. The precipitation quantities and frequencies can have profound effects on the vegetation composition over annual and decadal intervals (Snyder & Tartowski, 2006). Inter- and intra- annual climatic variability can

8
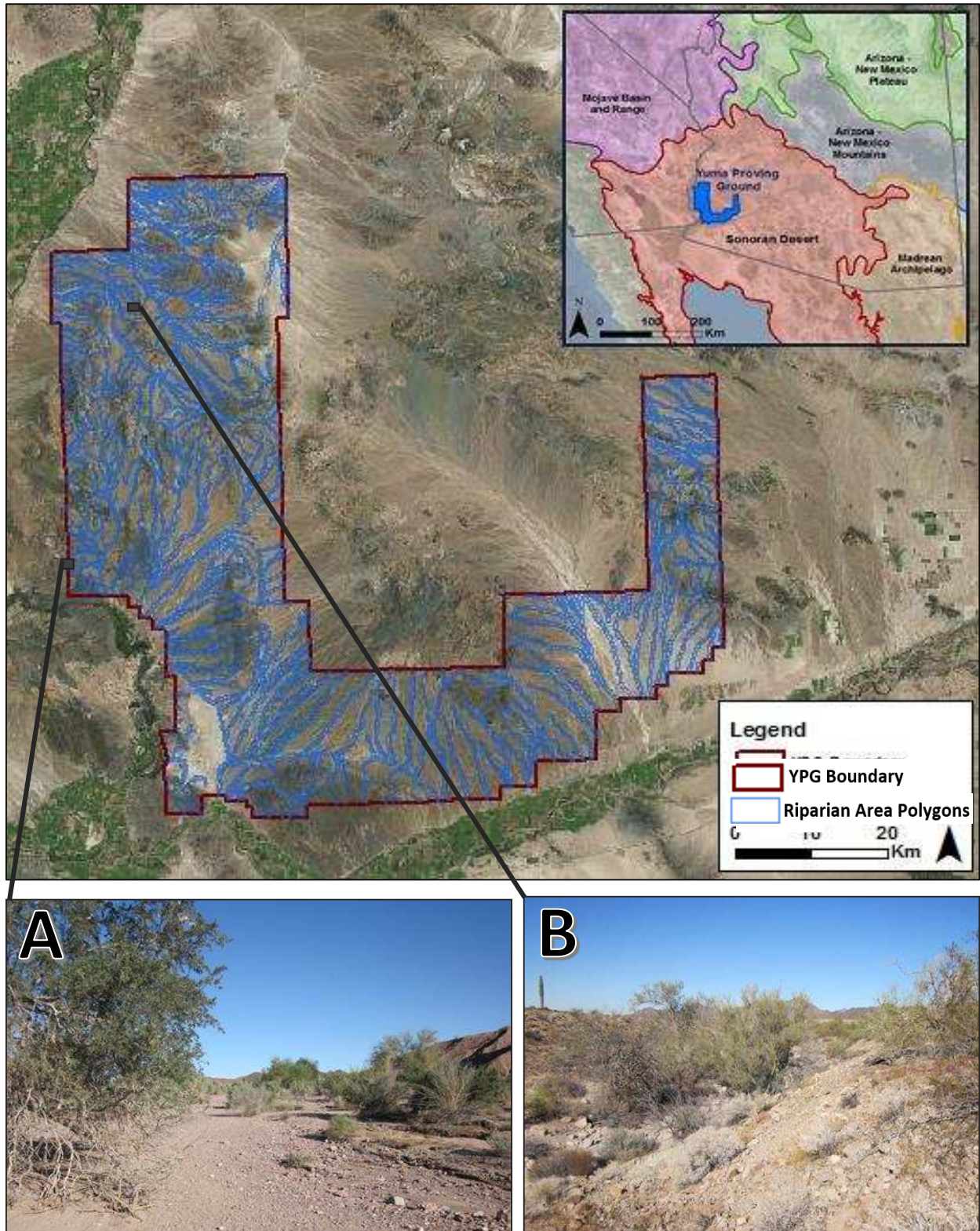
Figure 1: Location map of YPG. **Inset A:** Yuma Wash – Jan 2011 (UTMs: 11S 3664132m N, 731326m E). **Inset B:** Mohave Wash – Jan 2011 (UTMs: 11S 3698644m N, 737959m E). Pictures courtesy of Lainie Levick.

support a diverse set of vegetation, i.e. herbaceous plant seed can endure for multiple years until the

right conditions exist to initiate growth (Bowers et al., 2004) or large flood events can promote tree

recruitment and seedling success (Friedman & Lee, 2002). Furthermore, Sutfin et al. (2014) describes

five general channel types that occur within this area: piedmont headwaters, bedrock, bedrock with

alluvium, incised alluvium, and braided channel types. These stream types can be differentiated by the

channel geometry, width-to-depth ratio, slope, stream power, and shear stress and thus can have an

underlying influence on the vegetation within this area (Sutfin et al., 2014).
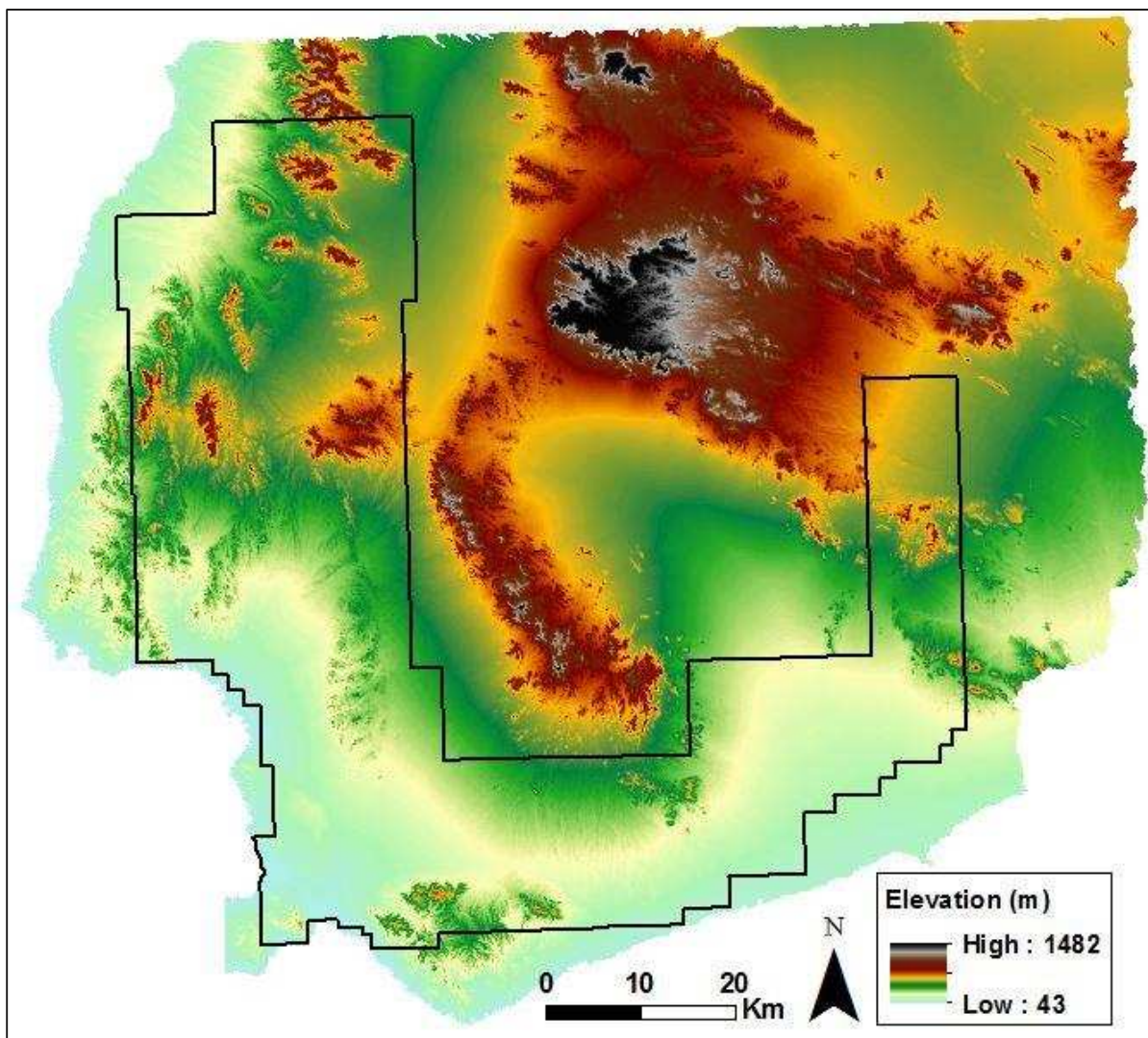
Figure 2: 10m DEM of YPG.

The following sections describe the methods used in creating this analysis and are illustrated in

Figure 3. The first phase modified the data to be used in this study (Figure 3-A). This involved deriving

the Riparian Area Polygons (RAPs) from the NHDPlus Version 2 dataset. The next step required

processing the NDVI from the Landsat images, subtracting paired NDVI scenes (ΔNDVI-S), followed by

extracting the mean NDVI value of the top ten percent of pixel values (MTT) within each RAP unit for

each ΔNDVI-S. The second phase (Figure 3-B) investigated the precipitation datasets using linear

regressions to assess the validity of NEXRAD radar and PRISM data as a proxy for precipitation within

each rainy season. The data was then organized between the monsoon and winter season's based on

the linear regressions from Figure 3B and the monsoon dataset was compared to two known flow

events (Figure 3-C). For the Results and Conclusions (Figure 3-D), mean and coefficient of variation (CV)

were used to determine the spatial uniformity and temporal variability of the changes in monsoon

season NDVI over the 26 year study period. Spearman's correlation analyses were used to relate winter

precipitation measured via radar instruments to the changes in NDVI over corresponding localities and

timescales. A final analysis was created that combined the monsoon and winter season analyses. These

methods are described in more detail in Appendices B & C. A list of abbreviations are shown in Table 1.

Table 1: List of Abbreviations.

4.1 Riparian Area Polygons (RAPs)

RAPs were derived from the NHDPlus Version 2

flowlines for the Lower Colorado Vector Processing Unit

(www.horizon-systems.com/NHDPlus/ NHDPlusV2_15

Change in NDVI Scene (post – pre) for each rainy season	ΔNDVI-S
Mean of Top 10% (NDVI) per RAP	MTT
Near Infra-Red Band (Band 4)	NIR
Riparian Area Polygon	RAP
Yuma Proving Ground	YPG

.php). The NHDPlus Version 2 flowline layer was split into 2,843 reaches at approximately 1km or

smaller lengths (Levick et al., 2015). Each reach was inundated to a height of 3m using a 10m DEM and

the HGVC (Hydro-Geomorphic Valley Classification) extension tool (Carlson E.A., 2009) in ESRI ArcMap

10.2, and the inundated area was mapped to a maximum distance of 200m from the original flowline.

Each RAP (Figure 1: blue polygons) was labelled with a unique identifier.
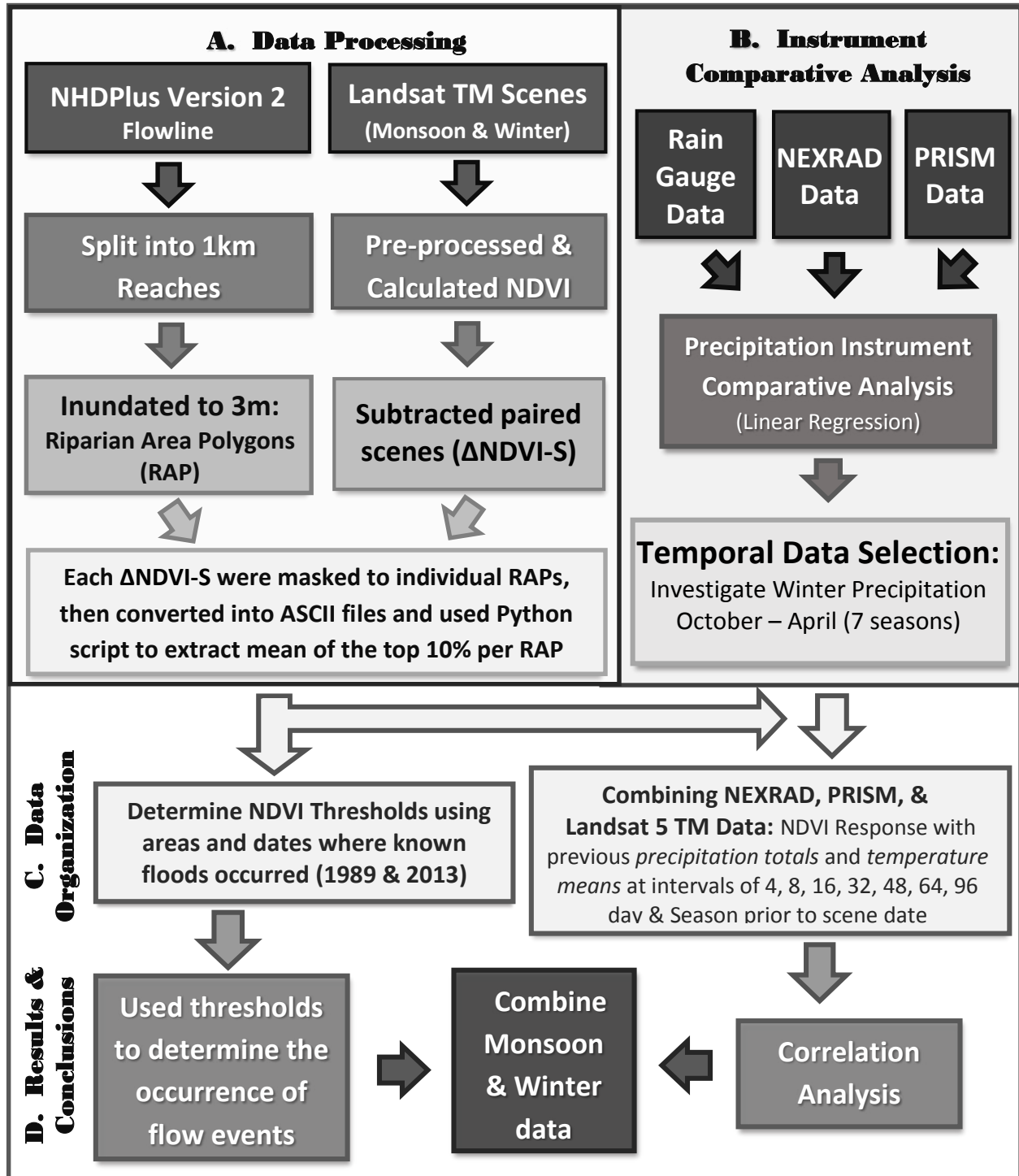
Figure 3: Flow Chart showing the Methods used and are segmented into four steps A, B, C, and D.

4.2 Landsat TM

Landsat TM scenes from Path 38, Row 37 were acquired through USGS's GlobeVis website

(http://glovis.usgs.gov/) for pre- and post-monsoon season dates for years 1986 – 2011 (26 total) and

from October to April for winters from 2004-05 to 2010-11 (seven total). In all cases, Landsat 5 TM

images were selected except during 2000–02 monsoon seasons where Landsat 7 TM provided superior

images. Additional scenes were acquired for the 1989 (Landsat 5 TM) and 2013 (Landsat 8 TM)

monsoon seasons to relate the change in NDVI to recorded flood events. Acquisition dates and

identification codes for each scene are documented in Appendix A.

Each Landsat scene underwent pre-processing in ENVI 5.0 where *Radiometric Calibration for*

Reflectance and *Dark Object Subtraction* were executed on all scenes. Each Landsat scene was masked

to the study area where the pixels were spatially aligned and the cell size was reduced to 5m^2 to ensure

that smaller RAPs would capture all NDVI values. NDVI was calculated for individual scenes using the

standard equation [(NIR – RED) / (NIR + RED)] in ARCMap 10.2. The base scene for each of the 26

monsoon seasons was chosen during June or July, with one exception in May (1996). The base scene

selected for each of the seven winter seasons was captured prior to the winter season in either

September or October. The monsoon season NDVI base scene was subtracted from the post-monsoon

season NDVI imagery of that year and the base winter NDVI scene was subtracted from all subsequent

winter scenes for each of the seven winter seasons. This created the change in NDVI scene for each pair

of dates (hereafter referred to as the ΔNDVI-S) where positive values indicate a gain in NDVI. The

monsoon season ΔNDVI-S results are located in Figure 7 in section 5.1. Further details are described in

Appendix B.

4.3 Mean of the Top Ten Percent (MTT) values

The quantity of change in NDVI of the monsoon and winter ΔNDVI-S were extracted at each RAP to determine the increase in plant biomass during the selected rainy seasons. This was done by taking the mean value of the pixels above the 90th percentile. The 90th percentile was chosen to estimate the increase in NDVI because the RAP units typically incorporate 50 to 500, 30x30m pixels with many non-vegetative pixels associated with them. Taking the mean of all pixels within the RAP unit would be meaningless and using the maximum value would misrepresent the increase in NDVI, therefore the mean value of the top ten percent was used. This was executed by clipping the individual 2,843 RAP units to every ΔNDVI-S. After a single ΔNDVI-S image was masked to the 2,843 individual RAPs, the newly created RAP raster images were changed into ASCII text files. A python script (Appendix B) was used to extract the NDVI values from each RAP ASCII text file, then calculate the Mean value of the Top Ten percent (MTT). The python code aggregated each MTT value for the 2,843 RAPs into a single CSV file based off the ΔNDVI-S used (Figure 4).
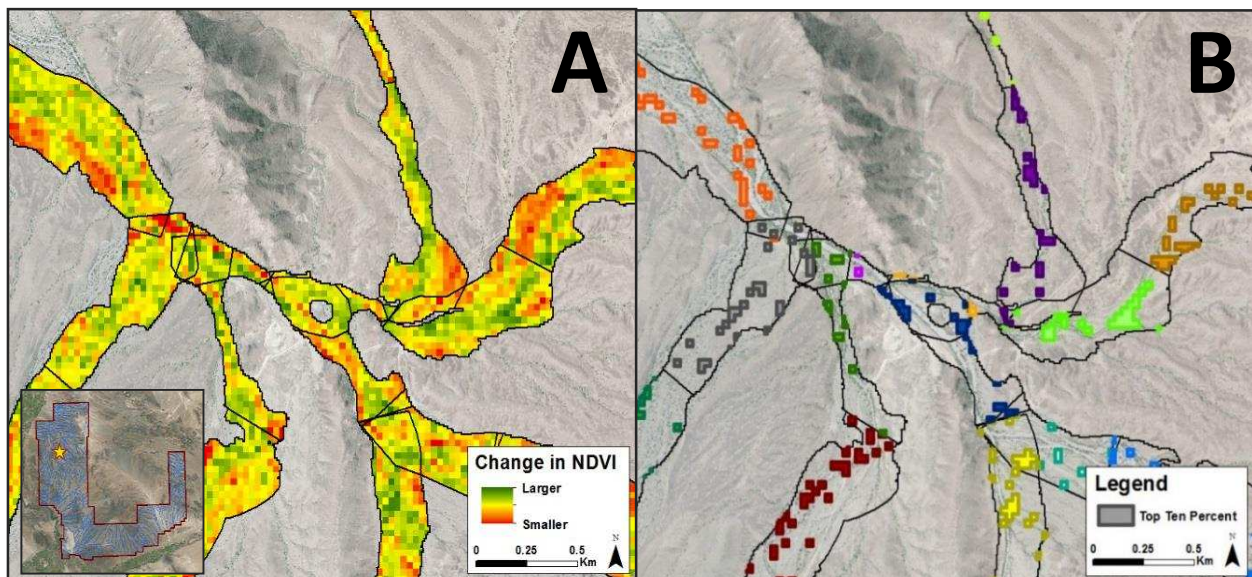
Figure 4: These figures demonstrate the methods for extracting the MTT NDVI values within each RAP. For each ΔNDVI-S, each RAP was extracted separately by using individual RAP shapefiles in ArcMap 10.2 (shown in Figure A), then converted into an ASCII text file that contains every pixel value within the RAP. The values of the pixels representing the Top 10% are depicted in Figure B.

The MTT values were further manipulated on the monsoon season dataset to calculate the slope (change in NDVI per day) using the total number of days between pre- and post-monsoon season imagery. This was done on each RAP unit for each ΔNDVI-S during the monsoon season. Coefficient of variation (CV) was also calculated for each of the 2,843 RAPs by taking the standard deviation of the 26 years of MTT values then dividing it by the mean. Two flood events were recorded within the study area during the 1989 and 2013 monsoon seasons. Nearby RAP units (n=52 and 10, respectively) were isolated and the median of the MTT values were calculated for several ΔNDVI-S's bracketing these events.

4.4 Rain Gauge Data

Rain gauge data were acquired through the National Weather Service Forecast Center (http://www.wrh.noaa. gov/twc/monsoon/monsoon_yum.php) for Yuma, Arizona from 1876 to 2014 and GHCN data were attained through the NOAA National Climatic Data Center website (http://www.ncdc .noaa.gov /data-access/land-based-station-data) at six locations within and surrounding YPG with
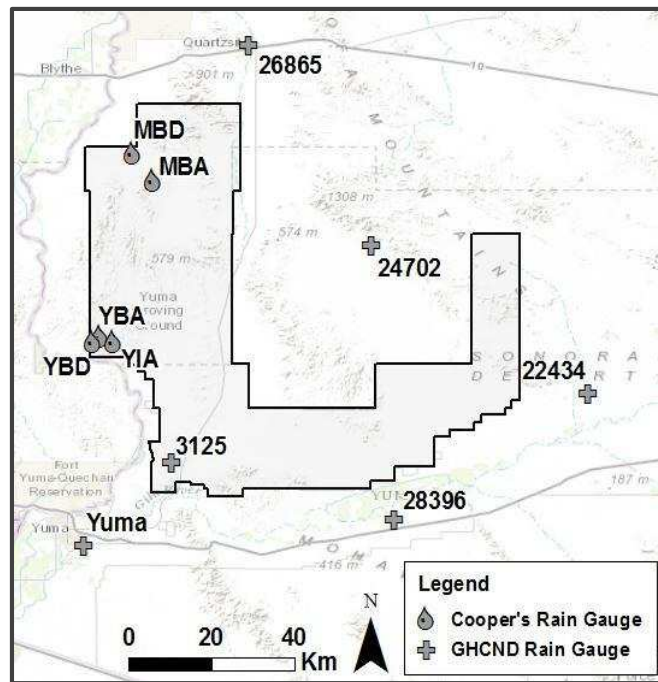
Figure 5: Rain gauges distributed through YPG and the surrounding area.

scattered coverage as early as 1909 (Figure 5; crosses). A second group of rain gauges were acquired for Yuma (YBA, YBD and YIA) and Mohave Washes (MBD and MBA) (Figure 5; drops) and measured rain events from 2011 to 2013 (Faulconer, 2015). The instruments used at Yuma and Mohave Washes were a TE 525 Tipping Bucket rain gauge system at 0.254mm per tip rate.

15

4.5 Radar Data

NEXRAD data are a type of Doppler radar that measure precipitation amounts from fixed stations located throughout the US and estimates precipitation up to a range of 230km from each station (Fulton, 2002). Radar emits a signal that increases in altitude with increasing distance causing the radar station to sample higher altitudes that do not necessarily represent what is occurring at the surface. Previous versions of NEXRAD (Stage II & III) data led to the creation of the Multisensor Precipitation Estimator (MPE) that combines Stage II data and independent rain gauge data with satellite precipitation data (GOES Satellite imagery) to produce more accurate precipitation estimates by minimizing local bias errors and enhancing coverage by decreasing beam blockage and reducing spatial uniformity with rain gauge data (Fulton, 2002). Mountain Mapper is similar to MPE, but is used in areas that are affected by orographic precipitation, commonly in the western US (Schaake et al., 2004). NEXRAD MPE and Mountain Mapper products are processed through the National Weather Service: River Forecast Centers since 2004. The precipitation data are delivered in the Hydrologic Rainfall Analysis Project (HRAP) grid at a 16km^2 resolution in inches.

The NEXRAD station YUX covers YPG and resides southwest of the boundary (Appendix C, Figure 22). The rain gauge sites for Yuma Wash were located approximately 80km away, while Mohave Wash rain gauge sites reside about 125km away. The NEXRAD data were downloaded from the National Weather Service website (water.weather.gov/precip/p_download_new) by using a python script created by Mehmet Ercan (http://mehmetbercan.com/scripts/scriptsGIS.html) that downloads and clips the NEXRAD data in Esri's ArcMap. It was further processed into tabular format of daily precipitation totals per each virtual grid point beginning on January 2, 2005.

Since the NEXRAD data that were used began on January 2, 2005, during a particularly wet winter season, PRISM precipitation data were used to estimate the rainfall prior to January 2, 2005 for the

2004-05 winter season. PRISM precipitation totals and temperature mean data were downloaded

through the PRISM CLIMATE GROUP from October 2004 through April 2011 in daily ASCII files for the

contiguous US (http://www.prism.oregonstate.edu). The resolution is identical to the NEXRAD data

($16km^2$).

4.6 Precipitation Instrument Comparative Analysis

The precipitation instrument comparative analysis was executed on the rain data initially to

determine the direction of the primary analyses and therefore the methods and results are documented

here. Rain gauge data were compiled with NEXRAD and PRISM precipitation data to assess the quality

of these datasets. The three rain gauge sites at Yuma Wash and the two rain gauge sites at Mohave

Wash (Figure 5), were used to evaluate the radar derived data. Inverse Distance Weighting was applied

to the three or four closest NEXRAD and PRISM grid center points to estimate the two observed

precipitation datasets at each of the five rain gauge sites. Linear regressions performed in RStudio 3.1.1

(R Core Team, 2014) on the NEXRAD and Rain Gauge datasets for years 2011-13, showed a stronger

relation with winter precipitation (Table 2; adjusted R^2: 0.81 & 0.84) than with annual precipitation

(Table 2; adjusted R^2: 0.18 & 0.34).   Moreover, the slopes of the linear regressions showed similar

results. Yearly data showed that NEXRAD radar data greatly underestimated the actual rainfall, where

slopes for Yuma and Mohave washes were 0.15 and 0.38, respectively (Table 2). Slopes configured from

Table 2: Linear regression results relating to the various daily precipitation total data.

	Site	Rain Events	Rain Gauge vs NEXRAD		Rain Gauge vs PRISM		NEXRAD vs PRISM	
			Mean Slope	Mean Adj R^2	Mean Slope	Mean Adj R^2	Mean Slope	Mean Adj R^2
Year	Yuma Wash	215	0.15	0.18	0.17	0.21	**1.00**	**0.64**
Year	Mohave Wash	162	0.38	0.34	--	--	--	--
Winter	Yuma Wash	88	**0.56**	**0.81**	**0.60**	**0.69**	--	--
Winter	Mohave Wash	69	**0.63**	**0.84**	--	--	--	--

the linear regressions on the winter data alone showed improvements (Yuma: 0.56 and Mohave: 0.63; Table 2), however, these data indicated that NEXRAD radar data generally underestimates the actual rainfall by approximately 40%. A similar trend followed for the PRISM datasets when compared to the Yuma Wash rain gauge sites (winter adjusted R^2: 0.69 and year adjusted R^2: 0.17). Linear regressions calculated on yearly data from 2005-13 combining the NEXRAD and PRISM datasets found that the average adjusted R^2 value was 0.64 for all years with a slope of 1.00. Because the NEXRAD data uses Greenwich Mean Time, any precipitation event that occurred after 6 pm at YPG was recorded the day after. Consequently, the NEXRAD data were moved to the day after when appropriate. PRISM data saw similar discrepancies, but not as frequently. For more detail on these analyses, refer to Appendix C.

4.7 Combining NDVI and Precip/Temp Interval Data

Since the linear regression calculations concluded that NEXRAD radar data is more accurate during winter than summer, correlation analyses using NEXRAD were limited to the winter. Precipitation, mean temperature data, and change in NDVI were organized at YPG starting in October and going through early May for each of the seven winter seasons. The precipitation data used NEXRAD daily observation data for all years except from October 1, 2004 to January 1, 2005 where PRISM precipitation daily totals were used. All temperature data came from the PRISM datasets and changes in NDVI data were derived from the Landsat imagery by taking the MTT values at every RAP unit for every ΔNDVI-S. The total precipitation and temperature mean data were organized in the previous 4, 8, 16, 32, 48, 64, and 96 day intervals as well as a season interval for every Landsat winter scene date. Earlier winter scenes had null values in the larger day interval data. Number of days with precipitation totals above 5mm and 10mm were totaled for every winter Landsat scene for the previous 32, 48, and 96 day intervals. To better investigate the time-lag, precipitation amounts were totaled between two select dates for the intervals: 8-16, 16-32, 16-48, 32-64, and 48-96 days prior to the more recent Landsat scene capture date.

5.1 Monsoon Season

The Sonoran Desert encounters a monsoon season usually between July and September that tends to experience high intensity thunderstorms. Though infrequent, these storms can deliver significant quantities of precipitation into the ephemeral stream channels and are likely to be spatially and temporally irregular where gaps between storms may span many years. However, the true patchiness of monsoon type storms is not well understood due to spatially and temporally inadequate datasets (usually from sparse rain gauge data or inaccurate RADAR data; Wang et al., 2008). The response in NDVI to precipitation may indirectly prove to be superior and more reliable at investigating these patterns than the aforementioned data types. The boxplots from Figure 6 and the ΔNDVI-S plates from Figure 7 shows the changes in NDVI at YPG for each monsoon season from 1986 to 2011. The strength of these changes as well as the spatial variability indicates the spatial and temporal scales at which monsoon season storms influence this landscape.
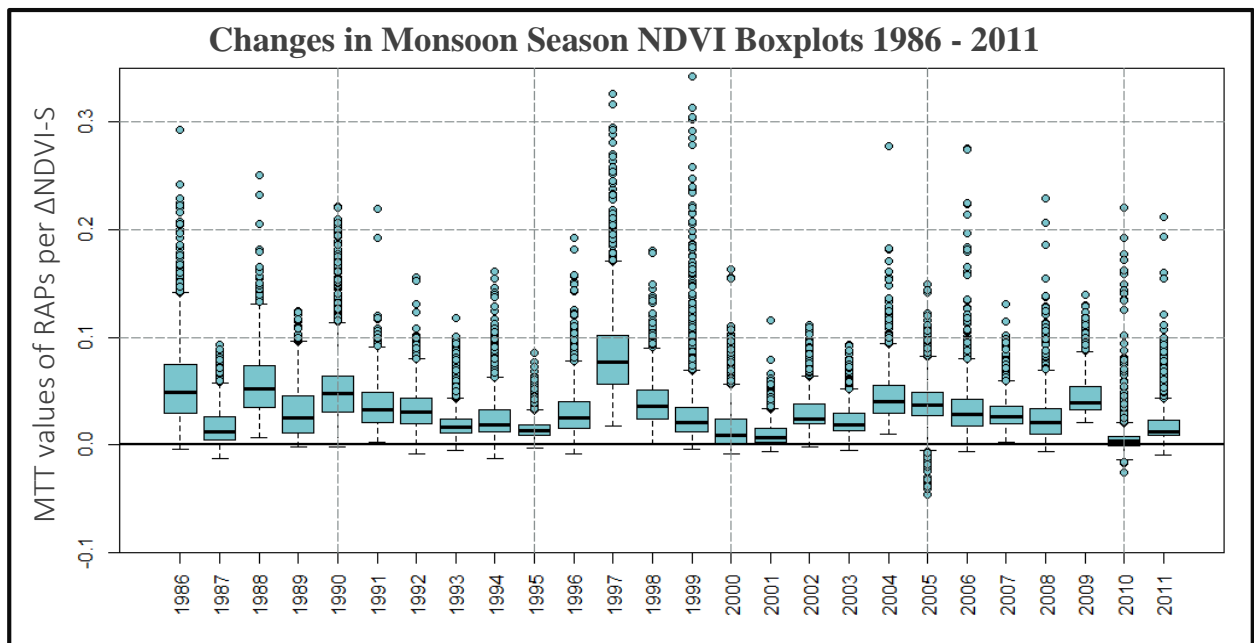
Figure 6: Boxplots for ΔNDVI-S along the 2,843 RAPs for all monsoon season study years.
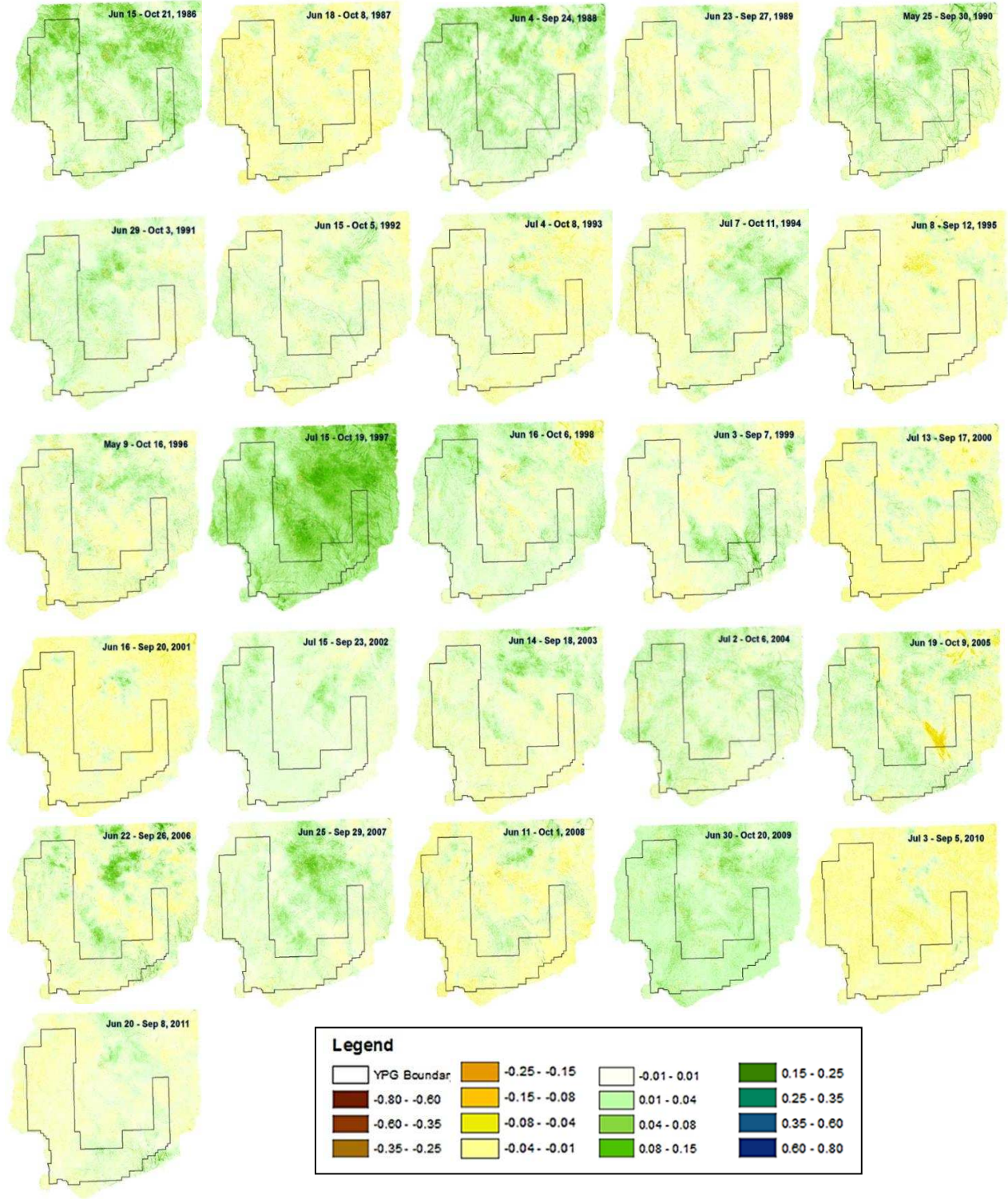
Figure 7: Change in NDVI scenes (ΔNDVI-S) for monsoon season years 1986 to 2011.

The boxplots from Figure 6 and ΔNDVI-S plates from Figure 7 indicate that 1986, 1988, 1990 and 1997 have higher than average changes in NDVI with median MTT values for all RAP units at 0.049, 0.052, 0.047, and 0.077, respectively, with the 1997 monsoon season showing the strongest overall NDVI signal. The significant MTT value seen in 1997 is likely due to the strong and rapid increase in El Niño conditions that occurred prior to the 1997 monsoon season (www.pmel.noaa.gov/tao/elnino/faq.html#deal). However, 1997 did not have the maximum MTT value for this dataset. The maximum MTT value among all RAP units occurred during the 1999 monsoon season at an increase in MTT of 0.342 in the southwestern portion of YPG. In contrast, the MTT values from the 2005 monsoon season (Figure 6) shows a decrease in NDVI along several RAP units resulting from a fire that burned through YPG and the KOFA National Wildlife Refuge preserve to the north (Esque et al., 2013). The minimum MTT value during this year is -0.046 and serves as the lower limit of the 1986-2011 dataset. A strong negative MTT change (< -0.02) is atypical during the wet season and when observed, it is likely the result of a significant land cover change. Monsoon season 2010 saw few changes with some negative MTT values. Unfortunately, this is likely the relic of an early post-monsoon season image of September 5, 2010. A better choice would have been a later image, but later scenes had considerable cloud cover over the study area. What is apparent from the cloud-free portions of the October 7, 2010 images is that that the monsoon season appears to be more similar to other monsoon seasons than is depicted from the September 5, 2010 image. This example illustrates the importance of selecting the best available dates while considering the cost of cloud cover versus the impact of change in NDVI. Other years that may be inflicted by earlier than desired post-monsoon season imagery include 1995, 2001, 2003, and 2011 (Figure 6).

5.1.1 Testing the MTT values

The MTT values from 52 RAP units that surrounded the NCDC rain gauge 3125 were associated to the precipitation record at the rain gauge site for each monsoon season between 1986 and 2011, excluding 2009 when the rain gauge lacked data (Figure 8). Using RStudio 3.1.1 (R Core Team, 2014), a linear regression was completed over the 25 monsoon seasons using the precipitation and NDVI data. Precipitation was totaled between the pre- and post-monsoon season dates for each season, however to account for a time-lag period between rainfall and vegetation growth, precipitation that was recorded within the 12d prior to the post-monsoon season date were excluded. The adjusted R-squared value determined from these data equaled 0.73 suggesting that the MTT values are a good indicator of precipitation inputs. Furthermore, the slope of the linear regression amounted to 0.0007, thus suggesting that 10mm of rainfall will increase the MTT values by roughly 0.007 (Figure 8).
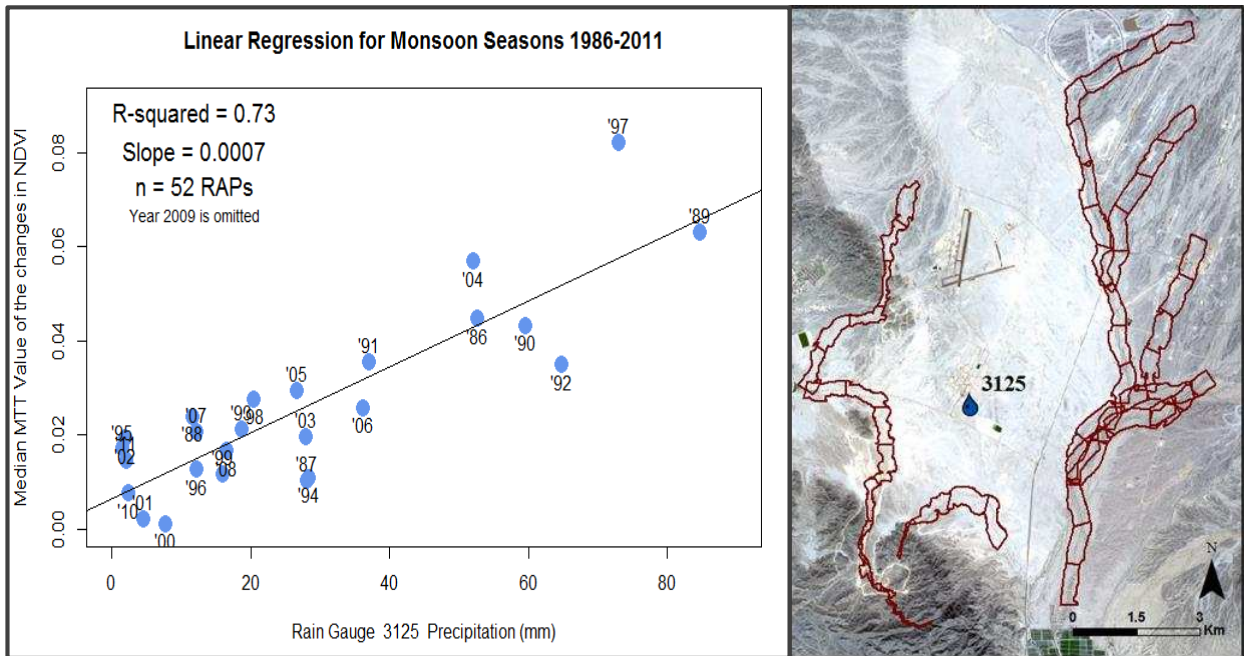
Figure 8: Linear regression comparing the total precipitation during monsoon seasons 1986 - 2011 at rain gauge 3125 to nearby RAPs. The median MTT value of the 52 RAPs were taken for every ∆NDVI-S and were regressed on the precipitation totals at the rain gauge. R^2 was found to be 0.73 with a slope of 0.0007.

5.1.2 Relating the MTT values to Precipitation

There have been many studies that have established the robust relationships between precipitation, plant productivity, and NDVI (Nicholson & Farrar, 1994; Wang et al., 2003; Pettorelli et al., 2005; Barbosa et al., 2006; Brooks et al., 2011). In this research, the Linear Regression shown in 5.1.1 further documents the strong relationship between the MTT values used here to precipitation. Additional parameters that may better explain the relation between monsoon season precipitation and NDVI are precipitation timing and intensity, temperature, and channel location. A negative change indicates that little or no rainfall has fallen and/or that persistent higher temperatures have caused noticeable decreases in plant productivity. A zero or near zero change indicates either that few rainfall events have occurred or that vegetation does not persist in the pixelated area. A positive change indicates that rainfall contributed to an increase in plant productivity and a large positive increase in NDVI suggests that the riparian area was not only influence by a rain event, but also by a flow event that allowed more rainfall to accumulate within the riparian areas triggering considerable increases in vegetation growth.

The rain gauge data acquired from the Strategic Environmental Research and Development Program (SERDP) RS-1725 grant funded project at Mohave Wash (Faulconer, 2015) and NOAA's GHCN rain gauge 3125 (Figure 5), has allowed a more detailed investigation into the change in NDVI following two flow events (Figures 9 & 10). During the summer of 1989, the GHCN 3125 rain gauge recorded a 61mm rain event on August 9 (Figure 9). Although it is unclear how much precipitation occurred in the surrounding area, the strong change in NDVI following this event indicated this event to be fairly large. It can also be assumed that even though no flow data were measured during this event, a 61mm monsoon rain event would surpass upland infiltration rates and produce runoff.

The same pre-monsoon season scene used for the 1989 monsoon season analysis was used here (June 23, 1989) to track the changes in NDVI during this season. The 52 RAPs that were used in the

23

linear regression in 5.1.1 were used here to measure the increase in NDVI following this large rain event

(Figure 9: Landsat Plates). The MTT values documented a sudden increase in NDVI 18 days following the

flow event (Figure 9; ΔNDVI/day graph). The Landsat scene taken on July 25, 1989 prior to the rain

event, documented a slight increase (0.0027) in the median MTT values for the 52 RAP units. However,

the median of the MTT values for the August 26, 1989 ΔNDVI-S increased by 0.057, increasing the slope

to 0.0017 ΔNDVI/day between July 25 and August 26, 1989. This is seen from the two graphs in Figure

9. Following August 26, 1989, the increase in NDVI declined substantially to 0.0002 ΔNDVI/day for the

next month and 0.0003 ΔNDVI/day over the following month.

When relating these data to the entire monsoon season, the strong change in NDVI following a flow

event is greatly diminished (0.0006 ΔNDVI/day increase between June 23 and Oct 29, 1989; Figure 9).

Even though the increase is not as substantial when considering the entire season, it is still likely to be

strong enough to indicate that a flow event has occurred during that season. From these data, I suggest

that an increase in 0.0006 ΔNDVI/day or greater indicates a high probability that flow occurred along

RAP units or if not flow then likely the RAP units were influenced by multiple and also significant rain

events.

Similar results are seen during the 2013 flow event at Mohave Wash (Figure 10) using the median

MTT values of the 10 closest RAP units. The rain gauge recorded a 52.6mm rain event on September 7,

2013 with smaller rain events occurring before and following the 52.6mm rain event. Furthermore, field

observations within the following month indicated flow had occurred within the stream channel (Joshua

Faulconer, personal communication). Unlike the 1989 event, the increase in NDVI within the

surrounding area, suggests that this event was considerably smaller and therefore only 10 RAPs were

used to show the change in NDVI. Because several other rain events were recorded at the Mohave

Wash rain gauge during the 2013 monsoon season, the NDVI showed a fairly steady increase (Figure 10;
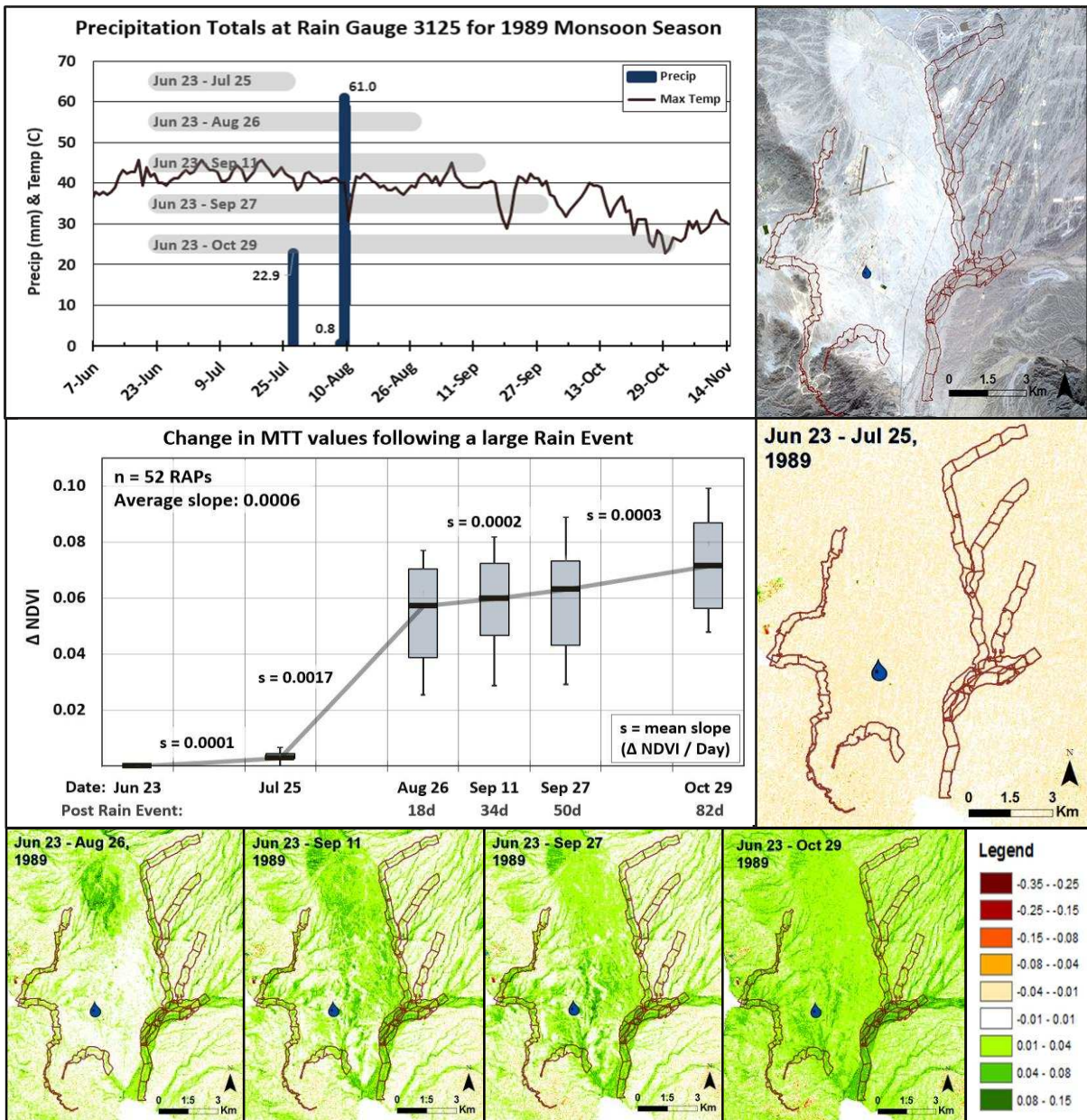
Figure 9: The 1989 flow event and NDVI Comparison. The GHCN 3125 rain gauge recorded a large rain event (61mm) on August 9, 1989. Considerable increase in NDVI over a spatially large area indicates that this rain event covered a relatively large region (radius >15km). Changes in NDVI were recorded for 52 reaches over the 1989 monsoon season. The largest change in NDVI occurred within the first 18d following the flood event (s=0.0017). The average slope between Jun 23 and Oct 29 (128d) is 0.0006.
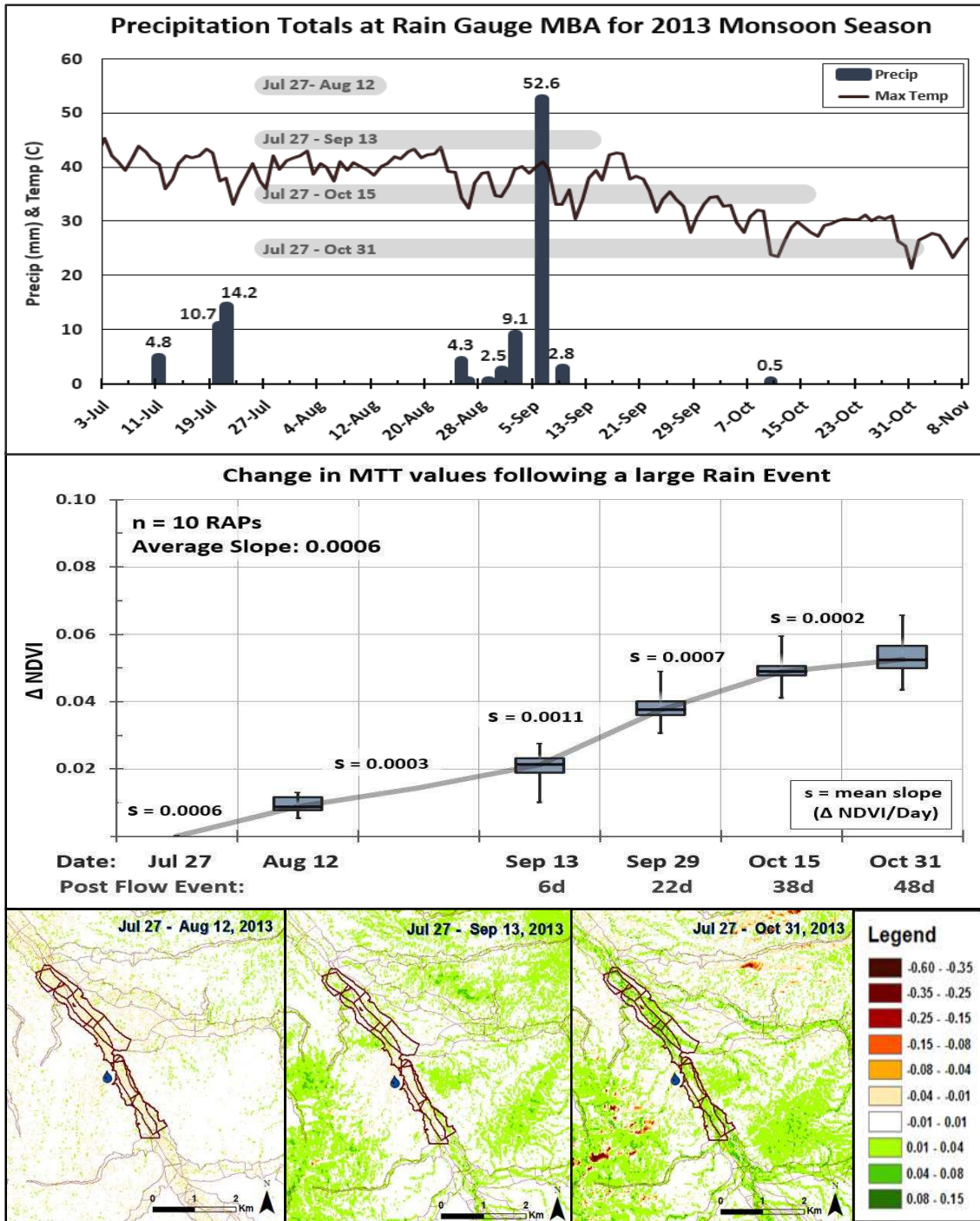
Figure 10: Mohave Wash (2013) flow event and NDVI Comparison. Rain gauge data recorded a large quantity of precipitation on September 7, 2013 (52.6mm), soil moisture data and field observations in October of 2013 indicated a flow event (re-working of channel and distribution of debris). Following this event, the largest gain in NDVI values were seen between 6 and 22 days following the event (slope = 0.0011) and decreased to 0.0007 after 38d. The average slope between Jul 27 and Oct 31 (96d) is 0.0006. These reaches have a Contributing Area of approximately 170km^2.

ΔNDVI/day graph). Between September 13 and 29 (6 to 22d following the flow event), the rate of increase rose from 0.0003 to 0.0011 ΔNDVI/day. Between September 29 and October 15 (22 to 38d following the event), the ΔNDVI/day decreased to 0.0007. After October 15 and 38 days following the flow event, the ΔNDVI/day decreases considerably to 0.0002. When averaging the slopes across the entire monsoon season, an average

Table 3: Number of days between pre- and post-monsoon season Landsat scenes for each year.

# Days	Tally	Years
64	1	2010
80	1	2011
96	14	1989, 1991, 1993-95, 1997, 1999-04, 2006-07
112	7	1987-88, 1992, 1998, 2005, 2008-09
128	2	1986, 1990
160	1	1996

slope of 0.0006 ΔNDVI/day is seen and is identical to the 1989 data. Since the 2013 flow event showed several other rain events that likely facilitated the overall increase in slope to 0.0006, this could denote that the threshold for indicating a flow event with high certainty may actually be lower than 0.0006 ΔNDVI/day.

Slopes were calculated for all RAP units during the 26 Monsoon seasons (Figure 11). For this analysis, the ideal number of days between scenes is either 96 or 112 and accounts for 21 monsoon seasons (Table 3). Figure 11 shows the percentage of slopes that is above the 0.0006 ΔNDVI/day threshold with the largest percentage occurring in 1997 with over 73% of the RAPs surpassing the 0.0006 threshold. This suggests that not only did a significant rain event or events occurred, but the coverage was more uniform than is typical during the monsoon season. Other notable years with higher percentages were 1998 at 31%, 1986 at 23%, 2004 at 21%, 1989 and 1990 at 13%, 2009 at 12% and 1999 at 11% (Figure 11).

The slopes of the MTT values for each RAP were averaged over the 26 monsoon seasons and are displayed in Figure 12.A. Inclusion of the 2010 monsoon season that had an early post-monsoon season imagery, did not vary these results considerably. RAP units with greater average slopes indicates that these reaches had more frequent increases in NDVI, suggesting that they received more monsoon season
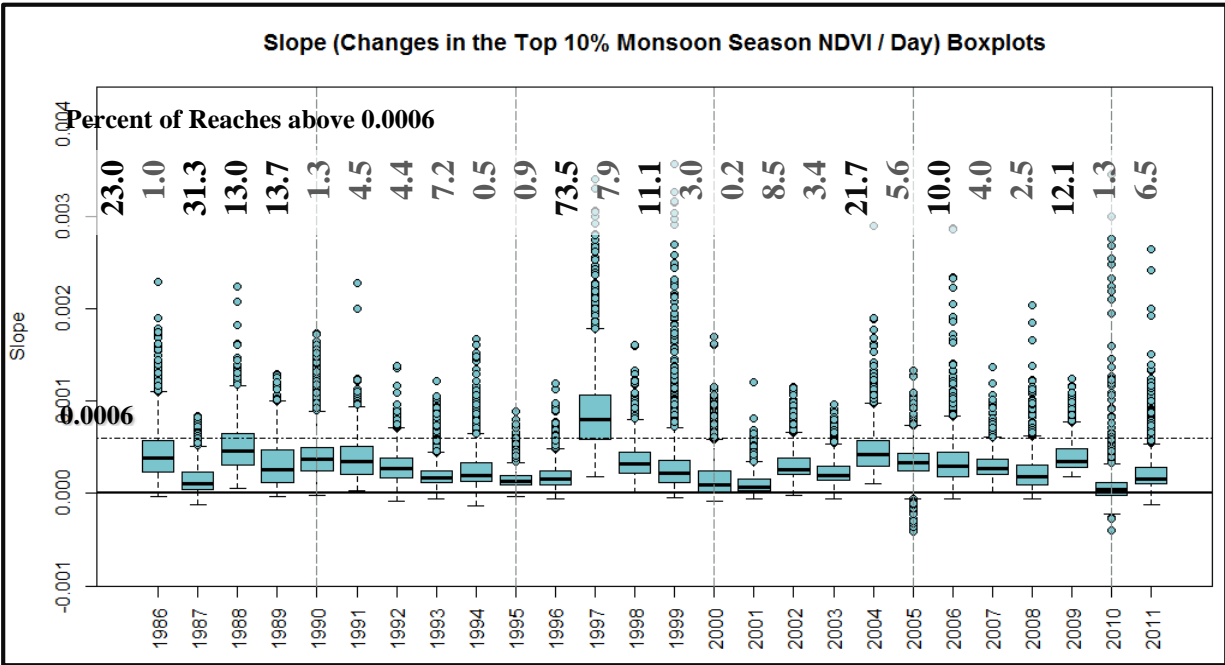
Figure 11: Boxplots of the Slope of each RAP unit over the 26 monsoon seasons. The 0.0006 ΔNDVI/day cutoff and percentages along the top of the figure represents the percentage of RAPs in which flow was likely during each year.

precipitation over the 1986 to 2011 study period. Of the 2,751km of stream channels at YPG, approximately 8% have an average slope between 0.0001-0.0002, 43% between 0.0002-0.0003, 36% between 0.0003-0.0004, 10% between 0.0004-0.0005, and 3% between 0.0005-0.0010. Figure 12.A shows that the mountainous terrain located in the western portions of YPG (refer to Figure 2; DEM), tend to have on average greater changes in NDVI/day within the mountains than in flatter terrain and also shows that as distance increases from the mountain ranges, slopes generally decreasing. This is expected given that these channels suffer from high transmission losses (Goodrich et al., 2008). Slopes of individual ΔNDVI-S are found in Appendix E.

The CV among RAPs for the 26 year study period are also shown in Figure 12.B. The CV explains the variability of changes in NDVI at YPG. Lower CV values (CV>1) suggest that there have been less changes and higher values (CV<1) imply that the RAPs experience greater changes in NDVI. From Figure 12.B, it is apparent that the eastern portions of YPG have experienced more variability than the western portions.

28
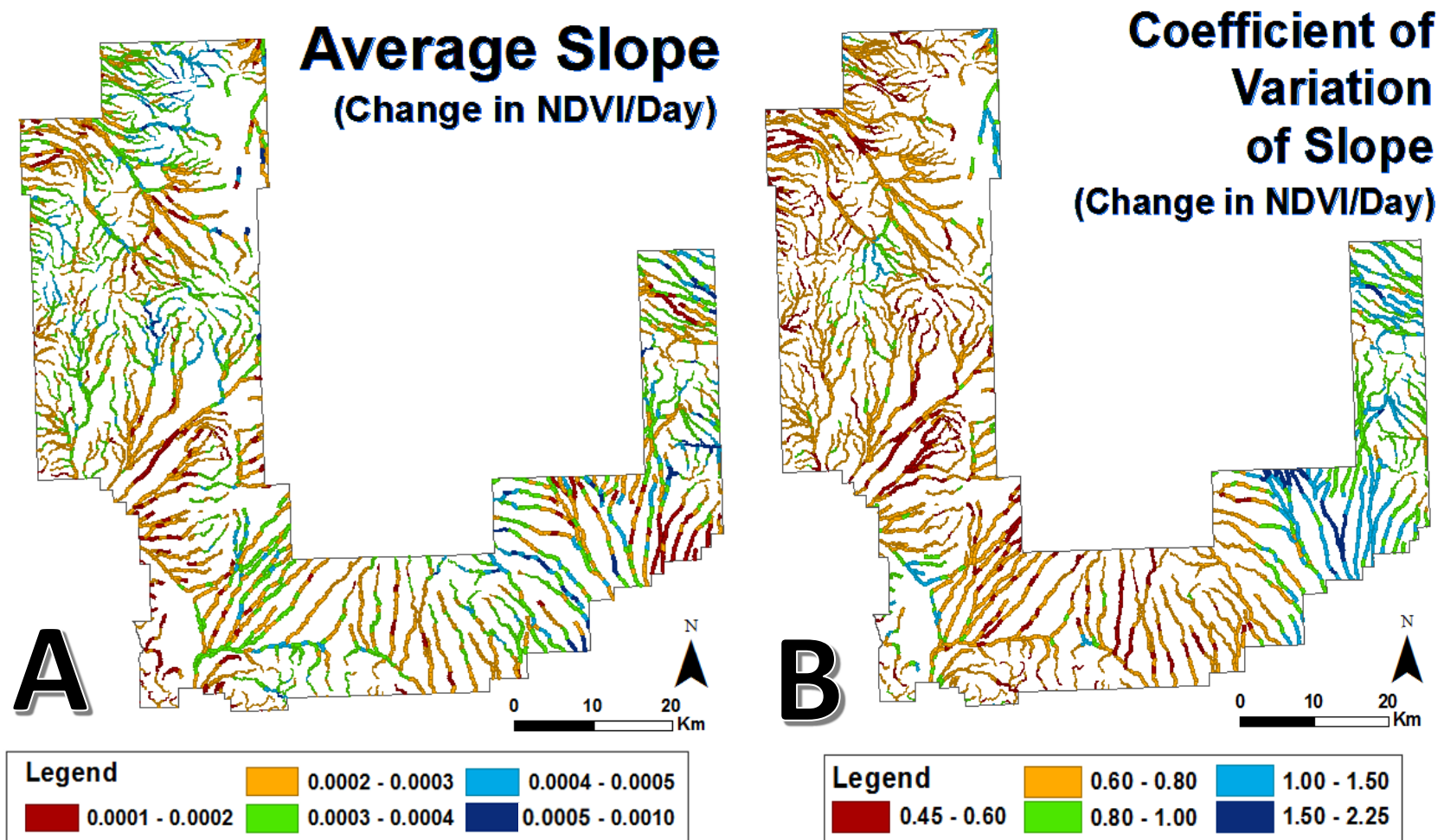
Figure 12: A: The slope (ΔNDVI/day) of the MTT values at each RAP were averaged over the 26 monsoon seasons. A larger slope indicates that there was on average higher increases in NDVI at that reach over the 26 years. **B:** The Coefficient of Variation (CV; standard deviation/mean) indicates the variance over the timeframe, where low CV values (CV < 1) suggests there was little change over the 26 monsoon seasons, while greater CV values (CV > 1) suggests that RAPs have higher variability in changes in NDVI between pre- and post-monsoon season images.

Some of the RAPs with a CV greater than 1.5 are in the region that was affected by the 2005 fire. This region is also supplied by a large mountain range in the KOFA National Wildlife Refuge preserve to the north and under the right conditions can experience large flow events. The distance of these channels from the mountain range also causes this region to undergo high transmission losses. This may explain why the southeastern portion of YPG sees higher variability in NDVI from 1986-2011 than the other regions. The mountainous region in the western portion of YPG may see more consistent weather patterns due to orographic effects, thus depicting lower CV value.

5.2 Winter Season

For the seven winter seasons examined, the 2004-05 season experienced more rainfall and more rain events than any other year. The NEXRAD/PRISM data measured approximately 140.5mm averaged over RAP units and NCDC rain gauge 3125 measured a total of 240mm of rainfall from September 1, 2004 to March 31, 2005 with 13 days measuring more than 5mm of rainfall, eight of which surpassed 10mm of precipitation. This is also apparent in the strong increase in MTT values that were recorded for this year (Figure 15 & Appendix D). There were also considerable increases in the MTT values during the winters of 2008-09 and 2009-10 where the NEXRAD radar data (averaged over RAP units) recorded approximately 37.4 and 105.5mm, respectively. The strong increase in MTT values for the 2008-09 winter may suggest that the 37.4mm average precipitation total is greatly underestimated or there were other variables such as temperature or precipitation timing and intensity that led to such high MTT values for this year. The 2009-10 winter season experienced rainfall later in the season which caused a delayed increase in the MTT values. It could also be expected that the MTT values would have further increased in the 2009-10 season, however two March scenes were left out due to significant amounts of cloud cover.

The remaining winters showed only slight changes in the MTT values (Figure 15 & Appendix D). The 2005-06 and 2006-07 winters experienced the earliest gain followed by a decrease in the MTT values suggesting a late monsoon season then followed by little winter precipitation. Lastly, the 2007-08 and 2010-11 seasons experienced few scattered rain events with minor gains in MTT values throughout the season.

In all cases, except for two, consecutive ΔNDVI-S's were found to be statistically different (p-value < 0.001; Appendix D, Table 10). This was tested through Paired T-Tests and when necessary the non-parametric Wilcoxon signed rank test between each 2,843 RAP unit of the two consecutive ΔNDVI-S's. The dates that were found not to be statistically different from each other are February 17 - April 6, 2007 and February 25 - April 14, 2010. In both cases, a statistical difference may have been detected if a cloudless Landsat scene was available in March of each year.

5.2.1 Correlation Analysis

Using RStudio 3.1.1 (R Core Team, 2014), a Spearman's Correlation for non-normal data was performed to determine the average time-lag between rainfall and an increase in NDVI using the MTT values for each season (Figure 13). The Spearman's Correlation was also completed on a combined and subset of dates (documented in Table 4) for all seven seasons (Figure 14). The Spearman's Correlation from Figure 13 shows that the MTT values have varying degrees of correlation to the precipitation-temperature interval data and vary significantly depending on the year.

Figure 13 shows that during the wettest season (2004-05), the increase in MTT values best correlates with the 32d precipitation total (0.69), where longer time intervals show no significant increases in correlation and may be attributed to fast growing herbaceous annuals that were abundant during this season (Esque et al., 2013). Other highly correlated variables for the 2004-05 winter season include the 16-32d precipitation interval (0.76) , rain events with >5mm at the 48d interval (0.66), and

31
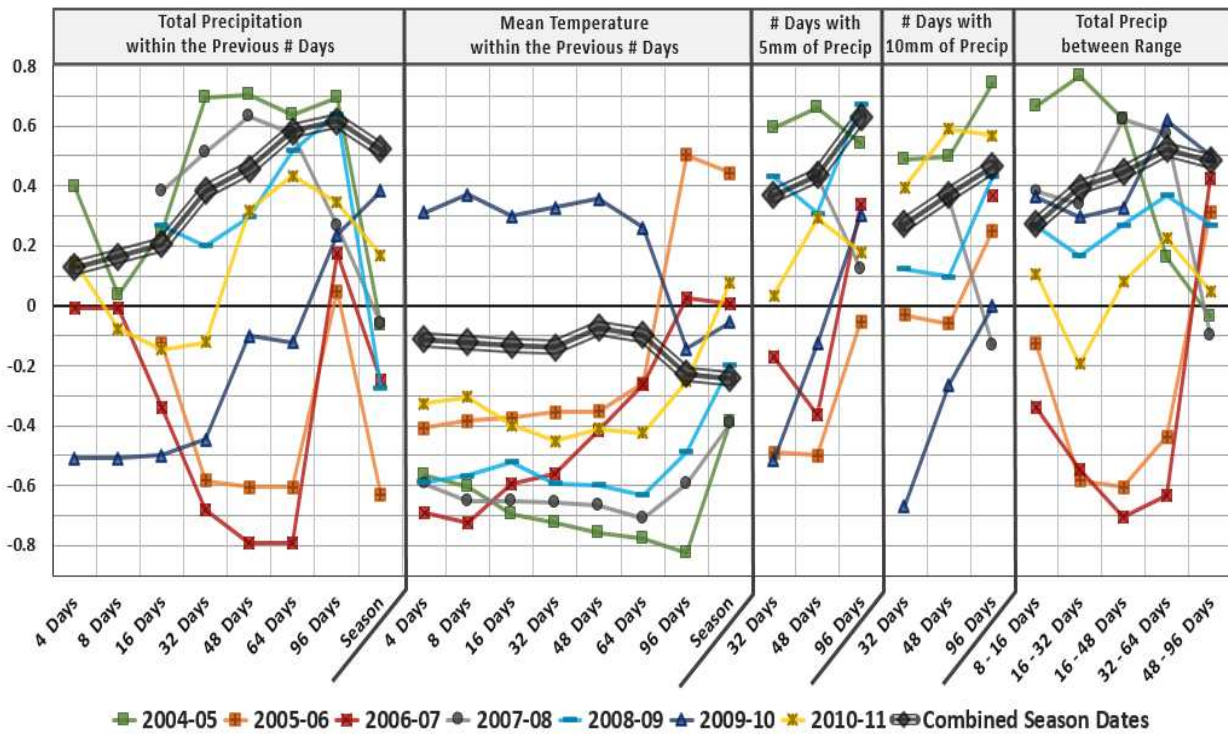
Figure 13: Spearman's Correlation of the winter MTT data and Precip/Temp Interval Data.

events >10mm at the 96d interval (0.74). During drier winters (2005-06 & 2006-07), there was a strong

negative correlation (-0.61 & -0.79, respectively) at both the 48 and 64d precipitation intervals and a

weak correlation for precipitation totals at the 4, 8, 16, and 96d intervals. Winters 2007-08 and 2010-

11 were average in total rainfall and concluded that the 48d at 0.63 (2007-08) and 64d at 0.43 (2010-

11) showed the highest correlation. 2010-11 also showed a relatively strong correlation to the >10mm,

48d interval (0.59). Surprisingly, the 2008-09 season, had similar rainfall totals to the 2007-08 and

2010-11 but showed a much stronger increase in MTT values (Appendix D). The radar precipitation

data for 2008-09 documented two early season rain events (late November and mid-December) with a

mean of 10mm or higher across the RAP units and one with a mean >5mm in early February. The 2008-

09 NDVI data is best correlated at the 96d precipitation interval (0.64) and number of rain events

>5mm during the previous 96d interval (0.67), but rain events >10mm only received a correlation of

32

0.43 at the 96d interval. The increase in MTT values for this year are intriguing and may suggest that

the NEXRAD data greatly underestimated the true rainfall or that other factors are involved, however

temperature does not seem unusual for this year. Another possibility for the substantial increase in

MTT during the 2008-09 season is due to the larger concentration of rain events recorded than during

the 2007-08 and 2010-11 seasons.

The 2009-10 period was the only season to have a positive correlation between mean temperature

and the MTT values for the 4-64d intervals. This is likely the result of not necessarily a winter with

below average temperatures, but the strong increase in NDVI in February, which is later than the other

seasons. These data suggests that the plants not only took advantage of late precipitation, but also

cooler temperatures that occur in December, January and February of 2009-10 (Appendix D: Mean

Monthly Temperature Graph). By coincidence, several significant rain events were captured within the

4d interval for the 24-Jan-10 date and caused poor correlation (-0.50) for the smaller precipitation time

intervals which increases in the larger time intervals with the season documenting the strongest

correlation at 0.38. This indicates that there is a substantial time delay from rainfall to vegetative

growth. The strongest positive correlation for the 2009-10 season occurred at the 32-64d *Between*

Range interval (0.62).

While the variation among years is important to recognize, the aggregation of each season may be

most relevant. When all seasons are combined (Figure 13 & 14; black diamonds), the correlation of MTT

values doubles between the 16d and 32d precipitation intervals. Although, the correlation continues to

grow in longer time-steps: 64d (0.58) and 96d (0.62) precipitation intervals, the increase is not as strong

as in the initial 32d interval. This is comparable to the Svoray & Karnieli (2011) results that show the

highest correlation for winter precipitation in a semi-arid climate to be at a month interval. The rates of

increases and strengths of correlation suggests that the time delay for the utilization of winter

precipitation by plants varies. Ogle & Reynolds (2004) recognize that deep-rooted tree or shrub species

will likely have a more gradual response to precipitation than shallow-rooted plant species. This could also imply that during the winter season initial plant growth occurs between two to four weeks following a rain event, but plants will continue to produce biomass, though at a lesser rate up to three months following the rain event.

Huxman et al. (2004) described rain events of 5mm or greater as significant where 5mm served as a threshold when relating to plant activity. Here, the total number of rain events 5mm or larger showed significant correlation especially at the 96d interval (0.63) and average for events >10mm at the 96d time step (0.47).

Table 4: Dates used in correlation analyses.

Combined Season Dates		Combined Late Season Dates
25-Dec-04	27-Feb-05	27-Feb-05
15-Mar-05	31-Mar-05	15-Mar-05
16-Apr-05	2-May-05	29-Jan-06
13-Jan-06	29-Jan-06	1-Feb-07
19-Apr-06	31-Dec-06	17-Feb-07
16-Jan-07	1-Feb-07	7-Mar-08
17-Feb-07	6-Apr-07	23-Mar-08
8-May-07	19-Jan-08	6-Feb-09
7-Mar-08	23-Mar-08	10-Mar-09
8-Apr-08	24-Apr-08	25-Feb-10
5-Jan-09	6-Feb-09	12-Feb-11
10-Mar-09	26-Mar-09	28-Feb-11
13-May-09	24-Jan-10	16-Mar-11
25-Feb-10	14-Apr-10	
30-Apr-10	27-Jan-11	
12-Feb-11	28-Feb-11	
16-Mar-11	1-Apr-11	
17-Apr-11		

This slight discrepancy could indicate that rain events of >10mm are less frequent than events of >5mm
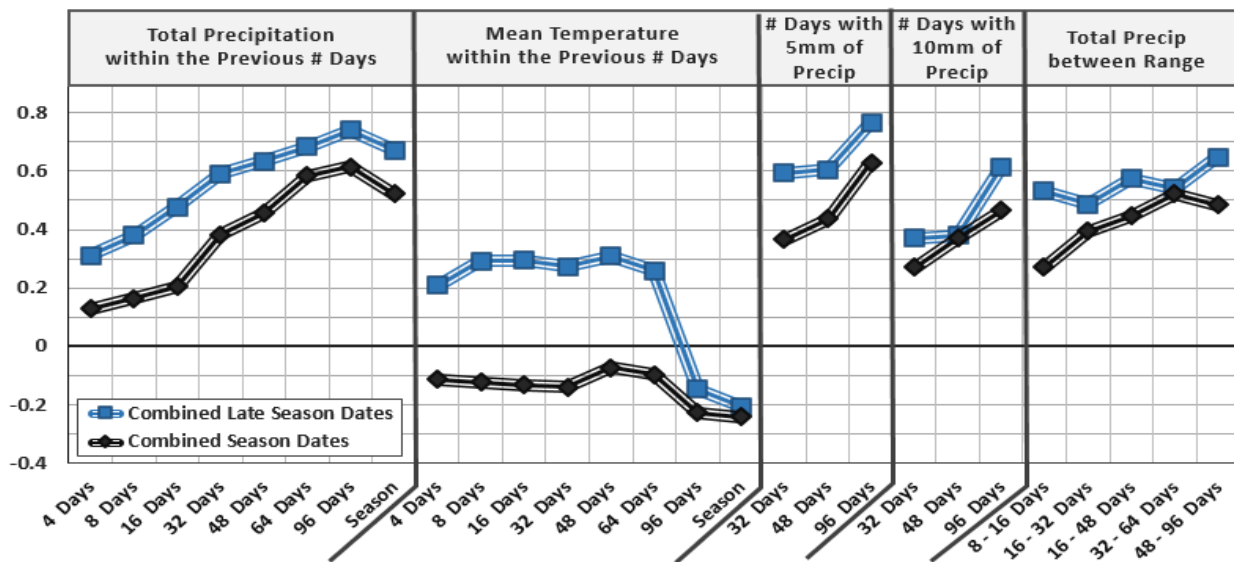
Figure 14: Spearman's Correlation of the winter season (**Combined Season Dates**) and using late January to end of March scenes (**Combined Late Season Dates**).

and therefore contribute less often to the overall increases in the MTT values. Furthermore, the

intervals that remove the more recent rain events showed mediocre correlation with the strongest

correlation occurring between 32-64d at 0.52.

Restricting the correlation analyses to late-season dates has not only improved the correlation

analysis, but may help explain the impacts of precipitation and temperature better than the complete

dataset. The dates used in the Combined Late Season Dates correlation analysis (Figure 14; blue

squares) are documented in Table 4 and include dates from late January to late March for all seven

seasons. Similar to the complete dataset, the Late Season subset shows that the correlation between

the MTT values and precipitation increases with longer timespans and peaks at the 96d time step with a

correlation of 0.74. The correlation for the Season interval (which measures precipitation between 112-

176d for these dates) decreases to 0.67. The 96d interval totaling rain events for >5mm and >10mm

also shows strong correlation at 0.77 and 0.62, correspondingly. The *Between Range* correlation is the

strongest at the 48-96d precipitation interval at 0.65. It is evident by this result that the MTT values

derived from the later ΔNDVI-S are often influenced by early season rainfall especially during drier

winters. Furthermore, for the Late Season subset, the correlation to mean temperature is positive for

each of the 4 to 64d intervals then decreases to below zero at the 96d and Season interval. Although

not a strong correlation, this shows that mid-season cooler temperatures aid in plant growth at YPG

during winter months.

5.3 Combining Monsoon and Winter Seasons

Antecedent precipitation inputs can play a major role in determining the immediate and long-lasting

impacts to the vegetation of an area. This may be especially true for dryland ecosystems. Holmgren and

Scheffer (2001) explain that increases in precipitation in southwestern deserts can initiate ecosystem

state changes, generate growth of woody seedlings, and produce positive feedback loops that will

impact the ecosystem for years to come. Moreover, Goodrich et al. (2008) measured a rise in winter

precipitation during the last half of the twentieth century and attributed the increases in precipitation to

a rise in ENSO conditions, while Kimball et al., (2010) suggests that a shift to later winter rains (from

October to December) supports higher densities of winter annuals that take advantage of increased

precipitation co-occurring with cooler temperatures.

Figure 15 combines the ΔNDVI-S of the monsoon season with the ΔNDVI-S winter seasons for years

2004-05 to 2010-2011. The 2004-05 winter season experienced extreme amounts of rainfall at YPG.

From these rains, there was a noticeable increase in winter annuals during this season (Esque et al.,

2013) which can be attributed to the extreme increase of the MTT values seen in Figure 15; 04-05. The
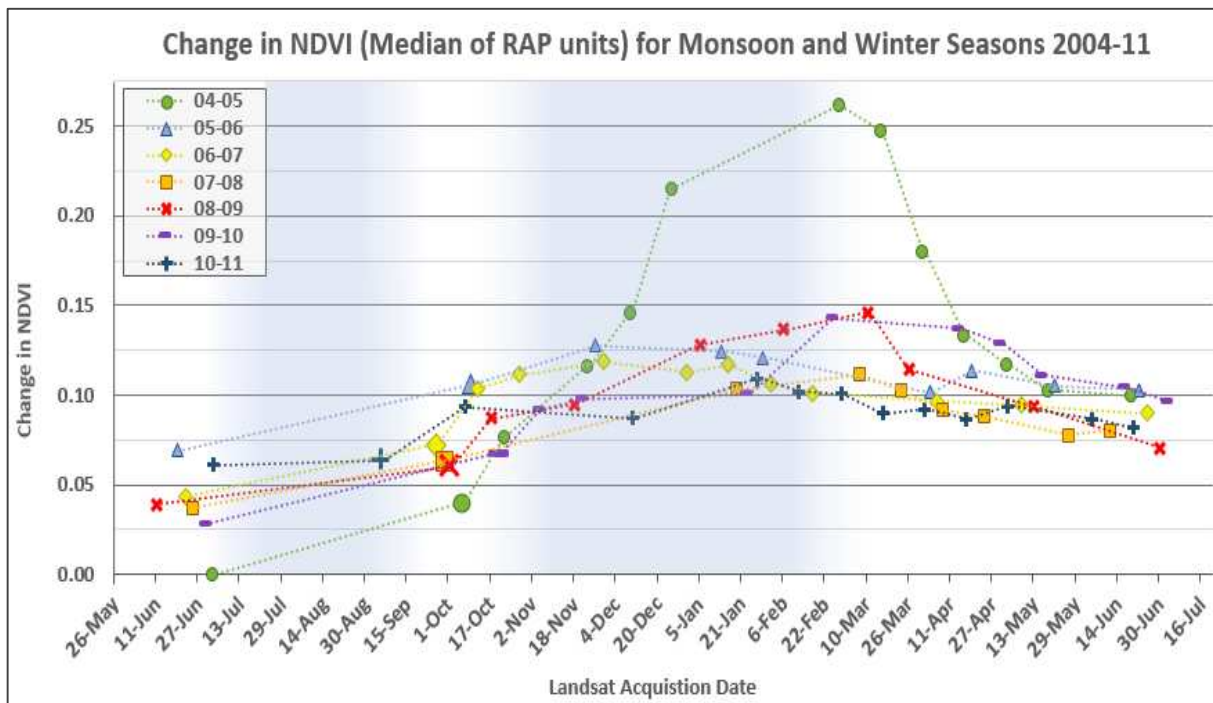
Figure 15: This graph combines the changes in NDVI over the monsoon and winter seasons starting
with June 2004 and going through June 2011. The common scene used for each year (June to June)
is the post-monsoon scene or base winter scene (larger symbols). To reset every year, the base/pre-
monsoon scene for the 2004-05 dataset (July 2, 2004) was subtracted from the base/pre-monsoon
season scene of each subsequent year. Since July 2, 2004 is the earliest date used in this analysis, it
is arbitrarily set at 0. Each of the following years starts out as more positive (increase in plant
biomass) than the July 2, 2004 Landsat scene.

pre-monsoon season Landsat scene (July 2, 2004), was subtracted from each of the following six years

of pre-monsoon scenes, all of which documented a stronger NDVI signal at the start of each monsoon

season than when compared to the 2004 scene. The strongest increase in the MTT values for pre-

monsoon season imagery was seen immediately following the 2004-05 winter. The following four

winters had low to moderate winter precipitation and caused a decrease in the MTT values at the start

of each monsoon season (2006-09). However, 2009-10 was another notable winter for precipitation

where the NCDC rain gauge 3125 measured at least 134mm of precipitation (data for December 2009

were absent) with a single event measuring 60mm of rainfall. The precipitation that occurred during

2009-10 winter caused a gain in the MTT values at the start of the following (2010) monsoon season.

5.4 Considerations

Brooks et al. (2011) states that "translating changes in precipitation into changes in plant available

water is not straightforward." Similarly, using NDVI to investigate precipitation influences is not exact

and there are a variety of factors that can either increase or decrease NDVI throughout the monsoon

and winter seasons. Such factors may include contributing area of the channel as well as channel type,

size of the storm, storm intensity (higher overland flow with stronger intensities), type of riparian

vegetation (woody versus herbaceous), vegetation densities or antecedent conditions. Changes in

landcover such as the decrease following the 2005 fire can also cause significant changes in NDVI that

may misrepresent the true amount of precipitation, unless the disturbance is accounted for. The timing

of the remote sensing imagery can play a major role in indicating when and where flood events have

occurred when using this method. Landsat imagery has a 16 day temporal resolution and when cloud

cover occurs within the imagery, then the temporal resolution can be pushed upwards of 32 or 48 days

in between usable scenes. Other remote sensing platforms may have shorter recurrence intervals, but

these often suffer from coarser resolution or higher costs. There are likely to be many other abiotic and

biotic variables that may influence the change in NDVI that are not mentioned here. In spite of these limitations, the results of this study show that Landsat imagery can play a pivotal role in explaining the occurrence and magnitude of precipitation in dryland ecosystems.

Most precipitation events are scarce and typically deliver less than a few millimeters of precipitation during each event. Accurately mapping these rain events is difficult and errors are hard to detect. While radar data is spatially and temporally continuous, observed radar values often misrepresent the actual precipitation for a number of different reasons: including reflectance issues, obstructions such as mountain ranges, small spatial storms (resolution of NEXRAD data is $16km^2$), and overshooting the cloud layer as happens during low-top convection storms. Moreover, from these data, it appears that NEXRAD is extremely inaccurate in measuring monsoon season precipitation and though it is more accurate for winter precipitation, it was shown here that NEXRAD typically underestimates precipitation at YPG and in surrounding areas.

CHAPTER 6: CONCLUSIONS

This study proposes that the change in NDVI across ephemeral stream channels may be used as an alternative to historic rain gauge and radar precipitation data. Landsat TM imagery has the spatial continuity that supersedes the densities of rain gauge sites and a historical record that far exceeds radar data. The MTT values that are derived from the ΔNDVI-S along ephemeral stream channels provides a unique method for mapping the increases and decreases in plant biomass while indirectly mapping the spatial, temporal, and to some extent the quantity of precipitation in water-limiting systems.

These data indicate that a strong increase in the MTT values between the pre- and post-monsoon season Landsat imagery reveal precipitation inputs and possibly the occurrence of flow events. Analyses of two flow events indicates that increases of 0.0006 ΔNDVI/day or larger using the ΔNDVI-S MTT values over the course of the monsoon season suggests a flow event. More comparisons may clarify the 0.0006 ΔNDVI/day threshold and may in fact reduce this value. However, even without a true threshold, mapping the slope of the MTT values between the pre- and post-monsoon season scenes often shows strong increases in the MTT values beginning in upper stream channels and continuing downstream into braided channels, where the MTT values lessen (Figure 12.A: Average Slope & Appendix E). This reflects the fact that flow events are often localized in semi-arid systems.

Combination of the monsoon and winter season MTT values for the overlapping years indicate that monsoon season precipitation may support vegetation into cooler winter months even when there is insignificant precipitation. This analysis also indicates that for YPG, post-monsoon season imagery captured in early to mid-September is often too early to measure the true increases in the MTT values. A third conclusion that these data support is the influences of antecedent precipitation. The above

average rainfall during the 2004-05 winter increased the MTT values for at least the subsequent four years until another rainy winter season ensued and caused another jump in the MTT values.

The final conclusions from these data show that there is a moderate to high correlation between the MTT values derived from the winter ΔNDVI-S and the NEXRAD precipitation data and that the strength of the correlation will vary considerably depending upon the weather for that year. Combination of the seven winter seasons indicates that plant biomass will increase during the first 2-4 weeks following a rain event and continue to increase up to 2-3 months after the rain event(s). The two time delay periods may reflect various types of vegetation in the region (i.e. shallow-rooted herbaceous or deep-rooted woody vegetation). The occurrence of precipitation events 5mm or larger showed strong correlation to changes among MTT values and implies that a rain event measuring as little as 5mm should be considered a significant event to vegetation during winter months in semi-arid regions.

The methodology and conclusions documented in this paper creates a novel method for measuring the spatial and temporal variability of precipitation in the Sonoran Desert by exploiting the strong connection between water inputs to vegetation growth, and finally, to the ability of remote sensing imagery to record such changes. While there have been many other studies that have documented the relationship between precipitation and vegetation growth using NDVI, there have been far fewer that have used NDVI as a way to measure the spatial and temporal range of precipitation. Even though this research attempts to find clear connections between precipitation and NDVI, the environment is vastly complex and such relationships are certainly contingent upon different circumstances.

CHAPTER 7: AFTERWORD

In the fall of 2012, I entered graduate school but not as a full time student, instead as a guest student enrolled in two courses. Although this was not my ideal situation, this allowed me to ease my way back into academia after a seven year break and build meaningful relationships with professors and students. This also gave me the opportunity to become a NASA student intern with the NASA DEVELOP Program. The NASA DEVELOP program is a 10-week paid internship that assembles a team of students to answer a preassigned ecological research question using remote sensing technology. This internship with the two courses set me up for applying to a graduate student announcement working with the Strategic and Environmental Research and Development Program (SERDP) under Dr. Melinda Laituri that began the following semester. This position allowed me to enroll in the Graduate Degree Program in Ecology (GDPE) and focused on using GIS and remote sensing technologies within ephemeral stream ecosystems in the arid southwest.

I spent two years in this position and was extremely grateful to have it, however this does not come without hard work and challenging circumstances. After I began the SERDP position in early 2013, the other CSU graduate student associated with this project resigned. There were two other graduate students involved in the project, but they were based out of the University of Arizona in Tucson along with the principle investigator. This made it hard to interact with them routinely and to develop a thesis where my skills and ideas would be most appropriate while aligning with my own interests.

Although I had flexibility in selecting a research question, I experienced challenges many graduate students face with times of ambiguous direction while being conflicted by the need to complete what the resigned student had left, while trying to incorporate my own ideas. A major challenge that I encountered was integrating myself into the SERDP RC-1727 project which was already halfway through its life span. Field work was completed by the time I had arrived and funding and time were limited.

However, with the knowledge I gained from the NASA DEVELOP program, I began to see the potential for a thesis question while working with the GIS data at the DoD installations: Fort Bliss, Fort Huachuca, Yuma Proving Ground, and Fort Irwin. This is when I developed the idea of linking vegetation to precipitation through remote sensing. This is not a new topic and has been extensively study, however, I choose a new direction, suggesting that Landsat imagery can be a better data source when regarding Monsoon Season precipitation, something that RADAR and rain gauges often have a harder time measuring consistently. This gave me a niche that I could pursue and most importantly, something that I found interesting.

Unfortunately, as in most exploratory phases of research, it was difficult to really develop this idea and instead I pursued several other paths that eventually proved unsuccessful. This ultimately slowed the completion of my thesis and defense considerably. Throughout this process from the DEVELOP internship, to graduate assistantship, to developing my own thesis I have learned that determination and perseverance come from a passion for the subject. I do not believe that without my genuine interest in these projects and my research topic that I would have completed this thesis.

During the last phase of my graduate career (i.e. writing and defending my thesis), I took a position with the National Park Service at Colorado National Monument where I worked in removing invasive plant species and restoring native landscapes. Though still a seasonal position, it is the very position that I went to graduate school for. Working with the National Park Service has allowed me to work toward my career goal of managing and restoring native landscapes, but I was faced with the challenge of finishing graduate school. I do not recommend working while finishing a master's degree, however in my situation, it was the best thing I could do. It was hard at times to stay on-track, but eventually I found the time and gained new perspectives on the demands of completing a research project.

In the end, I am so very grateful for the graduate experience and the support provided by my advisor. I learned a great deal in the classroom and even more crafting a valid research question with

the methods and statistics to support it. This experience has also reinforced my interests in a career in land management. I enjoy the knowledge that research brings and value their place in steering management practices and this experience has allowed me to develop useful and meaningful skills that I will be able to employ within a land management position. Lastly, this assistantship has allowed me to develop my interpersonal skills by working toward project objectives. This is a skill I did not have before starting this project. The collaboration and coordination that were necessary for the project's success have allowed me to see the utility in such an approach, while the independence has permitted me to bring my own skills and research questions to the table.

Barbosa, H.A., 2004. Vegetation dynamics over the Northeast region of Brazil and their connections with climate variability during the last two decades of the twentieth century. Doctoral degree dissertation in Soil, Water, and Environmental Science at the University of Arizona. Tucson, Arizona.

Barbosa, H.A., A. R. Huete and W. E. Baethgen. 2006. A 20-year study of NDVI variability over the Northeast Region of Brazil. *Journal of Arid Environments* **67(2)**: 288-307.

Bowers, J. E. 2005. El Nino and displays of spring-flowering annuals in the Mojave and Sonoran deserts. *The Journal of the Torrey Botanical Society* **132(1)**:38-49.

Bowers, J. E., R. M. Turner, and T. L. Burgess. 2004. Temporal and spatial patterns in emergence and early survival of perennial plants in the Sonoran Desert. *Plant Ecology* **172(1)**:107-119.

Brooks, P. D., P. A. Troch, M. Durcik, E. Gallo, and M. Schlegel. 2011. Quantifying regional scale ecosystem response to changes in precipitation: Not all rain is created equal. *Water Resources Research* **47(10)**.

Brown, M. E., J. E. Pinzón, K. Didan, J. T. Morisette, and C. J. Tucker. 2006. Evaluation of the consistency of long-term NDVI time series derived from AVHRR, SPOT-Vegetation, SeaWiFS, MODIS, and Landsat ETM+ sensors. *Geoscience and Remote Sensing, IEEE Transactions on* **44(7)**:1787-1793.

Brunsell, N. A. and C. B. Young. 2008. Land surface response to precipitation events using MODIS and NEXRAD data. *International Journal of Remote Sensing* **29(7)**:1965-1982.

Collins, S. L., R. L. Sinsabaugh , C. Crenshaw, L. Green, A. Porras-Alfaro, M. Stursova, and L. H. Zeglin. 2008. Pulse dynamics and microbial processes in aridland ecosystems. *Journal of Ecology* **96(3)**:413-420.

Esque, T. C., R. H. Webb, C. S. Wallace, C. van Riper III, C. McCreedy, and L. Smythe. 2013. Desert fires fueled by native annual forbs: effects of fire on communities of plants and birds in the lower Sonoran desert of Arizona. *The Southwestern Naturalist* **58(2)**:223-233.

Carlson, E. A. 2009. Fluvial riparian classification for national forests in the western United States. M.S. Thesis. Colorado State University.

Faulconer, J. D. 2015. Thresholds for runoff generation in ephemeral streams with varying morphology in the Sonoran desert in Arizona, USA. M. S. Thesis. Colorado State University.

Friedman, J. M., and V. J. Lee. 2002. Extreme floods, channel change, and riparian forests along ephemeral streams. *Ecological Monographs* **72(3)**:409-425.

Fulton, R. A. 2002. Activities to improve WSR-88D radar rainfall estimation in the National Weather Service. In *Proceedings of the Second Federal Interagency Hydrologic Modeling Conference, Las Vegas, Nevada*. Subcommittee on Hydrology, Advisory Committee on Water Data, CD-ROM [Available online at http://nws.noaa.gov/ohd/hrl/presentations /fihm02/pdfs/ qpe_hydromodelconf_web.pdf]

Goodrich, D. C., C. L. Unkrich, T. O. Keefer, M. H. Nichols, J. J. Stone, L. R. Levick, and R. L. Scott. 2008. Event to multidecadal persistence in rainfall and runoff in southeast Arizona. *Water Resources Research* **44(5)**.

Holmgren, M., and M. Scheffer. 2001. El Niño as a window of opportunity for the restoration of degraded arid ecosystems. *Ecosystems* **4(2)**:151-159.

Huxman, T. E., K. A. Snyder, D. Tissue, A. J. Leffler, K. Ogle, W. T. Pockman, D. R. Sandquist, D. L. Potts, and S. Schwinning. 2004. Precipitation pulses and carbon fluxes in semiarid and arid ecosystems. *Oecologia* **141(2)**:254-268.

Ichii, K., A. Kawabata, and Y. Yamaguchi. 2002. Global correlation analysis for NDVI and climatic variables and NDVI trends: 1982-1990. *International Journal of Remote Sensing* **23(18)**:3873-3878.

Kerr, J. T., and M. Ostrovsky. 2003. From space to species: ecological applications for remote sensing. *Trends in Ecology & Evolution* **18(6)**:299-305.

Kimball, S., A. L Angert, T. E. Huxman, and D. L. Venable. 2010. Contemporary climate change in the Sonoran Desert favors cold-adapted species. *Global Change Biology* **16(5)**:1555-1565.

Levick, L., Hammer, S., Lyon, R., Murray, J., Birtwistle, A., Goodrich, D., Bledsoe, B., Guertin, P., and M. Laituri. 2015. An ecohydrological approach to managing intermittent and ephemeral streams on Department of Defense lands in the Southwestern United States. Department of Defense, Strategic Environmental Research and Development Program (SERDP), Project RC-1727.

Lichvar, R., D. Cate, C. Photos, L. Dixon, B. Allen, and J. Byersdorfer. 2009. Vegetation and channel morphology responses to ordinary high water discharge events in arid west stream channels (No. ERDC/CRREL TR-09-5). *Engineer Research and Development Center.* Hanover, NH: Cold Regions Research and Engineering Lab.

National Weather Service. n.d. Monsoon inter-annual variability. Retrieved from http://www.wrh.noaa.gov/twc/monsoon/monsoon_variability.pdf (Accessed March 15, 2015).

Nguyen, U., E. P. Glenn, P. L. Nagler, and R. L. Scott. 2014. Long-term decrease in satellite vegetation indices in response to environmental variables in an iconic desert riparian ecosystem: the Upper San Pedro, Arizona, United States. *Ecohydrology*.

Nicholson, S. E., and T.J. Farrar. 1994. The influence of soil type on the relationships between NDVI, rainfall, and soil moisture in semiarid Botswana. I. NDVI response to rainfall. *Remote Sensing of Environment* **50(2)**:107-120.

NPS. n.d. Retrieved from http://www.nature.nps.gov/views/KCs/SonoranDesert/HTML/ET_02_ Chapter2.htm (Accessed September 8, 2014).

Ogle, K., and J. F. Reynolds. 2004. Plant responses to precipitation in desert ecosystems: integrating functional types, pulses, thresholds, and delays. *Oecologia* **141(2)**:282-294.

Pettorelli, N., J. O. Vik, A. Mysterud, J.M. Gaillard, C.J. Tucker, and N. C. Stenseth. 2005. Using the satellite-derived NDVI to assess ecological responses to environmental change. *Trends in Ecology & Evolution* **20(9)**:503-510.

PRISM Climate Group. 2010. Gridded climate data for the contiguous USA. http://prism.oregonstate.edu

R Core Team. 2014. R: A language and environment for statistical computing. R Foundation for Statistical Computing. Vienna, Austria. Retrieved October 7, 2014. http://www.R-project.org/

Reynolds, J. F., P. R. Kemp, K. Ogle, and R. J. Fernández. 2004. Modifying the 'pulse–reserve' paradigm for deserts of North America: precipitation pulses, soil water, and plant responses. *Oecologia* **141(2)**:194-210.

Richard Y., and I. Poccard. 1998. A statistical study of NDVI sensitivity to seasonal and interannual rainfall variations in Southern Africa. *International Journal of Remote Sensing* **19(15)**:2907-2920.

Schaake, J., A. Henkel, and S. Cong. 2004. 5.3 Application of PRISM Climatologies for Hydrologic Modeling and Forcasting in the Western US.

Shaw, J. R., and D. J. Cooper. 2008. Linkages among watersheds, stream reaches, and riparian vegetation in dryland ephemeral stream networks. *Journal of Hydrology* **350(1)**:68-82.

Snyder, K. A., and S. L. Tartowski. 2006. Multi-scale temporal variation in water availability: implications for vegetation dynamics in arid and semi-arid ecosystems. *Journal of Arid Environments* **65(2)**:219-234.

Stein, B. A., C. Scott, and N. Benton. 2008. Federal lands and endangered species: the role of military and other federal lands in sustaining biodiversity. *BioScience* **58(4)**:339-347.

Stromberg, J. C., V. B. Beauchamp, M. D. Dixon, S. J. Lite, and C. Paradzick. 2007. Importance of low-flow and high-flow characteristics to restoration of riparian vegetation along rivers in arid south-western United States. *Freshwater Biology* **52(4)**:651-679.

Sutfin, N. A., J. R. Shaw, E. E. Wohl, and D. J. Cooper. 2014. A geomorphic classification of ephemeral channels in a mountainous, arid region, southwestern Arizona, USA. *Geomorphology* **221**:164-175.

Svoray, T., and A. Karnieli. 2011. Rainfall, topography and primary production relationships in a semiarid ecosystem. *Ecohydrology* **4(1)**:56-66.

Thomey, M. L., S. L., Collins, R. Vargas, J. E. Johnson, R. F. Brown, D. O. Natvig, and M. T. Friggens. 2011. Effect of precipitation variability on net primary production and soil respiration in a Chihuahuan Desert grassland. *Global Change Biology* **17(4)**:1505-1515.

Vogelmann, J. E., B. Tolk, and Z. Zhu. 2009. Monitoring forest changes in the southwestern United States using multitemporal Landsat data. *Remote Sensing of Environment* **113(8)**:1739-1748.

Wang, X., H. Xie, H. Sharif, and J. Zeitler. 2008. Validating NEXRAD MPE and Stage III precipitation products for uniform rainfall on the Upper Guadalupe River Basin of the Texas Hill Country. *Journal of Hydrology* **348(1)**: 73-86.

Wang, J., P.M. Rich, and K. P. Price. 2003. Temporal responses of NDVI to precipitation and temperature in the central Great Plains, USA. *International Journal of Remote Sensing* **24(11)**:2345-2364.

Western Regional Climate Center. 2012. Yuma Proving Ground (029654). Period of record monthly climate summaries. (http://www.wrcc.dri.edu/cgi-bin/cliMAIN.pl?azyupg, Accessed November 20, 2014).

Wu, W., D. Kitzmiller, and S. Wu. 2012. Evaluation of radar precipitation estimates from the national mosaic and multisensor quantitative precipitation estimation system and the WSR-88D precipitation processing system over the conterminous United States. *Journal of Hydrometeorology* **13(3)**:1080-1093.

Xie, H., X. Zhou, E. R. Vivoni, J. M. Hendrickx, and E. E. Small. 2006. GIS-based NEXRAD Stage III precipitation database: automated approaches for data processing and visualization. *Computers & Geosciences* **31(1)**:65-76.

Table 5: Overview of data used in this study

Data	Type	Resolution	Objective	USE	Source
LANDSAT 5 TM	Grid	0.9 km^2	Monsoon, Winter	NDVI Response Variable	http://glovis.usgs.gov/
LANDSAT 7 TM	Grid	0.9 km^2	Monsoon	NDVI Response Variable	http://glovis.usgs.gov/
LANDSAT 8 TM	Grid	0.9 km^2	Monsoon	NDVI Response Variable	http://glovis.usgs.gov/
NHDPlus V2	Vector	Various	Monsoon, Winter	Input for the Inundated 1km Reach Polygons	www.horizon-systems.com/nhdplus/
National Elevation Dataset (1/3 arc second)	Grid	10 m^2	Monsoon, Winter	Input for the Inundated 1km Reach Polygons	http://viewer.national map.gov/viewer/
Inundated 1km Reach Polygons	Vector	Various	Monsoon, Winter	Riparian Area Polygons (RAPs): The unit of analysis	data created for the SERDP: RC-1727 project
Rain Gauge	Vector	~1.5 km^2	Monsoon, Winter	Assess Radar Data	Data from the SERDP: RS-1725 project
GHCN Rain Gauge Data	Vector	~1.5 km^2	Monsoon, Winter	General Trends, Assess Radar Data	http://www.ncdc.noaa. gov/data-access/land-based-station-data/land-based-datasets/global-historical-climatology-network-ghcn
NEXRAD MPE	Vector	16 km^2	Winter	Precipitation Estimates Jan 2005 – Apr 2011	water.weather.gov/pre cip/p_download _new/
PRISM Precipitation	Grid	16 km^2	Winter	Precipitation Estimates Oct 2004 –Dec 2004	http://www.prism. oregonstate.edu/
PRISM Temperature	Grid	16 km^2	Winter	Temperature Means October 2004 – April 2011	http://www.prism. oregonstate.edu/

Table 6: An account of Landsat Scenes used in this study

LANDSAT ID	Acquisition Date	Radar Precipitation Data Interval	Clouds	# Days from base
------- Monsoon Scene Dates -------				
LT50380371986166XXX13	Jun 15, 1986	NA	None	*Base*
LT50380371986294XXX03	Oct 21, 1986	NA	None	128
LT50380371987169XXX07	Jun 18, 1987	NA	None	*Base*
LT50380371987281XXX01	Oct 8, 1987	NA	None	112
LT50380371988156XXX07	Jun 4, 1988	NA	None	*Base*
LT50380371988268XXX03	Sep 24, 1988	NA	None	112
LT50380371989174XXX02	Jun 23, 1989	NA	None	*Base*
LT50380371989270XXX02	Sep 27, 1989	NA	None	96
LT50380371990145AAA03	May 25, 1990	NA	None	*Base*
LT50380371990273XXX02	Sep 30, 1990	NA	None	128
LT50380371991180XXX03	Jun 29, 1991	NA	None	*Base*
LT50380371991276XXX02	Oct 3, 1991	NA	None	96
LT50380371992167XXX03	Jun 15, 1992	NA	None	*Base*
LT50380371992279AAA02	Oct 5, 1992	NA	None	112
LT50380371993185XXX02	Jul 4, 1993	NA	None	*Base*
LT50380371993281AAA04	Oct 8, 1993	NA	None	96
LT50380371994188XXX02	Jul 7, 1994	NA	None	*Base*
LT50380371994284AAA02	Oct 11, 1994	NA	None	96
LT50380371995159XXX02	Jun 8, 1995	NA	None	*Base*
LT50380371995255XXX02	Sep 12, 1995	NA	None	96
LT50380371996130XXX02	May 9, 1996	NA	None	*Base*
LT50380371996290XXX01	Oct 16, 1996	NA	None	160
LT50380371997196XXX02	Jul 15, 1997	NA	None	*Base*
LT50380371997292XXX02	Oct 19, 1997	NA	None	96
LT50380371998167XXX02	Jun 16, 1998	NA	None	*Base*
LT50380371998279XXX02	Oct 6, 1998	NA	None	112
LT50380371999154XXX05	Jun 3, 1999	NA	None	*Base*
LT50380371999250XXX04	Sep 7, 1999	NA	None	96
LE70380372000165EDC00	Jun 13, 2000	NA	None	Base
LE70380372000261EDC00	Sep 17, 2000	NA	None	96
LE70380372001167EDC00	Jun 16, 2001	NA	None	*Base*
LE70380372001263EDC00	Sep 20, 2001	NA	None	96
LE70380372002170EDC00	Jun 19, 2002	NA	None	*Base*
LE70380372002266EDC00	Sep 23, 2002	NA	None	96
LT50380372003165LGS01	Jun 14, 2003	NA	None	*Base*
LT50380372003261PAC02	Sep 18, 2003	NA	None	96
LT50380372004184PAC01	Jul 2, 2004	NA	None	*Base*
LT50380372004280PAC01	Oct 6, 2004	NA	None	96
LT50380372005170PAC01	Jun 19, 2005	NA	None	*Base*
LT50380372005250PAC01	Sep 7, 2005	NA	None	80

LT50380372005282PAC01	Oct 9, 2005	NA	None	112
LT50380372006173PAC02	Jun 22, 2006	NA	None	*Base*
LT50380372006269PAC01	Sep 26, 2006	NA	None	96
LT50380372007176PAC01	Jun 25, 2007	NA	None	*Base*
LT50380372007272EDC00	Sep 29, 2007	NA	None	96
LT50380372008163PAC02	Jun 11, 2008	NA	None	*Base*
LT50380372008275PAC01	Oct 1, 2008	NA	None	112
LT50380372009181PAC01	Jun 30, 2009	NA	None	*Base*
LT50380372009293PAC01	Oct 20, 2009	NA	None	112
LT50380372010184EDC00	Jul 3, 2010	NA	None	*Base*
LT50380372010248PAC01	Sep 5, 2010	NA	None	64
LT50380372011171PAC01	Jun 20, 2011	NA	None	*Base*
LT50380372011251PAC02	Sep 8, 2011	NA	None	80
------- Monsoon Flood Events Scene Dates -------				
LT50380371989174XXX02	Jun 23, 1989	NA	None	*Base*
LT50380371989206XXX02	Jul 25, 1989	NA	None	32
LT50380371989238XXX02	Aug 26, 1989	NA	None	64
LT5038037198 9254XXX02	Sep 11, 1989	NA	None	80
LT50380371989270XXX02	Sep 27, 1989	NA	Some	96
LT50380371989302XXX02	Oct 29, 1989	NA	None	128
LC80380372013208LGN00	Jul 27, 2013	NA	None	*Base*
LC80380372013224LGN00	Aug 12, 2013	NA	None	16
LC80380372013256LGN00	Sep 13, 2013	NA	None	48
LC80380372013288LGN00	Oct 15, 2013	NA	None	80
LC80380372013304LGN00	Oct 31, 2013	NA	None	96
------- Winter Scene Dates -------				
2004-2005: Total Precip (Oct 1 – Mar 31): 102.8mm (Virtual Grid: 269218)				
LT50380372004280PAC01	Oct 6, 2004	2004 Base	None	0
LT50380372004296PAC01	Oct 22, 2004	4, 8, 16, Season	Some	16
LT50380372004328PAC01	Nov 23, 2004	4, 8, 16, 32, 48, Season	None	48
LT50380372004344PAC02	Dec 9, 2004	4, 8, 16, 32, 48, 64, Season	None	64
LT50380372004360PAC01	Dec 25, 2004	4, 8, 16, 32, 48, 64, Season	None	80
LT50380372005058PAC01	Feb 27, 2005	4, 8, 16, 32, 48, 64, 96, Season	Some	144
LT50380372005074PAC01	Mar 15, 2005	4, 8, 16, 32, 48, 64, 96, Season	None	160
LT50380372005090PAC01	Mar 31, 2005	4, 8, 16, 32, 48, 64, 96, Season	None	176
LT50380372005106PAC01	Apr 16, 2005	4, 8, 16, 32, 48, 64, 96, Season	None	192
LT50380372005138PAC01	May 18, 2005	NA	None	224
LT50380372005170PAC01	Jun 19, 2005	NA – Monsoon Base	None	256
2005-2006: Total Precip (Oct 1 – Mar 31): 27.7mm (Virtual Grid: 269218)				
LT50380372005282PAC01	Oct 9, 2005	2005 Base	None	0
LT50380372005330PAC01	Nov 26, 2005	4, 8, 16, 32, 48, Season	None	48
LT50380372006013EDC00	Jan 13, 2006	4, 8, 16, 32, 48, 64, 96, Season	None	96
LT50380372006029PAC01	Jan 29, 2006	4, 8, 16, 32, 48, 64, 96, Season	None	112

LT50380372006093PAC01	Apr 3, 2006	4, 8, 16, 32, 48, 64, 96, Season	Some	176
LT50380372006109PAC01	Apr 19, 2006	4, 8, 16, 32, 48, 64, 96, Season	None	192
LT50380372006141PAC01	May 21, 2006	NA	None	224
LT50380372006173PAC02	Jun 22, 2006	NA – Monsoon Base	None	256
2006-2007: Total Precip (Oct 1 – Mar 31): 19.8mm (Virtual Grid: 269218)				
LT50380372006269PAC01	Sep 26, 2006	2006 Base	None	0
LT50380372006285PAC01	Oct 12, 2006	4, 8, 16, Season	None	16
LT50380372006301PAC01	Oct 28, 2006	4, 8, 16, 32, Season	None	32
LT50380372006333PAC01	Nov 29, 2006	4, 8, 16, 32, 48, 64 Season	None	64
LT50380372006365PAC01	Dec 31, 2006	4, 8, 16, 32, 48, 64, 96, Season	None	96
LT50380372007016PAC01	Jan 16, 2007	4, 8, 16, 32, 48, 64, 96, Season	None	112
LT50380372007032PAC01	Feb 1, 2007	4, 8, 16, 32, 48, 64, 96, Season	None	128
LT50380372007048PAC01	Feb 17, 2007	4, 8, 16, 32, 48, 64, 96, Season	None	144
LT50380372007096PAC01	Apr 6, 2007	4, 8, 16, 32, 48, 64, 96, Season	Some	192
LT50380372007128PAC01	May 8, 2007	NA	None	224
LT50380372007160PAC01	Jun, 9, 2007	NA	None	256
LT50380372007176PAC01	Jun 25, 2007	NA – Monsoon Base	None	272
LEAPYEAR. 2007-2008: Total Precip (Oct 1 – Mar 31): 47.8 mm (Virtual Grid: 269218)				
LT50380372007272EDC00	Sep 29, 2007	2007 Base	None	0
LT50380372008019EDC00	Jan 19, 2008	4, 8, 16, 32, 48, 64, 96, Season	None	112
LT50380372008067PAC01	Mar 7, 2008	4, 8, 16, 32, 48, 64, 96, Season	Some	160
LT50380372008083PAC01	Mar 23, 2008	4, 8, 16, 32, 48, 64, 96, Season	None	176
LT50380372008099PAC01	Apr 8, 2008	4, 8, 16, 32, 48, 64, 96, Season	None	192
LT50380372008115PAC01	Apr 24, 2008	4, 8, 16, 32, 48, 64, 96, Season	None	208
LT50380372008147PAC01	May 26, 2008	NA	None	240
LT50380372008163PAC02	Jun 11, 2008	NA – Monsoon Base	None	256
2008-2009: Total Precip (Oct 1 – Mar 31): 31.2 mm (Virtual Grid: 269218)				
LT50380372008275PAC01	Oct 1, 2008	2008 Base	None	0
LT50380372008291PAC01	Oct 17, 2008	4, 8, 16, Season	None	16
LT50380372008323PAC01	Nov 18, 2008	4, 8, 16, 32, Season	None	48
LT50380372009005PAC01	Jan 5, 2009	4, 8, 16, 32, 48, 64, Season	None	96
LT50380372009037PAC01	Feb 6, 2009	4, 8, 16, 32, 48, 64, 96, Season	Some	128
LT50380372009069PAC01	Mar 10, 2009	4, 8, 16, 32, 48, 64, 96, Season	None	160
LT50380372009085PAC01	Mar 26, 2009	4, 8, 16, 32, 48, 64, 96, Season	None	176
LT50380372009133PAC01	May 13, 2009	NA	None	224
LT50380372009181PAC01	Jun 30, 2009	NA – Monsoon Base	None	272
2009-2010: Total Precip (Oct 1 – Mar 31): 95.3mm (Virtual Grid: 269218)				
LT50380372009293PAC01	Oct 20, 2009	2009 Base	None	0
LT50380372009309PAC01	Nov 5, 2009	4, 8, 16, Season	None	16
LT50380372009325PAC01	Nov 21, 2009	4, 8, 16, 32, Season	None	32
LT50380372010024PAC01	Jan 24, 2010	4, 8, 16, 32, 48, 64, Season	None	64
LT50380372010056PAC01	Feb 25, 2010	4, 8, 16, 32, 48, 64, 96, Season	None	160
LT50380372010104PAC02	Apr 14, 2010	4, 8, 16, 32, 48, 64, 96, Season	None	208
LT50380372010120PAC01	Apr 30, 2010	4, 8, 16, 32, 48, 64, 96, Season	Some	224
LT50380372010136PAC01	May 16, 2010	NA	None	240
LT50380372010168EDC00	Jun 17, 2010	NA	None	272

LT50380372010184EDC00	Jul 3, 2010	NA – Monsoon Base	None	288

2010-2011: Total Precip (Oct 1 – Mar 31): 39.9mm (Virtual Grid: 269218)				
LT50380372010248PAC01	Sep 5, 2010	2010 Base	None	0
LT50380372010280PAC01	Oct 7, 2010	4, 8, 16, 32, Season	Some	32
LT50380372010344EDC00	Dec 10, 2010	4, 8, 16, 32, 48, 64, 96, Season	None	96
LT50380372011027EDC00	Jan 27, 2011	4, 8, 16, 32, 48, 64, 96, Season	None	144
LT50380372011043PAC01	Feb 12, 2011	4, 8, 16, 32, 48, 64, 96, Season	None	160
LT50380372011059PAC01	Feb 28, 2011	4, 8, 16, 32, 48, 64, 96, Season	None	176
LT50380372011075EDC00	Mar 16, 2011	4, 8, 16, 32, 48, 64, 96, Season	None	192
LT50380372011091PAC01	Apr 1, 2011	4, 8, 16, 32, 48, 64, 96, Season	None	208
LT50380372011107PAC01	Apr 17, 2011	4, 8, 16, 32, 48, 64, 96, Season	None	224
LT50380372011123PAC01	May 3, 2011	NA	None	240
LT50380372011155PAC01	Jun 4, 2011	NA	None	272
LT50380372011171PAC01	Jun 20, 2011	NA – Monsoon Base	None	288

The following section expands upon the Methods section described in the main document and reflects the workflow shown in Figure 3. For a list of all data used in these analyses, refer to Appendix A: Tables 5 & 6. The mean NDVI value of the top ten percent (MTT) along each riparian area polygon (RAP) were calculated along the subtracted NDVI Landsat scenes (ΔNDVI-S) for both monsoon and winter dates. Coefficient of variation (CV) was used to determine the spatial uniformity and temporal variability of the changes in monsoon season NDVI over the 26 year study period. Correlation analysis were used to relate precipitation derived from radar instruments to increases in NDVI over the course of the winter rainy season. A final analysis was created that combined the monsoon and winter season analyses.

Riparian Area Polygons (RAPs)

Stream reaches were created for the SERDP RC-1727 funded project (Levick et al., 2015). They were originally derived from the NHDPlus Version 2 (V2) dataset downloaded from the Horizon Systems website (www.**horizon**-systems.com/**nhdplus/**) for the Lower Colorado (Vector Processing Unit 15). Using ArcMap 10.2, the NHDPlus V2 flowline layer was split into 2,843 reaches at approximately 1km in
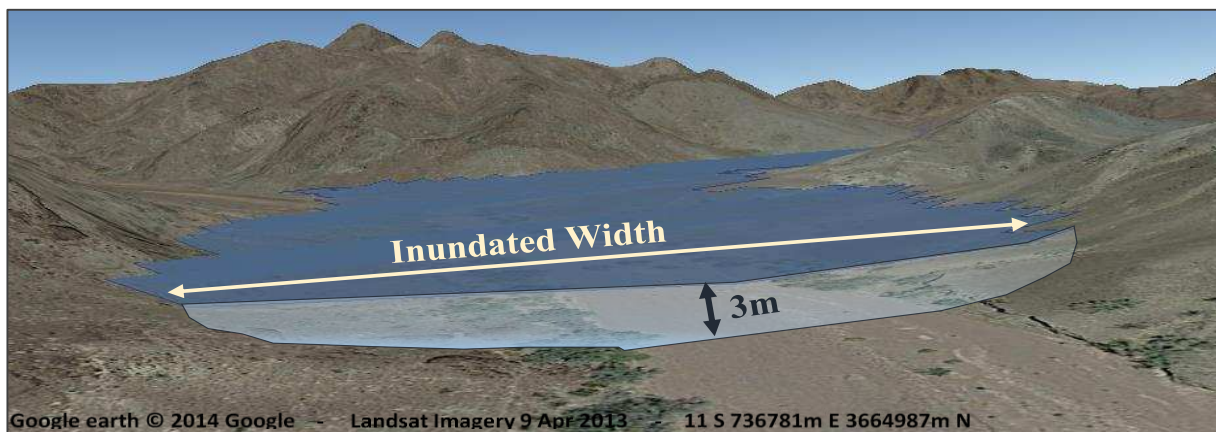

Figure 16: Representation of the 3m inundated Riparian Area Polygons (RAPs).

length. To achieve the riparian area along each reach, the 2,843 reach layer was buffered to 200m on either side of the flowline. The unbroken flowline layer was inundated to 3m using the HGVC (Hydro-Geomorphic Valley Classification) extension tool (Carlson E.A., 2009) with a 10m DEM in ArcMap 10.2. The 200m buffered reach layer was clipped back to the 3m inundated layer. Nearby reaches and areas of confluences had to be manually edited to remove the excess areas. This new layer was used to represent the riparian areas along the NHDPlus V2 flowline layer and was used as the spatial unit in this analysis (RAP; Figure 16).

Landsat TM Imagery

Landsat 5 Thematic Mapper (TM) has been an exceedingly useful tool as it provided imagery at 16 day intervals and in 7 wavelengths for nearly 27 years that was decommissioned in November of 2011. Landsat 5 TM is free to the public and has a pixel resolution of $30m^2$. Landsat 7 TM is the next generation and was launched in 1999. Landsat 7 TM is very comparable to Landsat 5 TM. From 1999 to 2003, it successfully collected images until the Scan Line Corrector instrument failed in May of 2003. Scenes from years 2000 to 2002 were incorporated into this analysis to replace inadequate Landsat 5 TM images. Scenes from Landsat 5 & 7 TM: Path 38, Row 37 were downloaded via GlobeVis (http://glovis.usgs.gov/) for pre- and post-monsoon season and winter dates. Acquisition dates for each analysis are shown in Figure 17 and 18.

Many useful indices have been developed from the bands associated with Landsat satellites; however, NDVI has proven to be a valuable and simple index that has been used in combination with many ecological and remote sensing inquires. NDVI takes advantage of the chlorophyllic processes by combining the Red and NIR bands where plant material reflects the NIR wavelengths while the red wavelengths are absorbed by chlorophyll (Nicholson & Farrar, 1994; Pettorelli et al., 2005; Brown et al., 2006). The difference between these two wavelengths divided by the sum calculates the NDVI value
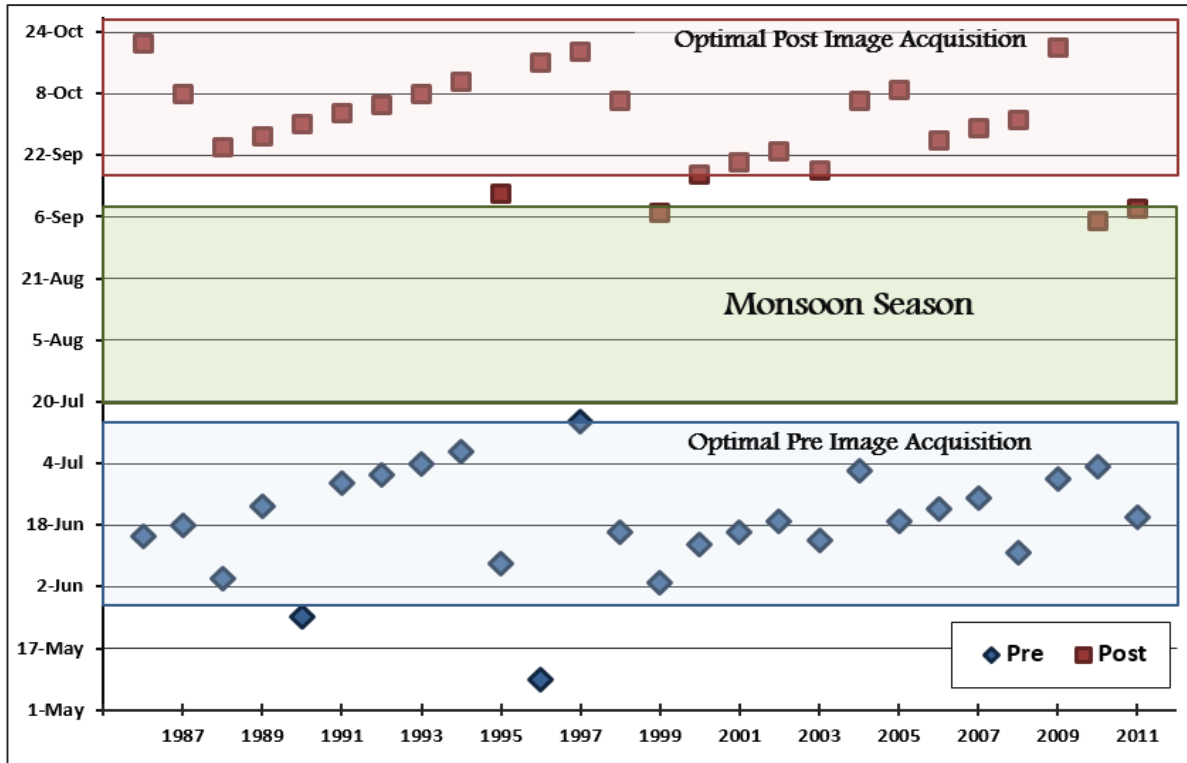
Figure 17: Pre- and post-monsoon season Landsat image selection. All scenes were captured from the Landsat 5 TM satellite platform except from 2000 to 2002 that were captured from Landsat 7 TM.
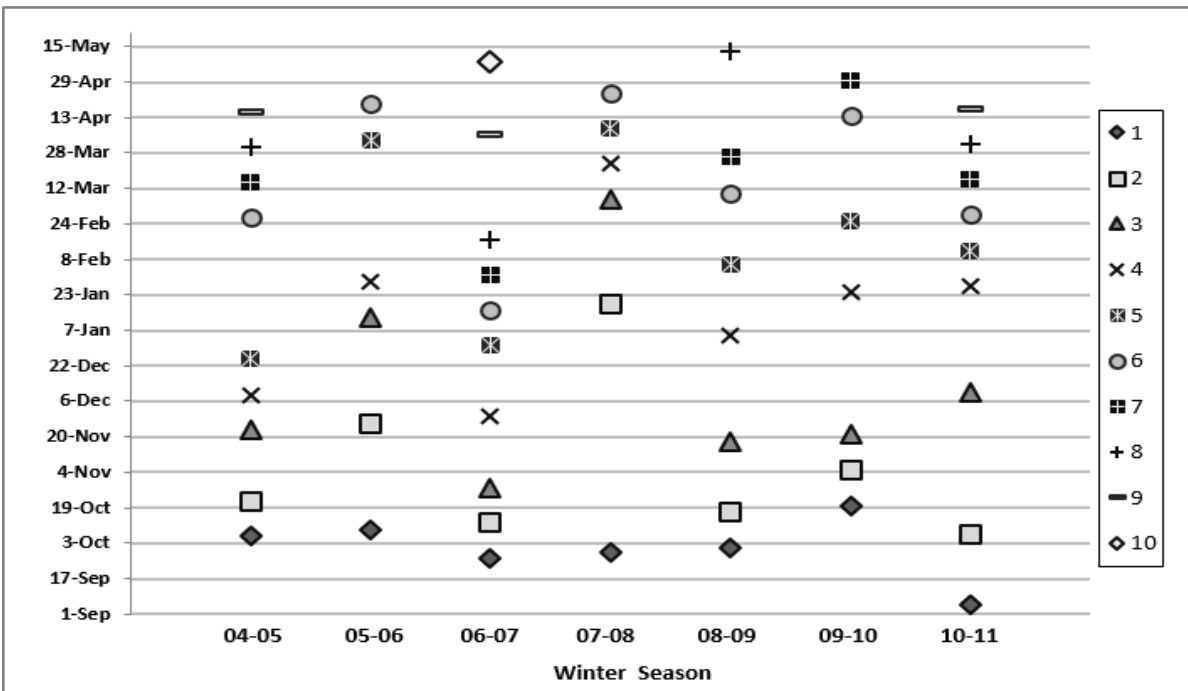
Figure 18: Frequency and distribution of Landsat 5 TM dates for the winter NDVI analysis. Base dates are shown as #1. Because Landsat 5 TM has a 16d temporal resolution, these dates are in 16d intervals or a multiple of 16. Skipped days are the result of heavy cloud cover. Low cloud cover dates were included.

and has been shown to map vegetation via chlorophyllic content around the globe (Pettorelli et al., 2005; Brown et al., 2006). Other vegetation indices exist and have been used in replacement of NDVI, such as MSAVI and MSAVI2 (Qi et al., 1994). Since this research is looking at change detection instead of vegetation classification, NDVI is used instead of MSAVI2 which takes into account regions of bare soil and has a more complicated equation.

All Landsat images were processed in ENVI 5.0 (*Radiometric Calibration for Reflectance* and *Dark Object Subtraction* were applied to all scenes). Each image was then uploaded in ARCMap 10.2. All monsoon season scenes chosen lacked clouds. The post-monsoon season scene served as the base winter scene for winters beginning in 2004 through 2010. When clouds were present in the subsequent winter scenes, these areas were removed. The following steps were applied to each scene in this order and the resulting monsoon ΔNDVI-S's are shown in Figure 7 (the winter ΔNDVI-S are not shown here).

1) *NDVI Calculation*

   A Model Builder tool was created using Raster Calculator Tool with the following equation:

   ("%NIR Band%" - "%Red Band%") / ("%NIR Band%" + "%Red Band%")

2) *Extraction of Study Area and Reduction of Cell Size*

   Each scene was reduced to the study area using the *Extract by Mask* tool with a constant boundary layer. The cell size of each pixel was reduced to 5m before running the tool using a common NDVI image so that each cell lined up properly (*Environment* tab: *Raster Analysis*: *Cell Size = 5;* this step does not modify any of the NDVI values). If clouds were present, the regions were masked out.

3) *Change in NDVI Scene (ΔNDVI-S)*

   The later scene was subtracted from the base scene using the *Raster Calculator* tool (Post-Monsoon – Pre-Monsoon or Later Winter Date – Base Winter Date).

4) *Extract the values of ΔNDVI-S to RAPs*

Each ΔNDVI-S was reduced to every RAP using the *Extract by Mask* tool then converted

into an ASCII text file by using the *Raster to Ascii* tool (A model builder tool was created

to iterate through the 2,843 RAPs).

5) *Calculate the mean value of the Change in NDVI for the Top Ten Percent of the pixels within*

each RAP (MTT value per RAP per ΔNDVI-S)

A Python Script was created (by Eric Schmidt) to extract all values of each RAP ASCII

text file for each ΔNDVI-S and subset the top 10% (rounding down; MTT). The mean

value was calculated off this subset and aggregated into a single CSV file for each

ΔNDVI-S (Figure 19). The code used is as follows:

```python
import os
import numpy as np

folder = "select local folder Path"
value_stuff = {}

for path,dir,files in os.walk(folder):
    output_file = os.path.join(path, 'MTT_values.csv')
    with open(output_file, 'wb') as out_file:
        out_file.write('Rast_ID, TopTenMEAN {}'.format(os.linesep))
        for file in files:
            if file.endswith('.txt'):
                full_file = os.path.join(path, file)
                print full_file
                data_values = []
                with open(os.path.join(path,file), 'rb') as data_file:
                    for j,line in enumerate(data_file):
                        if j > 5:
                            my_vals = line.split()
                            data_values.extend([float(item) for item in my_vals if float(item) != -9999.0])
                data_values.sort()
                num_values = len(data_values)
                ix_top_values = int(np.floor(num_values*.9))
                print ix_top_values
                top_values = data_values[ix_top_values:]
                mean_value = np.mean(top_values)
                value_stuff[full_file] = mean_value
                print '{} file has mean {}'.format(full_file, mean_value)

                out_file.write('{},{}{}'.format(file.split('.')[0], mean_value, os.linesep))
```
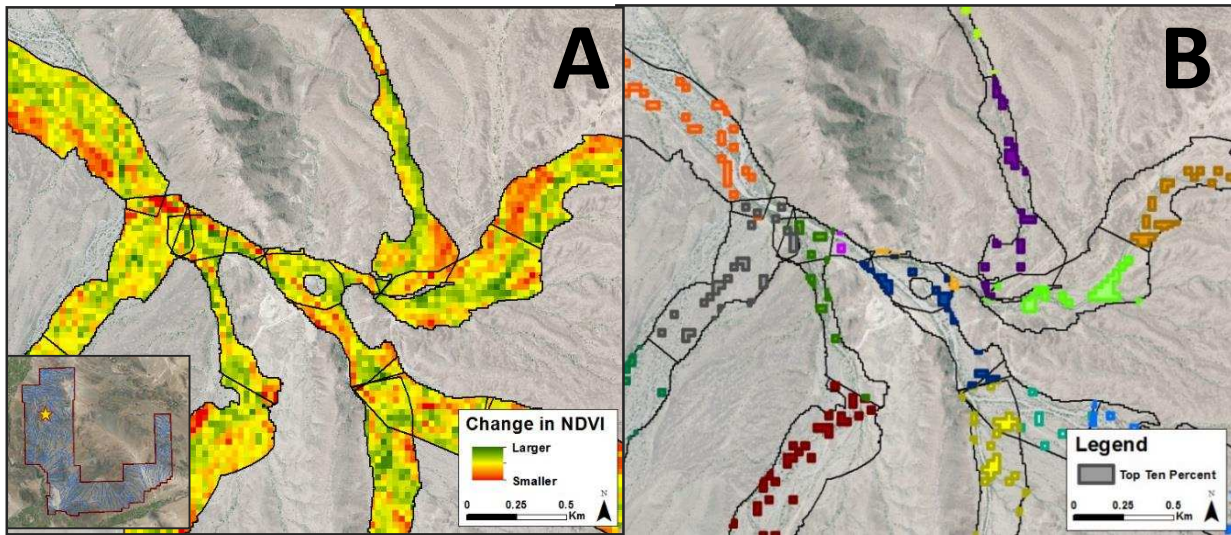
Figure 19: These figures demonstrate the methods for extracting the MTT NDVI values within each reach. For each ΔNDVI-S, each RAP was extracted separately by using individual RAP shapefiles in ArcMap 10.2 (shown in Figure A), then converted into an ASCIIi text file that contains every pixel value within the RAP. The values of the pixels representing the Top 10% are depicted in Figure B. These values were extracted from the ascii text file using the python code and the MTT was calculated. This was done for every ΔNDVI-S at every RAP unit.

NEXRAD Data (Winter only)

In an effort to reduce the amount of data, the version of the NEXRAD virtual grid layer that was created by Russell Lyon (Lyon R., 2013) for YPG was used where nine NEXRAD virtual rain gauge grids were averaged together creating a mean precipitation value for each day that spanned over the 144km^2 grid. Although this is a considerably large area, when considering the storm type (i.e. large frontal storms), this area is reasonable. This created a total of 60 grids that covered the study area. These grid layers were linked to the reaches at YPG using the *Spatial Join* tool in ARCMap 10.2. This allowed each reach to be connected to the daily NEXRAD and PRISM precipitation data.

Daily precipitation estimates of NEXRAD data were tabulated using Microsoft Excel. For each Landsat scene (excluding the Base scene), the sum of precipitation for the previous time periods at the 4, 8, 16, 32, 48, 64, 96 day and Seasonal time steps were calculated for each year. Earlier winter scenes

had null values in the longer time steps when the time step went earlier than the base image.

Additional parameters were calculated describing the amount of rain events of >5mm and >10mm that

occurred in the 32, 48, and 96d time steps. Precipitation was also totaled between ranges 8-16d, 16-

32d, 16-48d, 32-64d, and 48-96d before each scene.

PRISM Mean Temperature Data (Winter only)

Temperature data were also downloaded through the PRISM Climate Group (http://www.prism.

oregonstate.edu/). This research used daily mean temperature that were downloaded as ASCII files in

units of degrees Celsius with a spatial resolution of $4km^2$. The temperatures for each day during the

study period were averaged over the 60 NEXRAD grids at $12km^2$ resolution. The daily mean

temperature values for each winter season were tabulated. Microsoft Excel was used to calculate the

mean temperature values at the 4, 8, 16, 32, 48, 64, 96 day and Seasonal time steps previous to each

Landsat image. Earlier winter scenes had null values in the longer time steps.

Combining NEXRAD, PRISM, and Landsat 5 TM Data (Winter only)

The aforementioned data was combined into a table for each winter season. This was done by

creating two unique identifiers where the RAP identifier and the Gauge identifier were linked to the date

of each winter Landsat scene (Base scene excluded). RAPs and Gauge identifiers were repeated to fulfill

every winter Landsat date. All data were now joined together between the two unique identifiers and

organized into a single database table per winter season with the following column headers:

Date: Landsat scene date (more recent date)
UniqID: Modified UniqueID containing the Landsat scene date.
GaugeUniqID: Modified GaugeID containing the Landsat scene date
UniqueID: Original SERDP RC-1727 Unique Identifier
GaugeID: Unique Identifier for the NEXRAD grid layer combining 9 grids into one 12x12km grid (n=60)
MTT: Mean NDVI of the Top 10% (MTT) between the Landsat scene and the base scene (ΔNDVI-S)
Precip4d: Previous 4 day precipitation totals from Landsat scene
Precip8d: Previous 8 day precipitation totals from Landsat scene
Precip16d: Previous 16 day precipitation totals from Landsat scene
Precip32d: Previous 32 day precipitation totals from Landsat scene
Precip48d: Previous 48 day precipitation totals from Landsat scene
Precip64d: Previous 64 day precipitation totals from Landsat scene
Precip96d: Previous 96 day precipitation totals from Landsat scene
PrecipSeason: Precipitation totals between Landsat scene and the Base scene
Temp4d: Previous 4 day temperature means from Landsat scene
Temp8d: Previous 8 day temperature means from Landsat scene
Temp16d: Previous 16 day temperature means from Landsat scene
Temp32d: Previous 32 day temperature means from Landsat scene
Temp48d: Previous 48 day temperature means from Landsat scene
Temp64d: Previous 64 day temperature means from Landsat scene
Temp96d: Previous 96 day temperature means from Landsat scene
TempSeason: Temperature means between Landsat scene and the Base scene
Days5mm32d: Number of the previous 32 days where precipitation sums were 5mm or greater
Days5mm48d: Number of the previous 48 days where precipitation sums were 5mm or greater
Days5mm96d: Number of the previous 96 days where precipitation sums were 5mm or greater
Days10mm32d: Number of the previous 32 days where precipitation sums were 10mm or greater
Days10mm48d: Number of the previous 48 days where precipitation sums were 10mm or greater
Days10mm96d: Number of the previous 96 days where precipitation sums were 10mm or greater
Range8-16d: Total precipitation between 8 and 16 days prior to the Landsat scene
Range16-32d: Total precipitation between 16 and 32 days prior to the Landsat scene
Range16-48d: Total precipitation between 16 and 48 days prior to the Landsat scene
Range32-64d: Total precipitation between 32 and 64 days prior to the Landsat scene
Range48-96d: Total precipitation between 48 and 96 days prior to the Landsat scene

References

Brown, M. E., J. E. Pinzón, K. Didan, J. T. Morisette, and C. J. Tucker. 2006. Evaluation of the consistency of long-term NDVI time series derived from AVHRR, SPOT-Vegetation, SeaWiFS, MODIS, and Landsat ETM+ sensors. *Geoscience and Remote Sensing, IEEE Transactions on* **44(7)**:1787-1793.

Carlson, E. A. 2009. Fluvial riparian classification for national forests in the western United States. M.S. Thesis. Colorado State University.

Levick, L., Hammer, S., Lyon, R., Murray, J., Birtwistle, A., Goodrich, D., Bledsoe, B., Guertin, P., and M. Laituri. 2015. An ecohydrological approach to managing intermittent and ephemeral streams on Department of Defense lands in the Southwestern United States. Department of Defense, Strategic Environmental Research and Development Program (SERDP), Project RC-1727.

Lyon, R. 2013. Using rainfall-runoff models to characterize the flow regime of desert streams in the US Southwest. Russ Lyon, M.S. Thesis, University of Arizona, Tucson, AZ.

Nicholson, S. E., and T.J. Farrar. 1994. The influence of soil type on the relationships between NDVI, rainfall, and soil moisture in semiarid Botswana. I. NDVI response to rainfall. *Remote Sensing of Environment* **50(2)**:107-120.

Pettorelli, N., J. O. Vik, A. Mysterud, J.M. Gaillard, C.J. Tucker, and N. C. Stenseth. 2005. Using the satellite-derived NDVI to assess ecological responses to environmental change. *Trends in Ecology & Evolution* **20(9)**:503-510.

Qi, J., A. Chehbouni, A. R. Huete, Y. H. Kerr, and S. Sorooshian. 1994. A modified soil adjusted vegetation index. *Remote Sensing of Environment* **48(2)**:119-126.

APPENDIX C: INSTRUMENT COMPARISON AND LINEAR REGRESSIONS

Precipitation Data and Preparation for Instrument Comparison

The first task of this research was to acquire the Rain Gauge, NEXRAD and PRISM data from the appropriate sources. Appendix A: Table 5 documents the data type, resolution, its use, and the source of each dataset. After the data were acquired the precipitation estimates were compared using Linear Regression for multiple years and divided between the two rainy seasons (monsoon and winter). This step was necessary to field check the radar data against the rain gauge sites within the YPG vicinity and determine if or when the radar data can be used as a surrogate dataset to the rain gauge data in order to estimate the spatial and temporal variability of vegetation response to precipitation in semi-arid landscapes. RStudio 3.1.1 (R Core Team, 2014) was used to run all statistical analysis.

Rain Gauge Data

Rain gauge data exists for YPG in two separate washes from the SERDP: RS-1725 funded research and from the GHCN dataset (Figure 20). Yuma Wash (Figure 21) is located in the south western portion of the installation and had five separate rain gauge sites; though only three gauges were used in this study and were between 2 and 3.5km away from each other. Mohave Wash is located in the north western portion of the installation and had a total of four rain gauge stations, although only two were used in this analyses: MBA and MBD (Figure 24). All rain gauge sites were activated in 2011 and decommissioned in late spring of 2014. Each site measured precipitation with a TE 525 Tipping Bucket rain gauge system at 0.254mm per tip rate. The Yuma and Mohave wash rain gauge sites were in working order for most of the period, but contain scattered periods of disuse.
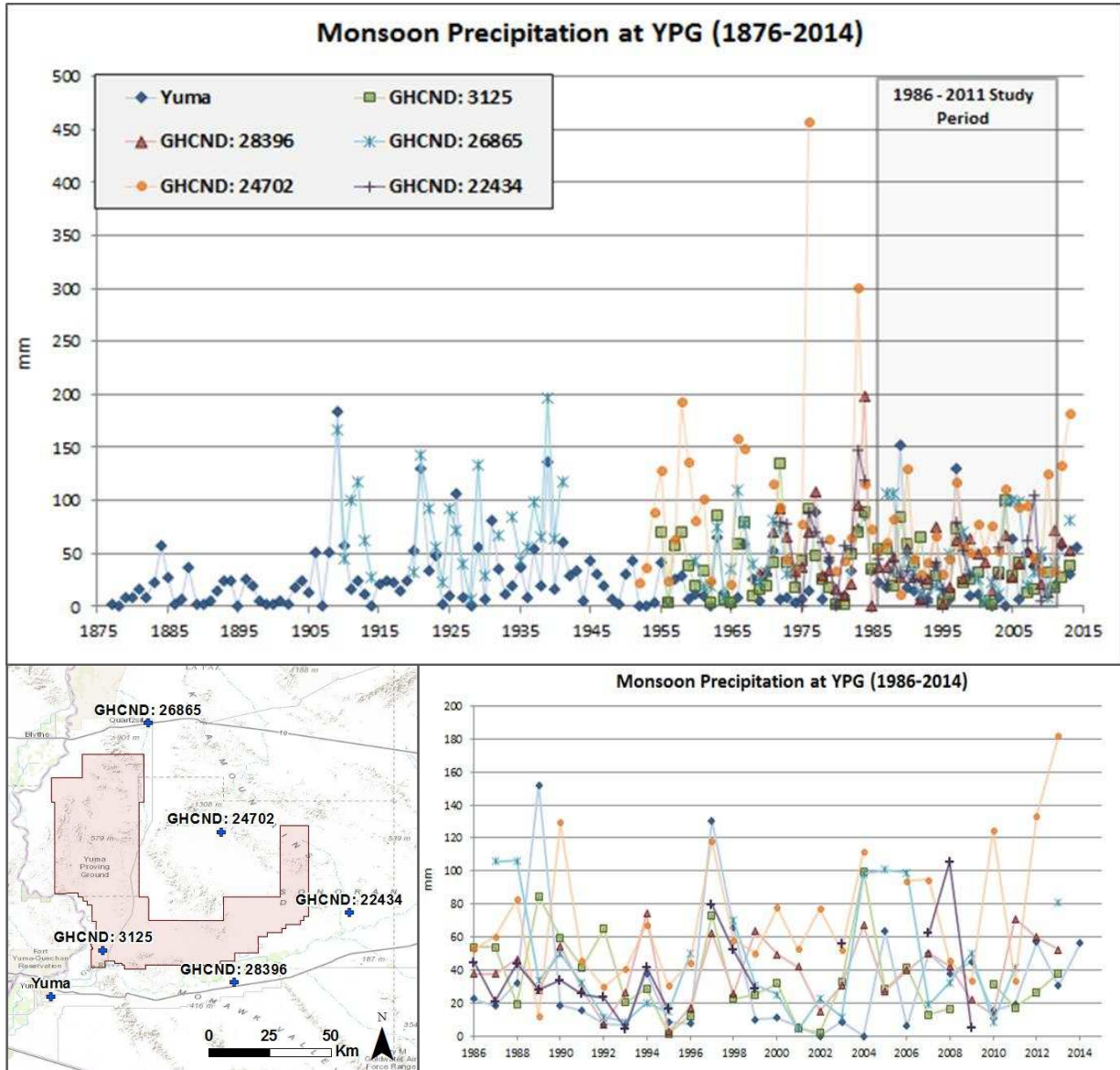
Figure 20: Historic monsoon precipitation at YPG. Yuma data acquired through the National Weather Service Forecast Center (http://www.wrh.noaa.gov/twc/monsoon/monsoon_yum.php); GHCN data acquired though the NOAA National Climatic Data Center (http://www.ncdc.noaa.gov/data-access/land-based-station-data).

NEXRAD Data

NEXRAD data are a type of Doppler radar that can measure precipitation amounts from fixed

stations that are located throughout the US and estimates precipitation up to a distance of 230km away
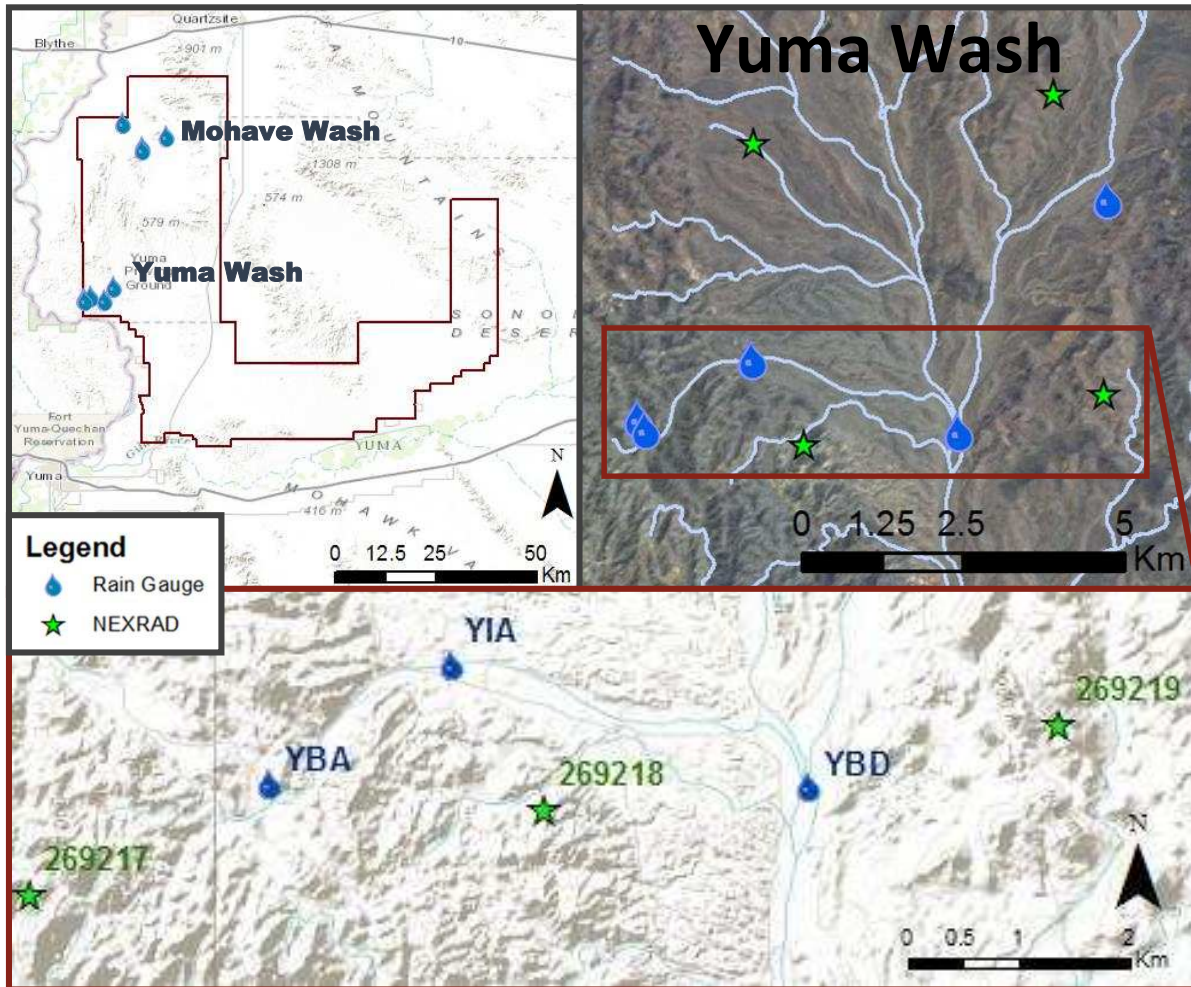
Figure 21: Location of Rain Gauge sites at Mohave and Yuma Wash.

(Fulton, 2002). Radar emits a signal that increases in altitude as you move further from the station and

samples higher altitudes that do not necessarily represent what is occurring on the surface. At mid to

far ranges (100km and beyond), NEXRAD stations may actually measure more rainfall than is present

and therefore have a tendency to create a 'range-related bias' (Fulton, 2002). Previous versions of

NEXRAD (Stage II & III) data led to the creation of the Multisensor Precipitation Estimator (MPE) that

combines Stage II data and independent rain gauge data with satellite precipitation data (GOES Satellite

imagery) to produce more accurate precipitation estimates by minimizing local bias errors and

enhancing coverage thru decreasing beam blockage and reducing spatial uniformity with rain gauge data

(Fulton, 2002). Mountain Mapper is similar to MPE, but is used in areas that are affected by orographic

precipitation, commonly in the western US during winter seasonal precipitation (Schaake et al., 2004).

NEXRAD MPE and Mountain Mapper products are processed through the National Weather Service:

River Forecast Centers since 2004. The precipitation data are delivered in a 16km^2 resolution in inches

and are combined to create the Stage IV NEXRAD product for the Contiguous US.

The NEXRAD station YUX covers most of YPG and resides southwest of the boundary (Figure 22).

The rain gauge sites for Yuma Wash were located in the Best Radar Coverage area (where the radar

station is able to capture weather as low as 4,000ft) and were approximately 80km away, while Mohave

Wash rain gauge sites were located in the Better Radar Coverage area (where the radar station is able to

capture weather not lower than 6,000ft) and were around 125km away. The NEXRAD data were

downloaded from the National Weather Service website (water.weather.gov/precip/p_download_new)
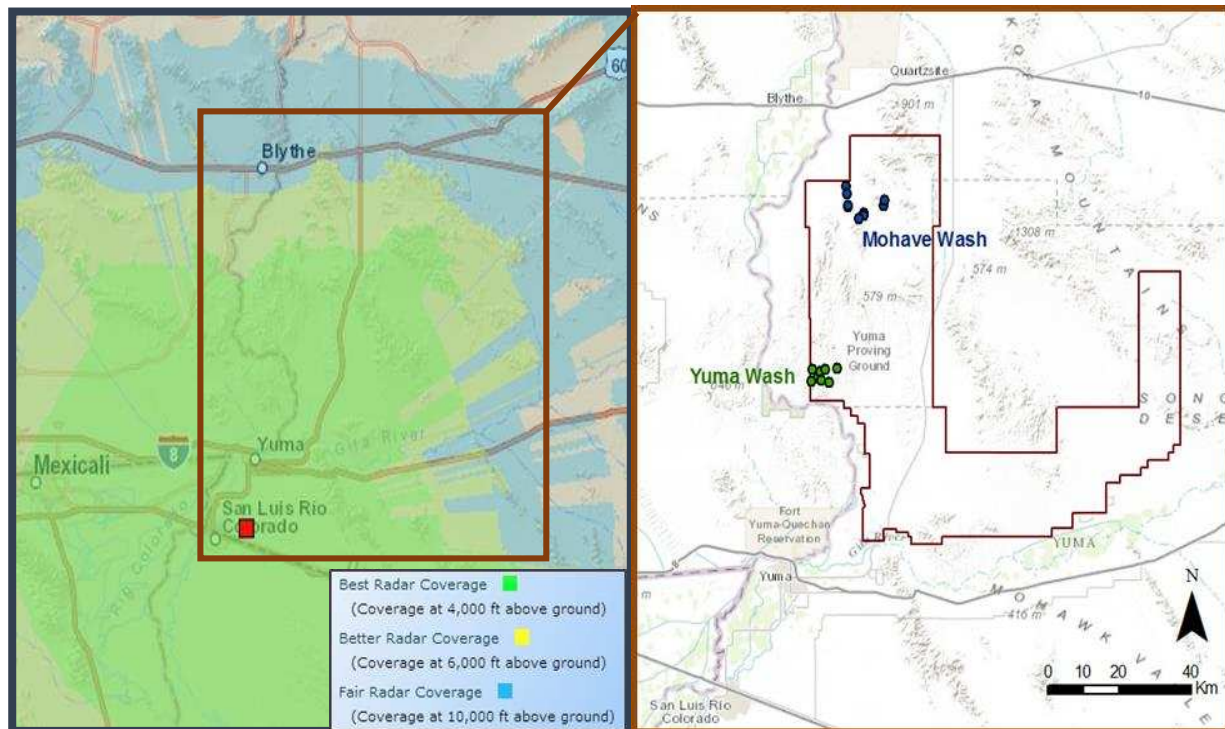
Figure 22: Left: NEXRAD extent and coverage variability. **Right:** Location of rain gauge sites. The blue sites (Yuma Wash) fall within the Best Radar Coverage Band (Coverage at 4,000ft and above the ground) and the red sites (Mohave Wash) are on the edge of the green and yellow band (between 4,000ft and 6,000ft above the ground). Left image source: *http://gis.ncdc.noaa.gov/map/viewer/#app=cdo&cfg= radar&theme=radar&display=nexrad*

by using a python script created by Mehmet Ercan (http://mehmetbercan.com/scripts/scriptsGIS.html)
that downloads and clips the NEXRAD data after January 2, 2005 in ArcMap 10.2. It was further
processed into tabular format of daily precipitation totals per each virtual grid point in mm. These data
were compared to the PRISM data and the acquired Rain Gauge data for the closest NEXRAD virtual rain
gauge daily precipitation values.

PRISM Data

Since the NEXRAD data that were used started on January 2, 2005, during a particularly wet winter
season, PRISM data were used to estimate the rainfall previous to January 2, 2005 for that season. The
PRISM data were also compared to the 2011-2014 rain gauge data to compare all datasets. PRISM data
were downloaded through the PRISM CLIMATE GROUP (http://www.prism.oregonstate.edu/) and came
in daily ASCII files for the contiguous United States. The resolution is the same as NEXRAD data at $16km^2$
and are in units of mm.

Inverse Distance Weighting

The Inverse Distance Weighting method was applied separately to each of the rain gauge sites and
the associated NEXRAD/PRISM grid cell centers in order to assign a distance weighted precipitation
estimate for the radar data at each rain gauge location. The equation used to assign these weights is
shown in *Equation 1;* where w_i is the weight of the radar grid cell depending on the distance to the rain
gauge site, *n* is the total number of grids that were used to determine the precipitation, and d_i is the
distance between the grid center point and the rain gauge:

$$\textbf{Equation 1:} \qquad w_i = \frac{1/d_i}{\sum_{i=1}^{n} 1/d_i}$$

Radar precipitation estimates at the rain gauge location were determined for each day using the following equation where P_e = precipitation estimate, n = total grid cells used, p_i = precipitation at that grid cell and w_i is the weight that is assigned to each grid in *Equation 1:*

$$\text{Equation 2:} \qquad P_e = \sum_{i=1}^{n} p_i w_i$$

Precipitation Instrument Comparative Analysis

Several linear regression models were conducted in RStudio (R Core Team, 2014) to investigate the statistical difference between the rain gauge sites in Yuma and Mohave Wash at YPG. The adjusted R^2 values and slopes are included below. When the adjusted R^2 values approach 1, then the two different data sources indicate synchronism. When the slope is near 1 then the data sources can be said to show similar rainfall totals. When the rain gauge and the NEXRAD precipitation data show these trends, then the radar data may be considered a reliable surrogate for rain gauge data.

NEXRAD and PRISM Comparison

Even though NEXRAD and PRISM data are on similar scales, there still are some discrepancies. By comparing the NEXRAD and PRISM data at one virtual rain gauge site in Yuma Wash over 9 years, I found the data correlates 64% of the time (*Average Adj R²*, Table 7). Neither

Table 7: NEXRAD - PRISM comparison considering 9 consecutive years of precipitation data. Here, the NEXRAD data were plotted on the Y-axis and the PRISM on the X-axis, thus slopes less than 1 suggest that the PRISM dataset is measuring more precipitation than the NEXRAD data and vice versa for slopes greater than 1.

Year	Slope	Adj R²	Year	Slope	Adj R²
2005	0.67	0.42	**2010**	1.05	0.86
2006	0.80	0.30	**2011**	0.87	0.46
2007	1.90	0.94	**2012**	1.24	0.77
2008	0.92	0.47	**2013** (Jan – Aug)	0.88	0.80
2009	1.96	0.77	**Average**	**1.00**	**0.64**

the NEXRAD nor the PRISM data are considered to be ground truth, so this analysis is merely a comparison between these data sources.

Rain Gauge to Radar Comparison: Yuma Wash

When comparing the data for Yuma Wash rain gauge sites to the NEXRAD radar data, many of the rain events were off by one day and produce poor correlation results. The Linear Regression results that are shown in Tables 8 & 9 and Figures 23 & 24 used data that I have altered to combine consecutive day rain events - meaning that the NEXRAD data were typically moved to the day before or at times, when the NEXRAD data documented consecutive day rain events, the precipitation amounts were totaled into single day events. This is acceptable because the NEXRAD data uses Greenwich Mean Time for the start and end of a day, therefore any precipitation events that occurred after 6 pm at YPG were recorded the day after.

The rain gauge and the radar data were compared in two different ways using linear regressions. The first analyses included precipitation data from the entire year (Table 8) and received poor adjusted R^2 results (mean NEXRAD: 0.18 and mean PRISM: 0.21). The second analysis excluded the summer months that are affected by monsoon storms (May 1 to September 30), therefore only examining winter frontal storms (Table 9 & Figure 23). The NEXRAD vs rain gauge comparison using winter precipitation data received the greatest adjusted R^2 value (0.81) thus suggesting that NEXRAD

Table 8: Entire year of precipitation data comparison for 2011-2013. Here, the radar (NEXRAD and PRISM) data were plotted on the Y-axis and the rain gauge data on the X-axis. All slopes are less than 1, which suggest that the rain gauge data typically measures more precipitation than the radar data. Dates with no recorded precipitation in either of the three datasets were removed from the regression analyses.

Rain Gauge	Rain Events	Rain Gauge vs NEXRAD		Rain Gauge vs PRISM	
		Slope	Adj R^2	Slope	Adj R^2
YBA	90	0.17	0.22	0.17	0.23
YIA	81	0.15	0.17	0.16	0.23
YBD	44	0.14	0.16	0.18	0.18
Mean		**0.15**	**0.18**	**0.17**	**0.21**

data may be a usable surrogate to rain gauge data when investigating winter precipitation in semi-arid landscapes. The results also showed that NEXRAD is a better dataset than PRISM data (0.81 vs 0.69; Table 9) when plotted against the rain gauge data.

For each of the Rain Gauge verse NEXRAD and the Rain Gauge

Table 9: Winter comparison of precipitation data for years 2011-2013 (October 1 - April 30). Since the radar (NEXRAD and PRISM) data were plotted on the Y-axis and the rain gauge data on the X-axis and all slopes are still less than 1 suggest that the rain gauge data typically measures more precipitation than the radar data. Dates with no recorded precipitation in either of the three datasets were removed from the regression analyses.

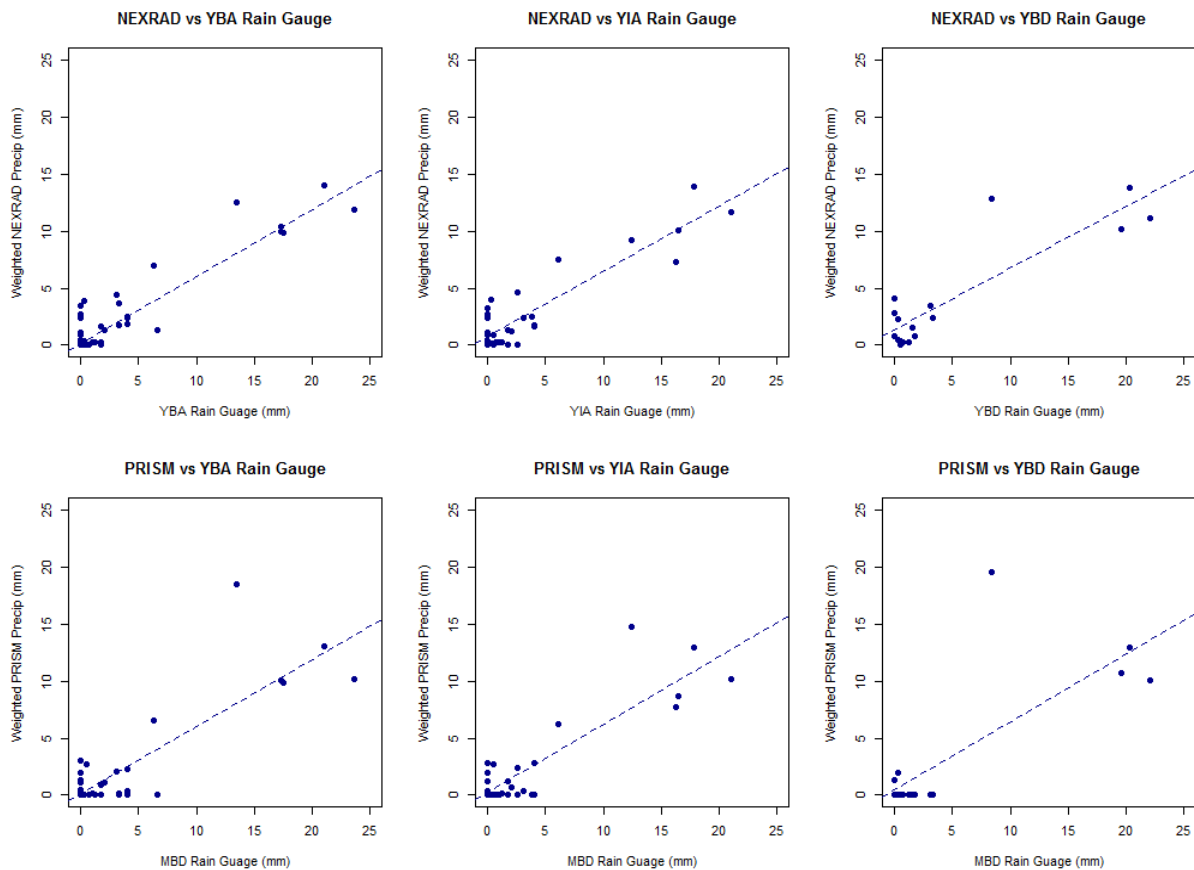| Rain Gauge	Rain Events	NEXRAD vs Rain Gauge		PRISM vs Rain Gauge	
		Slope	Adj R^2	Slope	Adj R^2
YBA	40	0.56	0.85	0.59	0.74
YIA	31	0.57	0.81	0.60	0.77
YBD	17	0.54	0.76	0.60	0.57
Mean		**0.56**	**0.81**	**0.60**	**0.69**

Figure 23: Plots for winter linear regression models at Yuma Wash looking at the NEXRAD – Rain Gauge and PRISM – Rain Gauge comparison.

69

verse PRISM comparisons, the slope of the linear regressions are all less than one (Tables 8 & 9). Since

the rain gauge data were plotted on the x-axis, a slope less than one indicates that the rain gauges

typically measures a larger amount of precipitation than the radar instruments, therefore indicating that

generally the radar data underrepresents the rainfall quantities by roughly 40% (NEXRAD: 0.56 and

PRISM: 0.60).

Rain Gauge and Radar Comparison: Mohave Wash

The linear regressions for Mohave Wash (Figure 24) which is 45km further away from the NEXRAD

station shows similar results compared to Yuma Wash. The average adjusted R² value for winter

precipitation is 0.84 with a slope at 0.63. These data suggest that NEXRAD data is an acceptable

replacement for rain gauge data at YPG for winter months.

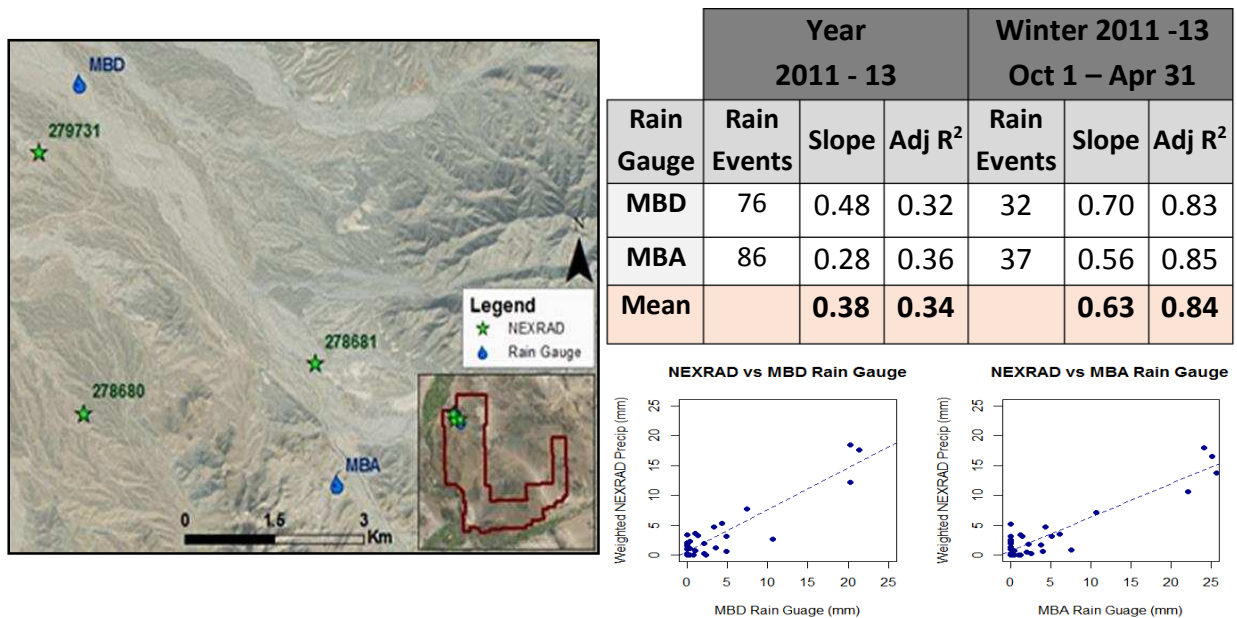| Rain Gauge	Year 2011 - 13			Winter 2011 -13 Oct 1 – Apr 31		
	Rain Events	Slope	Adj R²	Rain Events	Slope	Adj R²
MBD	76	0.48	0.32	32	0.70	0.83
MBA	86	0.28	0.36	37	0.56	0.85
Mean		0.38	0.34		0.63	0.84

Figure 24: Mohave rain gauge and NEXRAD sites with Linear Regression statistics. Plots are shown for the winter analyses only for years 2011-13. The mean slope and adjusted R² values for the winter analyses are 0.63 and 0.84, respectively. These values indicate good correlation between the rain gauges and the NEXRAD radar data for precipitation during winter months.

The linear regression of the larger NEXRAD grids (144km^2) to the GHCN Rain Gauge data showed

similar results for both the year and winter only analyses. These data appear to measure monsoon

season precipitation more accurately than the Yuma and Mohave sites (0.54), but less accurately for

winter precipitation (0.67). The differences in results from this dataset to Yuma and Mohave datasets

may be the result of the location, the agglomeration of 9 NEXRAD grids into one, or the increase in

temporal coverage. Nevertheless, these data supports that NEXRAD radar data is a suitable

replacement for rain gauge data during winter months at YPG.

Year 2008 - 13			Winter 2008 -13 Oct 1 – Apr 31		
Rain Events	Slope	Adj R^2	Rain Events	Slope	Adj R^2
107	0.49	0.54	52	0.49	0.67

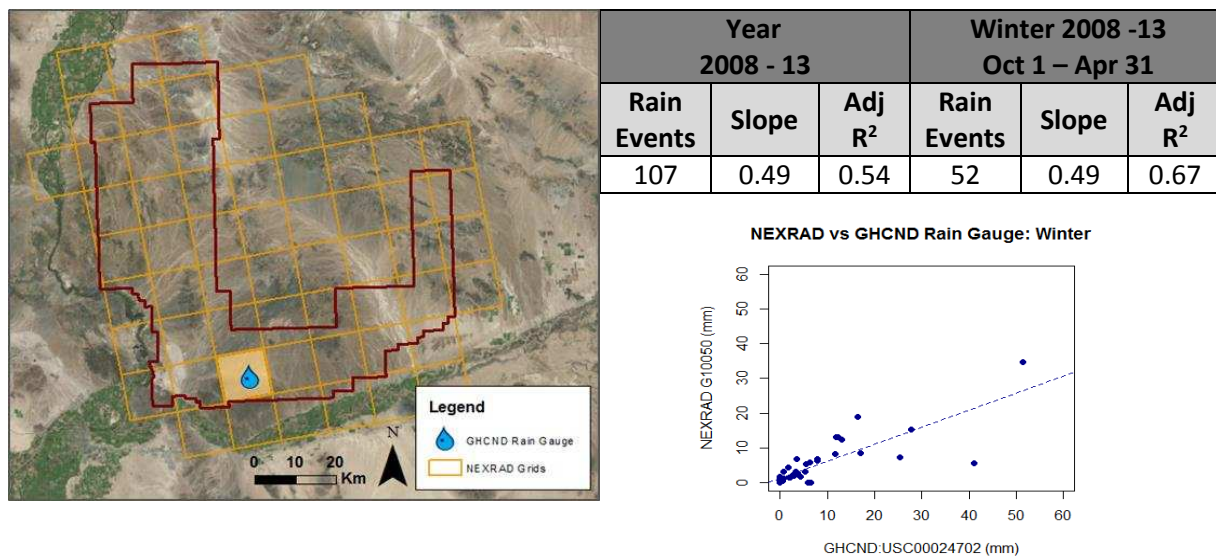**Figure 25:** Linear Regressions comparing a rain gauge with 9 combined 4 km^2 NEXRAD Grids, which make a larger 144km^2 grid. The adj R^2 for this comparison fell to 0.67 when comparing solely the winter data. When both seasons were considered, the adj R^2 reduced to 0.54. Slope averaged at 0.49 for both analyses and suggests that the NEXRAD instruments measure roughly 50% of the precipitation.

References

Fulton, R. A. 2002. Activities to improve WSR-88D radar rainfall estimation in the National Weather Service. In *Proceedings of the Second Federal Interagency Hydrologic Modeling Conference, Las Vegas, Nevada*. Subcommittee on Hydrology, Advisory Committee on Water Data, CD-ROM [Available online at http://nws.noaa.gov/ohd/hrl/ presentations /fihm02/pdfs/qpe_hydromodelconf_web.pdf]

R Core Team. 2014. R: A language and environment for statistical computing. R Foundation for Statistical Computing. Vienna, Austria.   Retrieved October 7, 2014. http://www.R-project.org/

Schaake, J., A. Henkel, and S. Cong. 2004. 5.3 Application of PRISM Climatologies for Hydrologic Modeling and Forecasting in the Western US.

APPENDIX D: WINTER NDVI-PRECIP-TEMP CHARTS AND TABLE OF PAIRED T-TESTS BETWEEN CONSECUTIVE DATES

Note that the NDVI Ranges are different for the 2004-05 and the 2005-06 Winters compared to the rest of the winters.

Winter NDVI-PRECIP-TEMP Data: 2004-05 Season
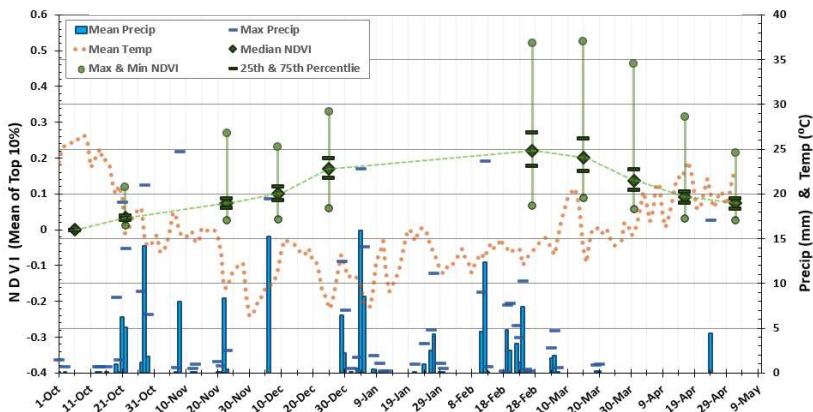
Winter NDVI-PRECIP-TEMP Data: 2005-06 Season
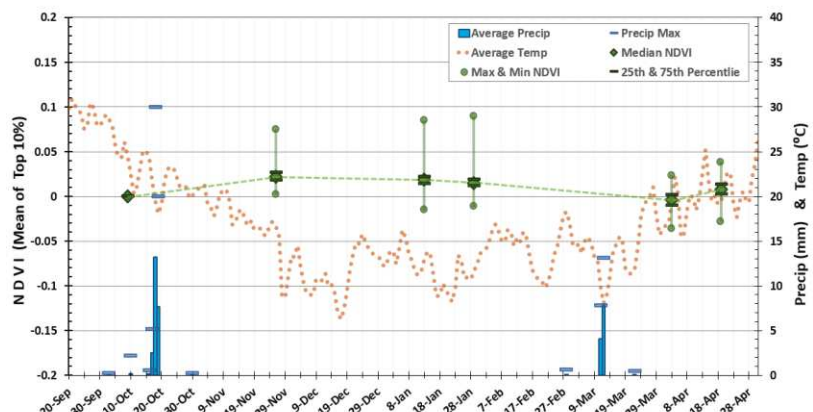
Winter NDVI-PRECIP-TEMP Data: 2006-07 Season
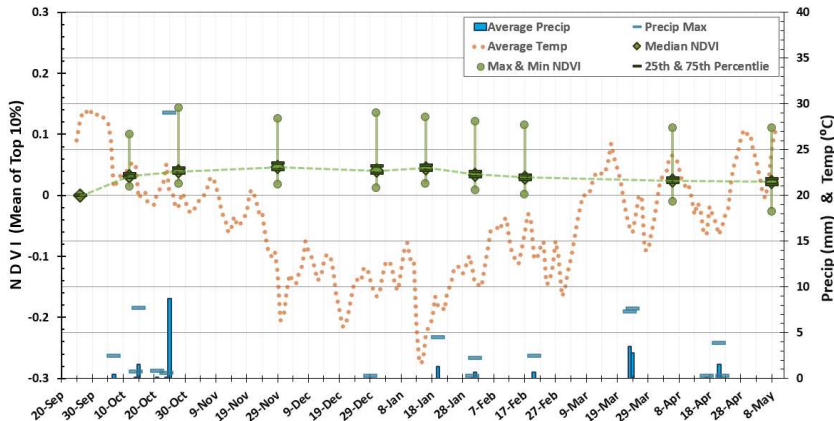
Winter NDVI-PRECIP-TEMP Data: 2007-08 Season
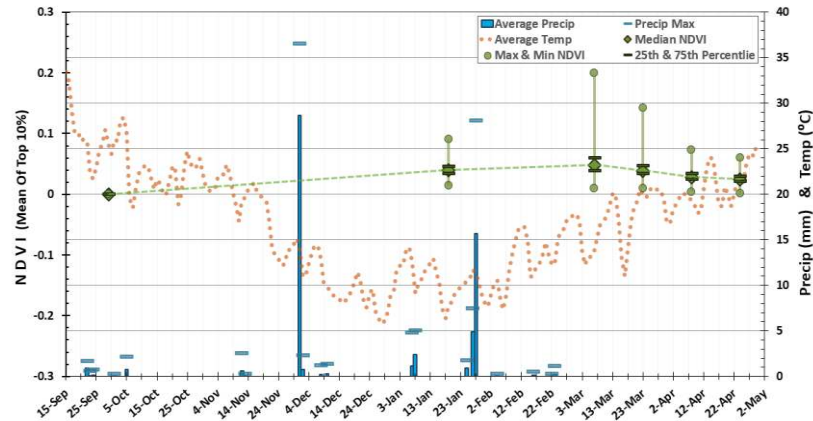
Winter NDVI-PRECIP-TEMP Data: 2008-09 Season
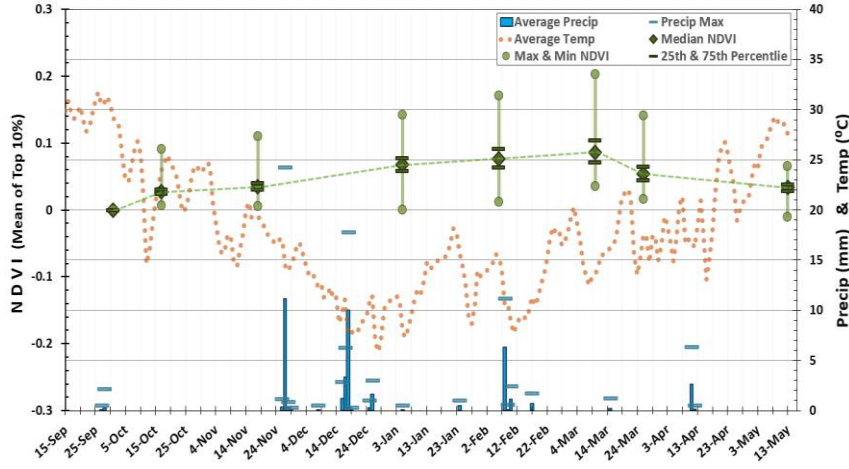
Winter NDVI-PRECIP-TEMP Data: 2009-10 Season
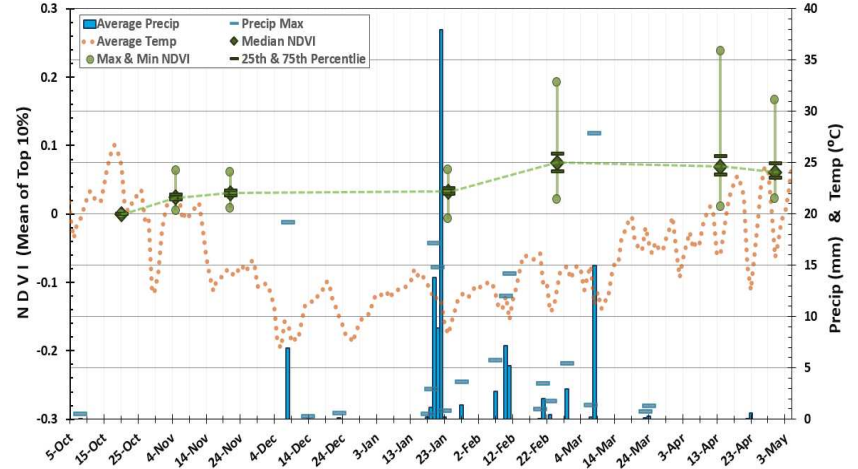
Winter NDVI-PRECIP-TEMP Data: 2010-11 Season
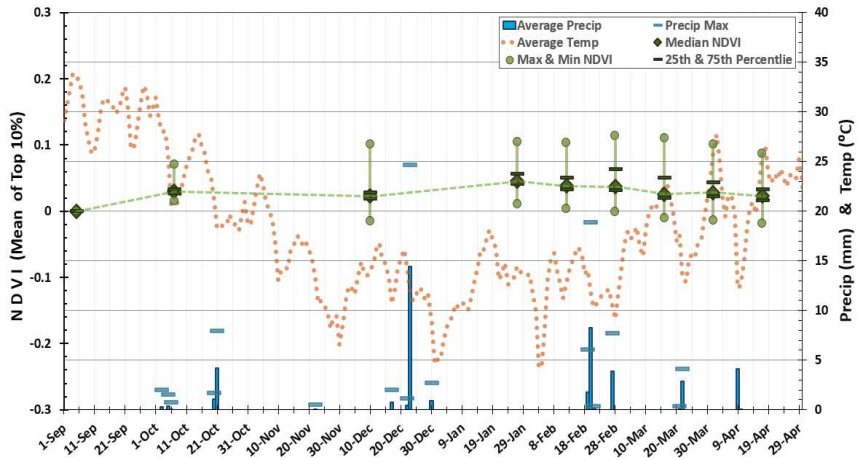
Mean Monthly Temperature for 2004-05 to 2010-11
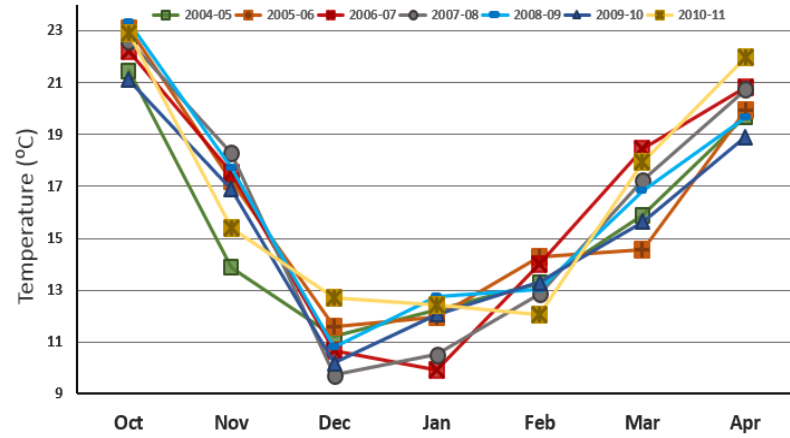
Table 10: Paired T-Tests between consecutive ΔNDIVI-S (ΔNDVI-S - 1 & ΔNDVI-S - 2) for each winter season, where N equals sample size, CI-1 and CI-2 are the lower and upper confidence intervals and the Test Estimate is the mean of the difference for Paired T-Test unless denoted by **††** where the Wilcoxon signed rank test with continuity correction was used and therefore the (pseudo)median is estimated. All but two tests were found to be statistically different (p-value = <<< 0.001) and are denoted by *****.

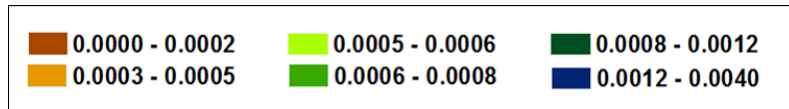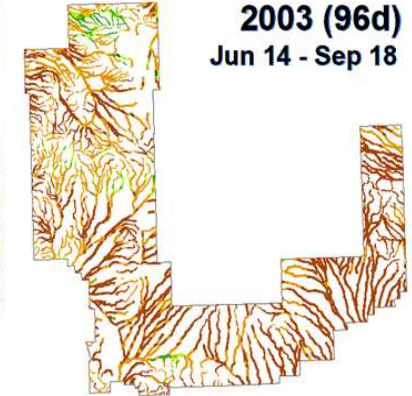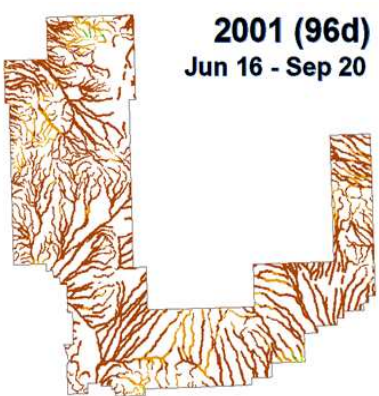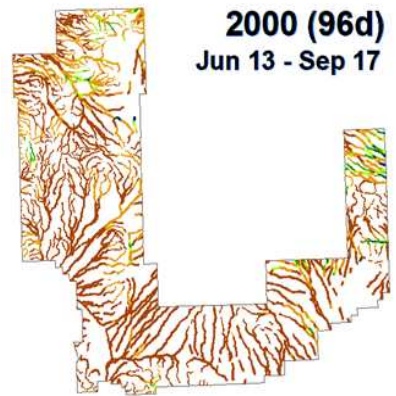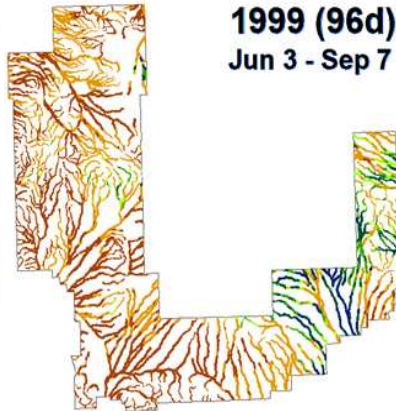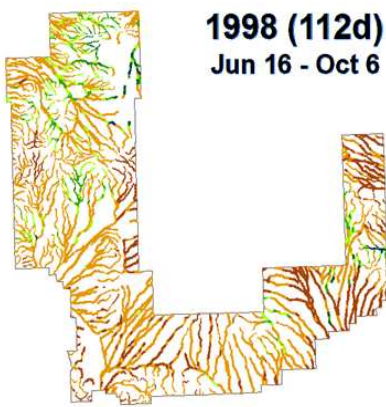| Year	ΔNDVI-S - 1	ΔNDVI-S - 2	N	CI-1	CI-2	Test Estimate
2004-05	Oct6Oct6	Oct22Oct6	2354	0.0355	0.0362	**0.0358 ***
2004-05	Oct22Oct6	Nov23Oct6	2354	0.0381	0.0394	**0.0387 ***
2004-05	Nov23Oct6	Dec9Oct6	2843	0.0265	0.0276	**0.0270 ***
2004-05	Dec9Oct6	Dec25Oct6	2843	0.0681	0.0694	**0.0688 ***
2004-05	Dec25Oct6	Feb27Oct6	2269	0.0570	0.0631	**0.0600 ***
2004-05	Feb27Oct6	Mar15Oct6	2269	-0.0269	-0.0250	**-0.0260 ***
2004-05	Mar15Oct6	Mar31Oct6	2843	-0.0708	-0.0688	**-0.0698 ***
2004-05	Mar31Oct6	Apr16Oct6	2843	-0.0502	-0.0482	**-0.0492 †† ***
2004-05	Apr16Oct6	May2Oct6	2843	-0.0171	-0.0167	**-0.0169 †† ***
2005-06	Oct9Oct9	Nov26Oct9	2843	0.0223	0.0229	**0.0226 ***
2005-06	Nov26Oct9	Jan13Oct9	2843	-0.0049	-0.0043	**-0.0046 ***
2005-06	Jan13Oct9	Jan29Oct9	2843	-0.0032	-0.0028	**-0.0030 ***
2005-06	Jan29Oct9	Apr3Oct9	1911	-0.0194	-0.0186	**-0.0190 ***
2005-06	Apr3Oct9	Apr19Oct9	1911	0.0105	0.0109	**0.0107 ***
2006-07	Sep26Sep26	Oct12Sep26	2843	0.0320	0.0324	**0.0322 ***
2006-07	Oct12Sep26	Oct28Sep26	2843	0.0085	0.0090	**0.0087 ***
2006-07	Oct28Sep26	Nov29Sep26	2843	0.0073	0.0079	**0.0076 ***
2006-07	Nov29Sep26	Dec31Sep26	2843	-0.0060	-0.0056	**-0.0058 ***
2006-07	Dec31Sep26	Jan16Sep26	2843	0.0028	0.0033	**0.0031 ***
2006-07	Jan16Sep26	Feb1Sep26	2843	-0.0116	-0.0112	**-0.0114 ***
2006-07	Feb1Sep26	Feb17Sep26	2843	-0.0053	-0.0049	**-0.0051 ***
2006-07	Feb17Sep26	Apr6Sep26	1477	-0.0060	-0.0054	**-0.0057 ***
2006-07	Apr6Sep26	May8Sep26	1477	-0.0002	0.0001	-0.0001
2007-08	Sep29Sep29	Jan19Sep29	2843	0.0402	0.0409	**0.0405 ***
2007-08	Jan19Sep29	Mar7Sep29	2823	0.0094	0.0104	**0.0099 ***
2007-08	Mar7Sep29	Mar23Sep29	2823	-0.0100	-0.0094	**-0.0097 ***
2007-08	Mar23Sep29	Apr8Sep29	2843	-0.0119	-0.0115	**-0.0117 ***
2007-08	Apr8Sep29	Apr24Sep29	2843	-0.0045	-0.0042	**-0.0043 ***
2008-09	Oct1Oct1	Oct17Oct1	2843	0.0277	0.0281	**0.0279 ***
2008-09	Oct17Oct1	Nov18Oct1	2843	0.0080	0.0084	**0.0082 ***
2008-09	Nov18Oct1	Jan5Oct1	2800	0.0320	0.0328	**0.0324 ***
2008-09	Jan5Oct1	Feb6Oct1	2707	0.0106	0.0117	**0.0112 ***
2008-09	Feb6Oct1	Mar10Oct1	2750	0.0082	0.0095	**0.0088 ***
2008-09	Mar10Oct1	Mar26Oct1	2843	-0.0332	-0.0321	**-0.0326 ***
2008-09	Mar26Oct1	May13Oct1	2843	-0.0226	-0.0218	**-0.0222 ***
2009-10	Oct20Oct20	Nov5Oct20	2843	0.0245	0.0249	**0.0247 ***
2009-10	Nov5Oct20	Nov21Oct20	2843	0.0055	0.0058	**0.0057 ***
2009-10	Nov21Oct20	Jan24Oct20	2843	0.0028	0.0033	**0.0030 ***

Year	ΔNDVI-S - 1	ΔNDVI-S - 2	N	CI-1	CI-2	Test Estimate
2009-10	Jan24Oct20	Feb25Oct20	2843	0.0415	0.0429	**0.0422 ***
2009-10	Feb25Oct20	Apr14Oct20	2843	-0.0016	0.0003	-0.0006
2009-10	Apr14Oct20	Apr30Oct20	2831	-0.0110	-0.0101	**-0.0106 ***
2010-11	Sep5Sep5	Oct7Sep5	2483	0.0301	0.0305	**0.0303 ***
2010-11	Oct7Sep5	Dec10Sep5	2483	-0.0074	-0.0067	**-0.0071 ***
2010-11	Dec10Sep5	Jan27Sep5	2843	0.0249	0.0260	**0.0255 ***
2010-11	Jan27Sep5	Feb12Sep5	2843	-0.0068	-0.0064	**-0.0066 ***
2010-11	Feb12Sep5	Feb28Sep5	2843	0.0035	0.0041	**0.0038 ***
2010-11	Feb28Sep5	Mar16Sep5	2843	-0.0119	-0.0114	**-0.0117 ***
2010-11	Mar16Sep5	Apr1Sep5	2843	-0.0018	-0.0013	**-0.0015 ***
2010-11	Apr1Sep5	Apr17Sep5	2843	-0.0084	-0.0080	**-0.0082 ***

1995 (96d)
Jun 8 - Sep 12

1996 (160d)
May 9 - Oct 16

1997 (96d)
Jul 15 - Oct 19

1998 (112d)
Jun 16 - Oct 6

1999 (96d)
Jun 3 - Sep 7

2000 (96d)
Jun 13 - Sep 17

2001 (96d)
Jun 16 - Sep 20

2002 (96d)
Jun 19 - Sep 23

2003 (96d)
Jun 14 - Sep 18

| | 0.0000 - 0.0002 | | 0.0005 - 0.0006 | | 0.0008 - 0.0012 |
| | 0.0003 - 0.0005 | | 0.0006 - 0.0008 | | 0.0012 - 0.0040 |

2004 (96d)
Jul 2 - Oct 6

2005 (112d)
Jun 19 - Oct 9

2006 (96d)
Jun 22 - Sep 26

2007 (96d)
Jun 25 - Sep 29

2008 (112d)
Jun 11 - Oct 1

2009 (112d)
Jun 30 - Oct 20

2010 (64d)
Jul 3 - Sep 5

2011 (80d)
Jun 20 - Sep 8

0.0000 - 0.0002	0.0005 - 0.0006	0.0008 - 0.0012
0.0003 - 0.0005	0.0006 - 0.0008	0.0012 - 0.0040
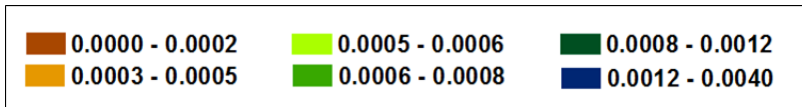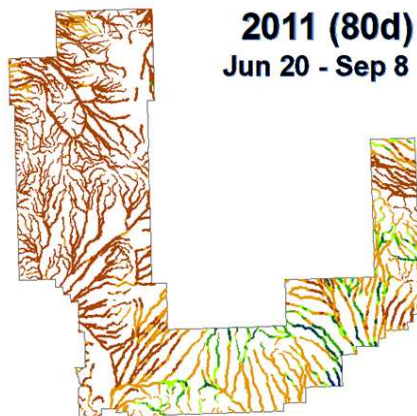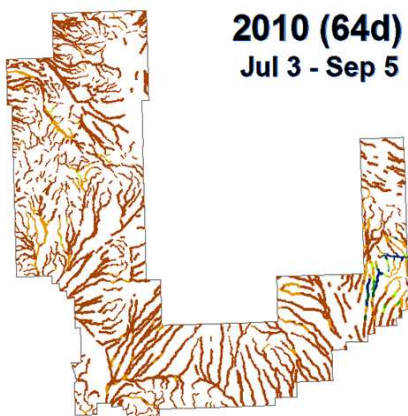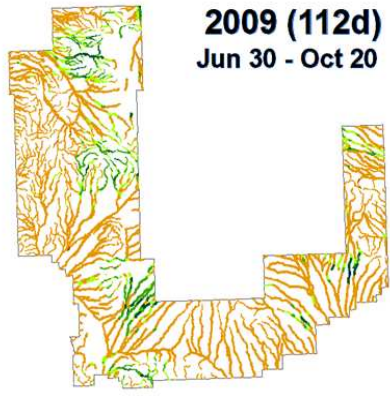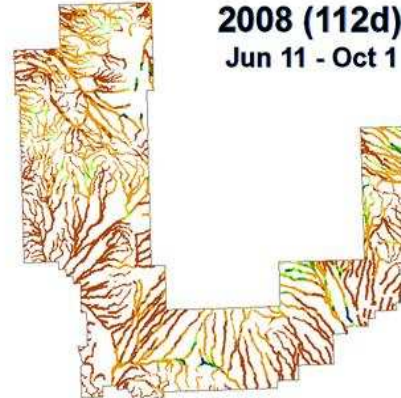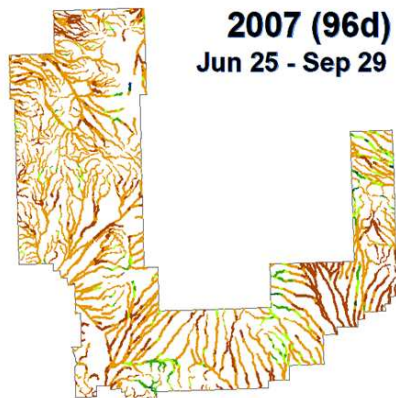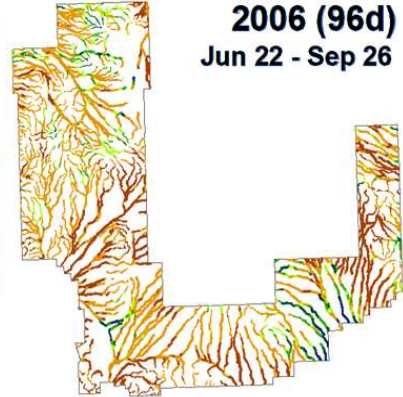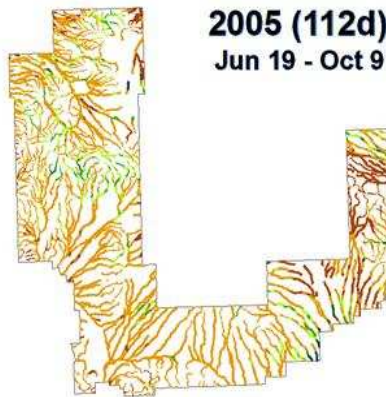
APPENDIX F: GEOMORPHIC METHODS TUTORIAL

TABLE OF CONTENTS

INTRODUCTION

Semi-arid and arid climates are globally abundant, experiencing a rise in human population and an increase in land degradation (Ravi et al., 2010). The majority of vegetation in these regions is restricted to riparian areas which are ephemeral in nature, only experiencing flow events during intense and infrequent rain events. Degradation of these riparian areas will undoubtedly have a negative impact on the biota and human populations within these regions. These ecosystems can also be challenging to study due to the high annual and interannual variability in precipitation, infrequent stream flow, lack of long term data, and the harshness and remoteness of the landscape (Hooke, 2007).   Furthermore, studying these regions with interdisciplinary approaches has shown to be beneficial to the overall understanding of the system (Newman et al., 2006).

Characteristics of geomorphology, hydrology, and land cover were calculated at varying scales as model parameters among four DoD installations: Fort Bliss (southern New Mexico), Fort Huachuca (SE Arizona), Yuma Proving Grounds (YPG, located on the Arizona-California border), and Fort Irwin (SE California). After the parameter processing was completed, the Salford Predictive Modeler Software[1] was used to analyze these data in a Random Forest Statistical Model. The goal of the modeling was to investigate which geo-hydro and vegetative attributes are valuable in describing ephemeral and intermittent streams in the Arid Southwest. All of the data used in creating these databases are freely available through various institutions and governmental organizations. It is important to note that as data improves these parameters and variables may be updated with similar methodology as described here. Since these ecosystems are complex this dataset is by no means complete and there are likely to be additional parameters or variables that would benefit this analysis. The addition of other parameters or different scales may improve model performance and may identify other important aspects in describing stream networks. This document describes the methods regarding the derivation and calculation of the suite of data that were created in this analysis.

---

[1] http://www.salford-systems.com/ (Salford Systems)

Hierarchical Hydrological Units

It has long been regarded that describing a system at multiple scales enhances understanding where multiple processes (biological, physical or chemical) simultaneously interact at varying spatial and temporal scales with each other. Often times the reasons behind the reach scale channel processes are often influenced by larger scale processes such as landcover type, soil characteristics, topography and disturbances within the uplands. The data that was created at varying spatial and temporal scales may lead to new insight on the processes that are occurring at the reach scale.

This methodology focuses on three hydrologic scales, but also takes into account larger spatial scales. The Water Boundary Dataset (WBD) within the NHDPlus Version 2 dataset maps Hydrologic Unit Codes (HUCs) at several hierarchical scales across the conterminous US. The HUC 8 (Subbasin) scale was used to isolate the smaller scale hydrologic units (HUC 10, HUC 12 and Catchment). In these databases, the HUC 12 (Watershed Hydrologic Unit) and Catchment (Valley Hydrologic Unit) scales were of primary focus and many of the parameters/variables used here were derived at these scales as well as the Reach scale. It is important to note that in certain regions the Catchment dataset is not nested within the HUC 12 layer and therefore may skew data analyses in these areas. The Catchment layer is at the heart of this problem and is most substantiated at Fort Bliss. While this should not have an adverse effect on the outcomes of this research, it is important to take into consideration when analyzing results or in decision making.

Data Acquisition

The stream networks and varying spatial scales were taken directly from the National Hydrography Dataset Plus[2] (High Resolution Dataset) and were downloaded by state (Table 1: *Flowline & HUC data[2]*). This includes the NHD Flowline network, and the hydrologic boundary feature classes: HUC 8, HUC 10 and HUC 12. The Catchment layer (*NHDPlusV21_XX_XX_NHDPlusCatchment_01.7z)* and Flow Accumulation Grid (*NHDPlusV21_XX_XX_XX_FdrFac_01.7z*) were downloaded by the HUC 2 Identifier (Table 1: *Drainage Area ID, VPU, and RPU*) through the Horizon Systems NHD Plus website[3].

Table 1: Downloading NHDPlus data from NHDftp[2] and Horizon Systems[3] website.

Base	Flowline & HUC data[2]	Catchment & Flow Accumulation Grid data[3]			
	NHD Plus High Resolution Dataset	**HUC 2 Name**	**Drainage Area ID**	**HUC 2 (VPU)**	**Raster Processing Unit (RPU)**
Fort Bliss	NHDH_NM_931v10.zip	Rio Grande	RG	13	13a, 13b, 13c
Fort Huachuca	NHDH_AZ_931v201.zip	Lower Colorado	CO	15	15a
YPG	NHDH_AZ_931v201.zip NHDH_CA_931v201.zip	Lower Colorado	CO	15	15b
Fort Irwin	NHDH_CA_931v201.zip	California	CA	18	18a

The NHDPlus (High Resolution Dataset) flowline network covers most streams in the US and identifies every stream apart of the network with a unique *ReachCode* identifier. When a stream intersects with another stream, the downstream section receives a new *ReachCode* identifier. In this research analysis, the streams were split into smaller segments and an underscore and number were added to the end of the *ReachCode* ID. This became our unique identifier in this study.

HUC 8, HUC 10, HUC 12, NHDPlus Flowline

1. Download and Unzip the NHDPlus (High Resolution Dataset), Catchment, and FAC grid data (the FAC grid data will be set aside for later use)

---

[2]ftp://nhdftp.usgs.gov/DataSets/Staged/States/FileGDB/HighResolution/ (US Geological Survey: National Hydrograph Dataset)

[3] http://www.horizon-systems.com/nhdplus/NHDPlusV2_home.php (Horizon Systems Corporation)

2. Open ARCMap 10.1 and locate the NHDH geodatabase (NHDH_*XX*.gdb)

Figure 1: NHDPlus High Resolution geodatabase.

3. Under the *WBD* subfolder in the geodatabase (Figure 1), import WBD_HU8, WBD_HU10 and WBD_HU12 into ARCMap 10.1 (the smaller the HUC number, the larger the spatial scale)

4. Upload a boundary of the region of interest

5. Overlay the Boundary Layer with the WBD_HU8 layer

6. Use the **Select Tool** [icon] to select the intersecting WBD_HU8 polygons with the Boundary of interest (Figure 2, Table 2)

7. Use the **Select Tool** to extract the HUC 8 polygons that are identified in Table 2 under *Analysis -> Extract -> Select*

8. Use the **Clip Tool** to clip the HUC 10 and HUC 12 layers to the boundary of the HUC 8 layer that was just created, under *Analysis -> Extract -> Clip*

   a. *Input Features:* HUC 10, HUC 12

   b. *Clip Features:* HUC 8 output from the *Select Tool*

9. Import the NHDFlowline under the *Hydrography* subfolder (Figure 1) and follow **Step 8**, but with the Flowline layer as the input layer

10. Change Projection of the reduced HUC 8, HUC 10, HUC 12 and NHDFlowline layers into the associated WGS 1984 UTM projection (refer to Table 2 for specific projection)

   a. To do this, use the **Project Tool** *(Data Management Tools -> Projections and Transformations -> Feature -> Project)*
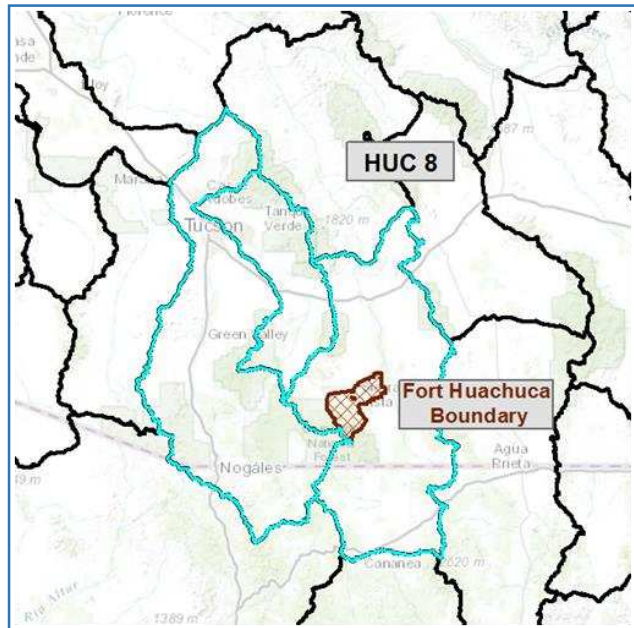
Figure 2: Selecting the HUC 8 layers that pertain to the study area.

Table 2: HUC 8 IDs that were selected in Step 6 and designated projection for each feature class in the end product.

Base	HUC 8 IDs Extracted in Step 6	Projected Coordinate System
Fort Bliss	13050003, 13030103, 13060010, 13050004, 13040100, 13030102	WGS_1984_UTM_Zone_13N
Fort Huachuca	15050302, 15050202, 15050301	WGS_1984_UTM_Zone_12N
YPG	15030106, 15030105, 15030104, 15070201, 15030107, 18100204, 15030108	WGS_1984_UTM_Zone_11N
Fort Irwin	18090204, 18090201, 18090207, 18090205, 18090206, 18090202, 18090208, 18090203	WGS_1984_UTM_Zone_11N

Catchment Layer

11. Upload the Catchment polygon layer in ARCMap 10.1 (Figure 3)

    a. The Catchment layer does not exactly match up to the HUC boundaries and therefore the Select Button was used to select the Catchment polygons that fall within the HUC 8 Boundary files (Figure 4)
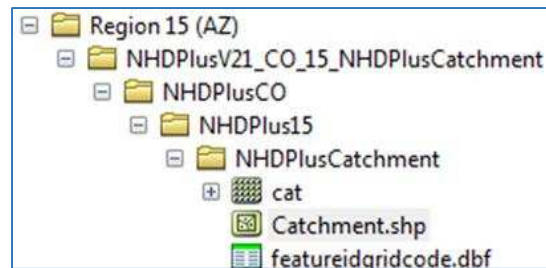
Figure 3: Location of Catchment Polygon after unzipped.

12. The **Select Tool** was used to extract the Catchment polygons *(Analysis -> Extract -> Select)*

13. The layer was re-projected as defined in Table 2 and **Step 10**
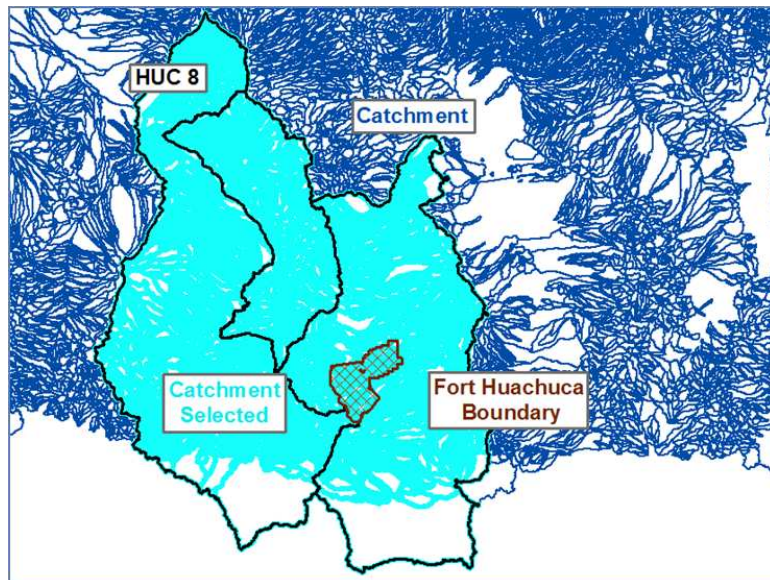
Figure 4: Selecting Catchment polygons.

Connecting Flowlines with each Watershed Boundary Polygon

The NHDPlus Flowline layer was intersected with each NHDPlus Watershed Boundary layer so future joins between these layers could be easily executed. The unique common identifiers in Table 3 were transferred to the NHDPlus Flowline layer by the Intersecting Tool.

Table 3: The Fields in the Attribute Table that holds the Unique Identifier in each WBD Layer.

WBD Layer	Common Identifier	WBD Layer	Common Identifier
HUC 8	HUC_8	HUC 12	HUC_12
HUC 10	HUC_10	Catchment	GRIDCODE

14. **Spatial Join Tool** was used on each WBD Layer with the NHDPlus Flowline layer *(Analysis Tools -> Overlay -> Spatial Join)*

    a. *Target Features:* NHDPlus Flowline
       Join Features: HUC 8
       Join Operation (optional): JOIN_ONE_TO_ONE
       Match Option (optional): HAVE_THEIR_CENTER_IN

    b. Repeat for HUC 10, and HUC 12 and Catchment

15. In the original NHDPlus Flowline layer 4 new Fields were added by the ***Add Field*** button under

    the menu tab   **(Figure 5)**

    a. *Name:* HUC8ID
       Type: Text
       Length: 8

    b. *Name:* HUC10ID
       Type: Text
       Length: 10

    c. *Name:* HUC12ID
       Type: Text
       Length: 12

    d. *Name:* GRIDCODE
       Type: Long
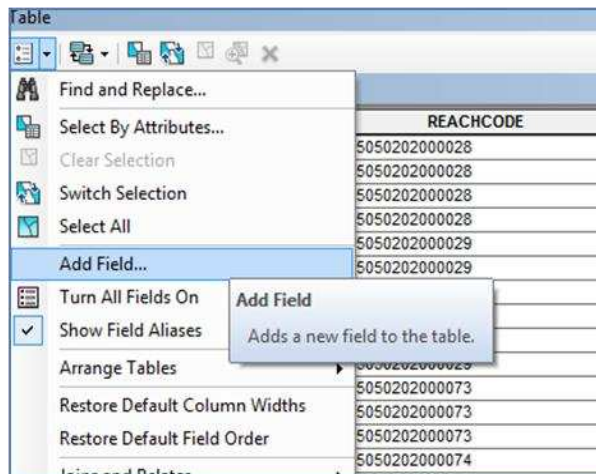
Figure 5: Adding Fields in the Attribute Table.

***The following Steps (16 to 18) were executed for each individual join before moving on to the next join; **Step 16** creates the join, **Step 17** transfers the data and **Step 18** removes the join.

16. Each WBD layer was joined separately to the NHDPlus Flowline Layer by

a. Right Clicking the NHDPlus Flowline layer in the *Table of Contents;* moving curser over **Joins and Relates**, clicking **Join…** (Figure 6)

b. In the *Join Data* GUI, join the Common ID of the associated field as seen in Table 3 to the same Common ID from the selected intersected layers created in **Step 14** (which is set in Item 2)
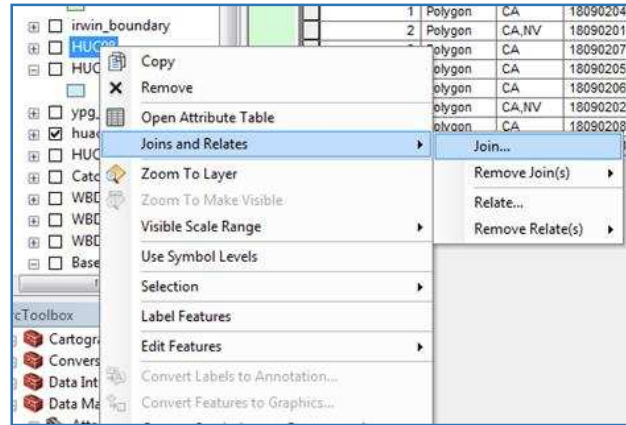
Figure 6: Joining two attribute tables in ArcGIS.

17. The **Field Calculator Tool** was used to transfer the Common ID from the intersected flowline layer to the main flowline layer by right clicking the column header and choosing *Field Calculator…*; *"XXX"* represents the name given to the output layers from **Step 14**; the formulas that transferred the Common IDs per WBD Layer are as follows:

a. *HUC8ID* = [**XXX:HUC_8**]

b. *HUC10ID* = [**XXX:HUC_10**]

c. *HUC12ID* = [**XXX:HUC_12**]

d. *GRIDCODE* = [**XXX:GRIDCODE**]

18. Each Join was removed

a. Right Click on Layer in Table of Contents; move mouse over *Joins and Relates,* then *Remove Join(s),* click on Join to remove (Figure 7)
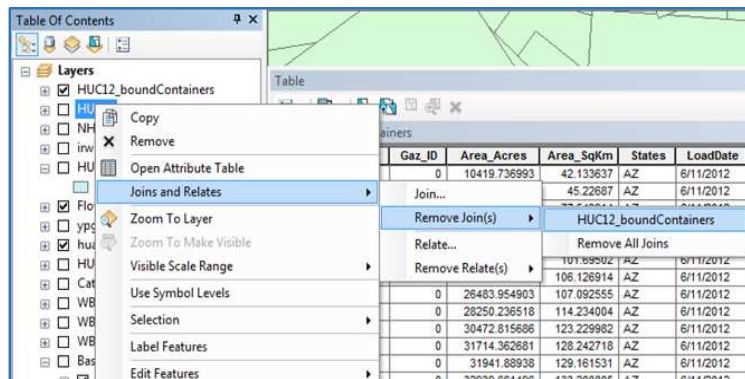
Figure 7: Removing Join by Right Clicking on Layer in the Table of Contents.

Reach Layer

19. The **Clip Tool** was used to create the Reach layer *(Analysis -> Extract -> Clip)*; (Figure 8)

    a. *Input Features:* The re-projected Flowline Layer created in **Steps 9 & 10**

    b. *Clip Features*: Boundary Layer (in the same Projection as the *Input Features*)

20. The ET Geo Wizards Tool was downloaded through ET Spatial Techniques[4] and uploaded into ARCMap 10.1 Toolbox. This tool was used to divide the reaches into equal lengths roughly around 1 km

21. The **Split Tolerance Tool** was used (Note: a Licensed is required)

    a. *Input:* Base Boundary
            Flowline Layer
        Segment Length: 1 km
        Split Tolerance: Equal Length

22. In the Attribute Table, two new fields were created (**Step 15**, Figure 5)

    a. *Name:* ET_ID
        Type: Text
        Length: 5

    b. *Name:* UniqueID
        Type: Text
        Length: 25

Figure 8: Clipping the NHDPlus Flowline to the base boundary.

23. The **Field Calculator Tool** was used to calculate the new columns (Right click on column header and choose *Field Calculator….*); the formulas are as follows:

    a. *ET_ID =* **[FID]**
    b. *UniqueID =* **[REACHCODE] & "_" & [ET_ID]**

**The *UniqueID* is the unique identifier that is used in the rest of this methodology to join and relate the Attribute Tables of the associated layers back to the reach scale and to link up the geodatabase tables of the end products to the spatial layers.

---

[4] http://www.ian-ko.com (ET SpatialTechniques)

After the HUCs, Catchment, NHDPlus Flowline, and Reach (at the Base scale) were all created, the next task was to estimate eco-geo-hydro attributes at each scale using a variety of GIS functions and data sources, as identified in Figure 7. The HUC 8 and HUC 10 layers are at larger scales and therefore only a few parameters have been calculated for them. The HUC 12 or Watershed Scale and Catchment layers incorporate data that are generalized to the extents of each polygon. The Reach scale is at the smallest scale and generalizes data along each 1km reach that were created in **Steps 14 – 18**.
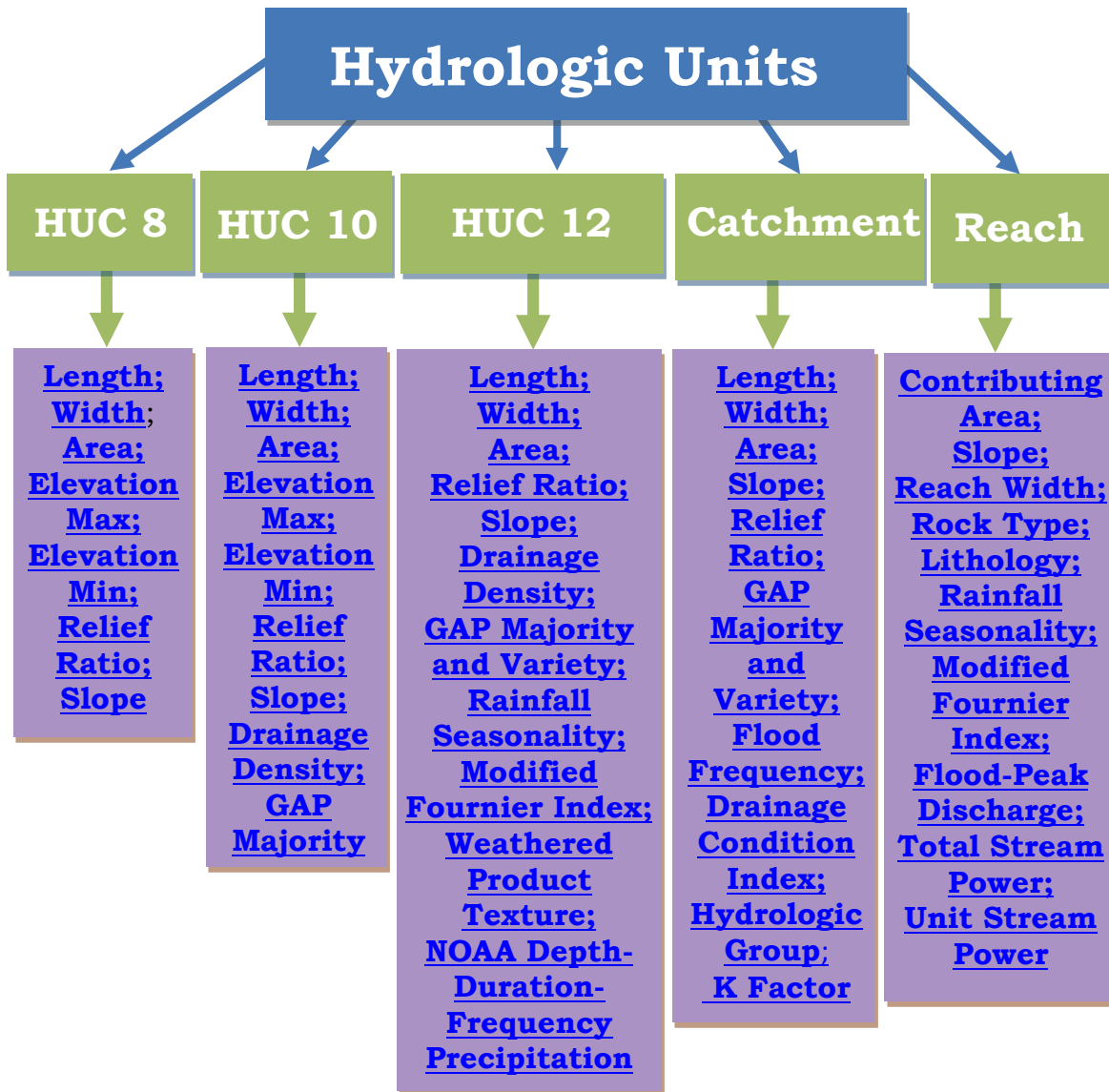
Figure 9: Spatial assignments of each parameter included within the geomorphic dataset. The items in this figure are linked to the area within this document that shows how the data was processed.

It is important to note that when some parameters were calculated, they were derived off of or have input variables from other parameters, therefore the order that the parameters proceed in is important in most cases.

HUC 8, HUC 10, HUC 12, and Catchment Metrics

Length, Width and Area

The dimensions of the polygon layers within the HUC 8, HUC 10, HUC 12 and Catchment layers were estimated to display detail concerning the hydrologic units at each scale. Length was used to calculate the average slope for each hydrologic unit within the spatial layers.

24. The **Minimum Bounding Geometry Tool** was used to calculate the Length and Width of each polygon within each feature class

      a. *Input:* HUC 8, HUC 10, HUC 12
          Geometry Type (optional): RECTANGLE_BY_AREA option
          Group Option (optional): None
          Check *Add geometry characteristics as attributes to output (optional)*

      b. The output feature class maintained each of the input attributes and added
          MBG_Width, MBG_Length, MBG_Orient

25. Two new fields were added in each NHDPlus Layer (**Step 15**, Figure 5)

      a. *Name:* Width_km
          Type: Float

      b. *Name:* Length_km
          Type: Float

26. The Main Layer was joined to the Minimum Bounding Geometry output shapefile using the Common Identifiers specified in Table 3 (**Step 16**, Figure 6)

27. The **Field Calculator** in the Attribute Table was used to transfer the data (refer to **Step 17**); note that the dimensions were in units of meters; dividing by 1000 in the **Field Calculator** puts the dimensions into km; "*XXX*" represents the name given to the output table from **Step 24**; the formulas used are as follows:

      a. *Width_km = [XXX:**MBG_Width] / 1000**

      b. *Length_km = [XXX:**MBG_Length] / 1000**

28. The Join was removed (**Step 18**, Figure 7)

29. Area was calculated for each Main Layer by adding another Field (**Step 15,** Figure 5)

      a. *Name:* Area_sqkm; *Type:* Float

30. The area was calculated by right clicking on the field that was just created then clicking **Calculate Geometry…** (Figure 10)

   a. *Property:* Area
      Units: Square Kilometers [sq km]
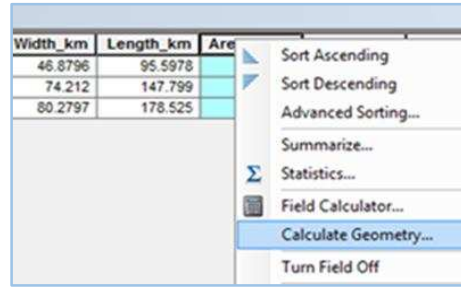
Figure 10: Calculate Geometry for a Field.

Elevation Max, Elevation Min, Relief Ratio and Slope

For these parameters, a Digital Elevation Model (DEM) was used. These raster datasets were downloaded through the USGS National Map Viewer website[5] for each region to the extent of the NHDPlus layers. The specific DEMs used in this analysis were from the National Elevation Dataset (NED) 1/3 and have a spatial resolution of 10m or 1/3 arc-second and are in an ArcGrid format with units in meters. The DEMs that pertained to each installation were merged for continuous coverage throughout the installation and to the extent of the NHDPlus layers. Each DEM was used to acquire the Elevation Max and Min parameters. The Relief Ratio is simply the range between the highest and lowest elevation values within each NHDPlus unit. The slope (m/m) was determined by dividing the Relief Ratio within the specific spatial unit by the length of that unit.

Table 4: Specific DEM Grid Code IDs (NED 1/3 arc-second) used in estimating Elevation and Slope parameters at the HUC extents. These grid layers were downloaded through the USGS: National Map Viewer[5].

Base	USGS NED 1/3 arc-second Grid ID			
Fort Bliss	n31 w105 n31 w106 n31 w107	n32 w105 n32 w106 n32 w107 n32 w108	n33 w105 n33 w106 n33 w107 n33 w108	n34 w106 n34 w107	n35 w106 n35 w107
Fort Huachuca	n32 w110 n32 w111 n32 w112	n33 w111 n33 w112			
YPG	n33 w114 n33 w115 n33 w116 n33 w117	n34 w113 n33 w114 n33 w115 n33 w116 n33 w117	n35 w114 n35 w115		
Fort Irwin	n35 w116 n35 w117 n35 w118 n35 w119	n36 w116 n36 w117 n36 w118 n36 w119	n37 w116 n37 w117 n37 w118 n37 w119	n38 w117 n38 w118 n38 w119	

---

[5] http://viewer.nationalmap.gov/viewer/ (US Geological Survey: The National Map Viewer)

31. The grids shown in Table 4 were downloaded through the USGS National Map Viewer website[5] and unzipped

32. All DEM grids per study area were uploaded into ARCMap 10.1

33. All DEM grids were transformed into the WGS 1984 UTM projection as specified by Table 2 and **Step 10**

34. The **Mosaic Tool** was used to mosaic all the datasets into one target dataset *(Data Management Tools -> Raster -> Raster Datasest ->Mosaic)*

    a. *Input Rasters:* For each base, all but 1 of the Grids mentioned in Table 4
       Target Raster: The remaining Grids not used in *Input Rasters*, per base

35. To link up the Elevation Data to each of the NHDPlus Boundary layers, the **Zonal Statistics as Table Tool** was used *(Spatial Analyst Tools -> Zonal -> Zonal Statistics as Table)*

    a. *Input raster or feature zone data:* HUC 8, HUC 10, HUC 12 or Catchment
       Zone field: ***The Common Identifier shown in Table 3 was used***
       Input value raster: Mosaiced DEM created in **Step 34**
       Statistics type (optional): MIN_MAX

36. Four new fields were added to each NHDPlus layer (**Step 15**, Figure 5)

    a. *Name:* ElevMax_m;   *Type:* Float
    b. *Name:* ElevMin_m;   *Type:* Float
    c. *Name:* Relief Rat;   *Type:* Float
    d. *Name:* Slope;   *Type:* Float

37. A join (**Step 16**, Figure 6) was used to join the Zonal Statistics as Table output table (**Step 35)** to each NHDPlus layer with the Common Identifier shown in Table 3

38. After joined, the **Field Calculator** was used to transfer the Min and Max elevation data to the main NHDPlus layers; Note, the DEM input data is in meters and therefore the Min Max data is also represented in meters; *"XXX"* represents the name given to the output table; the formulas used are as follows:

    a. *ElevMax_m =* **[*XXX***:MAX]**
    b. *ElevMin_m=* **[*XXX***:MIN]**

39. The Join was removed (See **Step 18**, Figure 7)

40. To calculate the Relief Ratio, the **Field Calculator Tool** was used (see **Step 17**); the formula used is

    a. *ReliefRat =* **[ElevMax_m] - [ElevMin_m]**

41. To calculate Slope, the **Field Calculator Tool** was used (see **Step 17**); Note, the units for Relief Ratio had to be changed to km; the slope is unitless; the formula used is

    a. *Slope =* **([ReliefRat] / 1000) / [Length_km]**

Drainage Density (HUC 10 and HUC 12 only)

Drainage Density (in units of km/km^2) is an important variable as it estimates the ability of a watershed to drain, where the larger drainage densities suggest higher peak floods, higher sediment yield, and steeper slopes (Dunne & Leopold, 1978; pg 500). Drainage Density is calculated by summing the length of all streams within a drainage area then dividing it by the area of the drainage area. While the NHDPlus Flowline layer is a coarse estimation of many of the streams in the southwest, this parameter can still be useful as it is consistent in recording the larger stream types. A finer Drainage Density would have included the smaller streams and braided channels that are not located on the NHDPlus Flowline. Nevertheless, this is important to note as the drainage density derived from the NHDPlus dataset are likely to be underrepresented values, which is why we see many values less than 1.0 km/km^2. A Drainage Density of 0 means there are no stream channels. In our dataset, this is most often seen at Fort Bliss in areas of little to no slope and high infiltration rates.

42. NHDPlus Flowline, HUC 10, and HUC 12 layers were opened in ARCMap 10.1

43. The **Intersect Tool** was used to join the Flowline layer with the HUC layers *(Analysis Tools -> Overlay -> Intersect)*

    a. *Input Features:* NHDPlus Flowline

    　　　　　　　　HUC 10
    Join Attributes (optional): ALL
    Output Type (optional): Input

44. **Step 43** was repeated for the HUC 12 layer

45. In the intersected Flowline layers, a new field was added (**Step 15,** Figure 5)

    a. *Name:* Length
    Type: Float

46. ***Calculate Geometry…*** was used on the field just created to calculate the length of all the reaches in km (**Step 30**, Figure 10)

    a. *Property:* Length
    Units: Kilometers [km]

47. All non-natural streams were removed, such as ditches, canals and pipelines

    a. In the Attribute Table **Select by Attributes…** was used; under the menu tab
    (Figure 11)
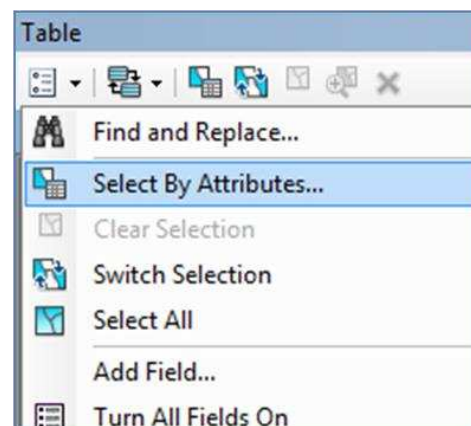
Figure 11: Select By Attributes…

93

b. This equation was inserted:

   "FTYPE" = 'StreamRiver'

48. Once all of the StreamRiver FTypes were selected the **Select Tool** was used, under *Analysis -> Extract -> Select*

49. The **Dissolve Tool** was used to dissolve the streams on the HUC 10 and HUC 12 Flowline; where the unique Common Identifier was used to dissolve the flowlines on (*Data Management Tools -> Generalization -> Dissolve*)

   a. *Input Features:* Output from **Step 48** (HUC10flowline or HUC12flowline layers)
      Dissolve: Check HUC_10 or HUC_12 depending upon input
      Statistics Field(s) (optional):
         Field: Length
         Statistics Type: SUM

50. The ***Sum_Length*** from the dissolved layer for the HUC 10 and HUC 12 layers were transferred to the main NHDPlus HUC 10 and HUC 12 layers by

   a. Adding a new Field (**Step 15**, Figure 5)

      i. *Name:* SumLen_km;   *Type:* Float

   b. Joining the tables (**Step 16**, Figure 6)

   c. Using Field Calculator (**Step 17**) with the formula:

      i. *SumLen_km =* **[*XXX*:Sum_Length]**

   d. Removing the Join (**Step 18**, Figure 7)

51. Drainage Density was now calculated

   a. A new field was added to the attribute table in the main NHDPlus HUC 10 and HUC 12 layers (**Step 15**, Figure 5)

      i. *Name:* DrainDen;   *Type:* Float

   b. Field Calculator (**Step 17**) was used with the formula:

      i. *DrainDen =* **[SumLen_km] / [Area_SqKm]**

GAP Majority and Variety (HUC 10, HUC 12 and CATCHMENT)

   National Gap Analysis Program (GAP)[6] data was taken from the Southwest and South Central Region. This raster dataset is delivered in the Albers Conical Equal Area Projection. The GAP data is derived from the Landsat 7 ETM+ satellite imagery from 1999 through 2001 and digital elevation model (DEM) datasets. Each $30m^2$ cell within the dataset has been assigned an Ecological System or a land use

---

[6] http://gapanalysis.usgs.gov/gaplandcover/ (US Geological Survey, 2011)

value and description. This classification was created through using a decision tree classifier (Gap Metadata[7]).

The GAP Majority variable estimates the majority of the landcover from the GAP model that occurs in each drainage unit within the HUC 10, HUC 12 and Catchment scales. The values created through this method should be considered categorical data and indicate a certain landcover type. The GAP Majority field of the NHDPlus layers can be joined to the GAP raster layer through the Value field to identify each landcover type. The GAP Variety estimates the diversity in landcover types within each drainage unit at each scale.

52. The SW and Southcentral GAP models were downloaded and uploaded into ARCMap

53. The Southwest and Southcentral GAP models were transferred into the designated projection as defined by Table 2 and using the **Project Raster Tool** *(Data Management Tools -> Projections and Transformations -> Project Raster)*

54. The Southwest GAP layers was then clipped to fit the NHDPlus extents by using **Extract by Masked Tool** *(Spatial Analyst Tools -> Extraction -> Extract by Mask)*

55. An extra step was required for Fort Bliss as portions of the study area were located in the Southcentral GAP region; **Step 54** was repeated using the Southcentral GAP layer

    a. After both GAP rasters were masked, they were merged together through the **Mosaic Tool** *(Data Management Tools -> Raster -> Raster Datasest ->Mosaic)*

        i. *Input Rasters:* Fort Bliss's re-projected and masked Southcentral GAP *Target Raster:* Fort Bliss's re-projected and masked Southwest GAP

56. To link up the GAP Data to each of the NHDPlus layers, the **Zonal Statistics as Table Tool** was used *(Spatial Analyst Tools -> Zonal -> Zonal Statistics as Table)*

    a. *Input raster or feature zone data:* HUC 10, HUC 12 or Catchment
       *Zone field: **Use Common Identifier shown in Table 3***
       Input value raster: The associated GAP layer created in **Step 54**; Bliss: **Step 55**
       Statistics type (optional): ALL

57. The *Majority* and *Variety* fields from the Tables created in **Step 56** for the HUC 10 & 12 and Catchment layers were transferred to the associated NHDPlus HUC 10, HUC 12, Catchment layers by

    a. Adding two new Fields (**Step 15**, Figure 5)

        i. *Name:* GAPmaj; *Type:* Long

        ii. *Name:* GAPvar; *Type:* Long

    b. Joining the NHDPlus layer to the appropriate Zonal Statistics Table (**Step 21**, Figure 8)

---

[7] http://gapanalysis.usgs.gov/gaplandcover/files/2012/09/USGS_GAP_LandCover_Metadata.pdf (Gap Analysis Program, 2010)

c.   Using Field Calculator (**Step 17**)

        i.   *GAPmaj = [XXX:**Majority**]*

        ii.   *GAPvar = [XXX:**Variety**]*

    d.   Removing the join (**Step 18**, Figure 7)

Rainfall Seasonality and Modified Fournier Index (HUC 12)

    Rainfall is an important driver in arid landscapes especially when rainfall events are temporally and spatially variable. Characterizing how precipitation events occur annually can be an important indicator of channel form, degree of erosibility and impact vegetation especially when rain events are concentrated. The Rainfall Seasonality Index (RS) takes the wettest month and divides it by the annual total precipitation and therefore attempts to describe the seasonal differences in rainfall dynamics (Equation 1). Taking the average of monthly rainfall over many years, the RS index will describe the climatic seasonality in a region.

    The RS index described above is closely related to the Fournier Index which squares the precipitation of the wettest month. An extension of the Fournier Index, known as the Modified Fournier Index (MFI) measures the effects of rainwater on erosion where higher values equate to more erosibility potential (Elagib, 2011). The MFI is classified into five categories: very low (0 – 60), low (60-90), moderate (90-120), high (120-160) and very high (>160) (Elagib, 2011). The Modified Fournier Index (MFI) takes the sum of the squares of the mean rainfall total per month for the annum then divides it by the mean annual precipitation amount (Equation 2). Several papers have described the MFI as a beneficial measure of rainfall erodibility potential using the above criteria (Elagib, 2011).

Equation 1:
$$RS = \frac{Mean\ Monthly\ Precip\ of\ Wettest\ Month}{Mean\ Annual\ Precip}$$

Equation 2:
$$MFI = \sum_{n=1}^{12} \left(\frac{(Month_n)^2}{Mean\ Annual\ Precip} \right)$$

    The mean monthly and mean annual precipitation data used in the RS and MFI equations were derived using the PRISM 30-Year Normals dataset[8]. The PRISM Data were downloaded through the Oregon State University as ASCII layers (13 layers in total) at a 800 meter resolution. These data were calculated using the HUC 12 and reach layer (**Steps 106-109**), calculating the RS and MFI at the watershed and reach scale. The precipitation is downloaded in units of mm*100, so all precipitation values should be divided by 100 to convert precipitation to mm.

---

[8] http://www.prism.oregonstate.edu/normals/ (PRISM Climate Group, 2010)

58. After the Annual and Monthly 30-Year Normals[8] (.asc) data at the 800m resolution were download and unzipped, the 13 ASCII layers were uploaded into ARCMap 10.1

59. The HUC 12 was transferred into the same projection as the PRISM datasets (GCS North American 1983) by using the **Project Tool** *(Data Management -> Projections and Transformations -> Feature -> Project)*

    a. *Input:* HUC 12
    Output Coordinate System: GCS_North_American_1983
    Output Transformation (optional): WGS_1984_(ITRF00)_To_NAD_1983

60. To achieve the precipitation means within each HUC 12 drainage area, the **Zonal Statistics as Table Tool** was used *(Spatial Analyst Tools ->Zonal -> Zonal Statistics as Table);* Batch tool expedited this step; these tables were saved as the first 3 letters: ann, jan, feb, mar, apr, may, jun, jul, aug, sep, oct, nov, dec

    a. *Input raster or feature zone data:* HUC 12
    Zone field: HUC_12
    Input value raster: **1 of the 13 ASCII files downloaded in Step 58**
    Statistics type (optional): MEAN

61. The MEAN precipitation values for each HUC 12 unit from the 13 tables created in **Step 60** were joined back to the HUC12 shapefile with the GCS coordinate system by

    a. Adding 13 new Fields (**Step 15**, Figure 5)

        i. *Name:* Ann; Jan; Feb; Mar; Apr; May; Jun; Jul; Aug; Sep; Oct; Nov; Dec
        Type: Float

    b. Joining each table separately (**Step 16**, Figure 6)

    c. Using Field Calculator (**Step 17**); (divide by 100 changes the precipitation into mm)

        i. *Ann =* **[ann:MEAN]/100**

        ii. *Jan =* **[jan:MEAN]/100**

        iii. Et cetera…

    d. Remove each join (**Step 18**, Figure 7)

62. The Attribute Table of the HUC 8 with each annual and monthly mean precipitation value was then extracted into a .dbf file (Select the menu button ▤▾ in the attribute table, then ***Export…*** and save as a **dBASE Table**)

63. The .dbf file was uploaded into Excel

    a. In the adjacent cell to the **Dec** column, the **=MAX()** function was used to pull out the Highest Precipitation Value for all months (the **Ann** column was not included in this formula)

    b. In the next column, the Rainfall Seasonality (RS) was calculated by dividing the Highest Precipitation Value by the Annual Precipitation Value

c.　In the next column, the Modified Fournier Index (MFI) was calculated by following the MFI formula described in *Equation 2*

64. The Excel document was saved, uploaded into ARCMap and the RS and MFI data were transferred to the main HUC 12 layer by

　　　a.　Adding 2 new Fields (**Step 15**, Figure 5)

　　　　　i.　*Name:* RainfallSeas
　　　　　　　Type: Float

　　　　　ii.　*Name:* ModFournier
　　　　　　　Type: Float

　　　b.　Joining the HUC 12 to the excel (dbf) table (**Step 16**, Figure 6)

　　　c.　Using Field Calculator (**Step 17**)

　　　　　i.　*RainfallSeas=* **[***XXX***:RS]**

　　　　　ii.　*ModFournier=* [*XXX*:**MFI**]

　　　d.　Removing the join (**Step 18**, Figure 7)

Weather Products Texture (HUC 12)

　　　The Weathered Products Texture (WPT) parameter is a measure of the geologic parent material and is used to explain the availability of sediment potential within the watershed. This parameter is based off of the USGS Mineral Resources Program: Geology Datasets, where the categories in the Rock Type 1 field were simplified into four categories: *Unconsolidated, Coarse, Fine* and *Unknown* (for rock type assignment refer to Appendix: A). These USGS GIS layers were compiled from State Geology maps and can be downloaded per state[9]. The digital geology ARC layers for California[10], Arizona[11], New Mexico[12] and Texas[13] were downloaded (ArcView shapefiles: *XX*geol_dd.zip). Background information about these layers and attributes tables can also be found at
http://pubs.usgs.gov/of/2005/1351/documents/CONUSDocumentation.pdf.

65. The GIS versions of the State Geology layers were downloaded, unzipped and the *XX*geol_dd_polygon.shp layer was uploaded into ARC GIS

66. An extra step was needed at Fort Bliss, where the Texas and New Mexico geology layers were merged together by using the **Merge Tool** *(Data Management -> General -> Merge)*

---

[9] For New Mexico and Texas: http://pubs.usgs.gov/of/2005/1351/ (Stoeser et al. 2007). For California and Arizona: http://pubs.usgs.gov/of/2005/1305/ (Lundington et al. 2007)
[10] California Geology Layers (http://pubs.usgs.gov/of/2005/1305/#CA): *CAgeol_dd.zip*
[11] Arizona Geology Layers (http://pubs.usgs.gov/of/2005/1305/#AZ): *AZgeol_dd.zip*
[12] New Mexico Geology Layers (http://pubs.usgs.gov/of/2005/1351/#NM): *NMgeol_dd.zip*
[13] Texas Geology Layers http://pubs.usgs.gov/of/2005/1351/#TX): *TXgeol_dd.zip*

67. The **Project tool** was used to convert the geology shapefile into the same projection as the HUC 12 layer as documented in Table 2 *(Data Management Tools -> Projections and Transformations -> Feature -> Project)*

68. The **Clip Tool** was used to clip the geology layer to the HUC extents *(Analysis Tool -> Extract -> Clip)*

69. The Geology polygons were then dissolved on the ROCKTYPE1 field using the **Dissolve Tool** *(Data Management ->Generalization -> Dissolve)*

    a. *Input Features:* Geology Layer
       Dissolve_Field(s) (optional): check ROCKTYPE1

70. A new field was added into the attribute table of the dissolved geology layer (**Step 15**, Figure 5)

    a. *Name:* WPT
       Type: Text; *Length:* 50

    b. The four categories were added to the new field: *Unconsolidated, Coarse, Fine* and *Unknown* to reflect Appendix: A by using the **Editor Tool** *(Right click on layer in Table of Contents-> Edit Features -> Start Editing)*

71. The **Dissolve Tool** was preformed again to aggregate the WPT classes *(Data Management -> Generalization -> Dissolve)*

    a. *Input Features:* Geology Layer
       Dissolve_Field(s) (optional): check WPT

72. The geology polygon layer that stores the WPT field was then converted into a raster using **Polygon to Raster Tool** *(Conversion Tools -> To Raster -> Polygon to Raster)*

    a. *Input Features: **geology layer created in Step 71***
       Value field: WPT
       Cell assignment type (optional): Cell_Center
       Priority field (optional): NONE
       Cellsize (optional): 0.0001

73. **Zonal Statistics as Table Tool** was used to find the majority of the WPT index from the geology raster *(Spatial Analyst Tools -> Zonal -> Zonal Statistics as Table)*

    a. *Input raster or feature zone data:* HUC 12
       Zone field: WPT
       *Input value raster: **geology raster from Step 72***
       Statistics type (optional): MAJORITY

74. Since the Zonal Statistics calculated the Value field, the WPT has to be associated to the Value field; this was done by

    a. Adding a new Field in the Zonal Statistics Geology Table (**Step 15**, Figure 5)

        i. *Name:* WPT
          Type: Text
          Length: 50

    b. Joining the *Majority* field in the Zonal Statistics Geology Table to the *Value* field in the geology raster (**Step 16**, Figure 6)

    c. Using Field Calculator (**Step 17**)

        i. *WPT =* **[***XXX***:WPT]**

    d. Removing Join (**Step 18**, Figure 7)

75. The *WPT* field from the Zonal Statistics Geology Table was transferred to the main HUC 12 layer by

    a. Adding a new Field in the HUC 12 layer (**Step 15**, Figure 5)

        i. *Name:* WPT
          Type: Text
          Length: 50

    b. Joining the HUC 12 layer to the Zonal Statistics Table (**Step 16**, Figure 6)

    c. Using Field Calculator (**Step 17**)

        i. *WPT =* **[***XXX***:WPT]**

    d. Removing Join (**Step 18**, Figure 7)

NOAA Depth-Duration-Frequency (HUC 12)

The Depth-Duration-Frequency (DDF) estimates the depth of rainfall during extreme precipitation events as a function of duration for a specified return period. The frequency and magnitude of these events can be a major driver of fluvial geomorphological processes such as channel formation and sediment movement. The DDF estimates were calculated for rainfall depths at duration and frequency intervals of 10yr-30min, 10yr-60min, 10yr-2hr, 25yr-30min, 25yr-60min and 25yr-2hr; where the 10yr recurrence intervals have an annual exceedance[14] probability of 0.10 or a 10% chance of this type of event occurring each and every year; whereas the 25yr recurrence intervals have a probability of occurring of 0.04 or 4% chance each and every year (Dunne & Leopold, 1978, p 52-53).

---

[14] *Annual exceedance* is a measure of a sample of all annual extreme rain events of a certain duration interval at a measuring station (Dunne & Leopold, 1978, p 52).

The Precipitation Frequency raster data used in this research were developed through the Hydrometeorological Design Studies Center within the Office of Hydrologic Development of National Oceanic and Atmospheric Administration's (NOAA) National Weather Service (NWS) and are divided into volumes based on geographic location (Office of Hydrologic Development, 2014)[15]. At each DDF interval, the Semiarid Southwest (NOAA Atlas 14 Volume 1) were downloaded in ASCII grid format and used on the associated installations. The resolution of this data is at 889 meters and is delivered in precipitation values of inches*1000 (to put precipitation in interval form). The precipitation was transferred into mm with three significant figures.

Since Fort Bliss includes areas in Texas, DDF values for Texas had to be sourced separately through the *USGS: Atlas of Depth-Duration Frequency of Precipitation Annual Maxima for Texas[16]* contour maps (Asquith & Roussel, 2004). Within this document contains the DDF contour maps at varying duration and time scales. The precipitation depths were taken at the same six Duration-Frequency scales as the NOAA DDF datasets and are documented in intervals at a tenth of an inch. This was approximated by geo-referencing the contour maps and using the Editor Tool in ARCMap to add in the values. The DDF values were transformed into millimeters and rounded to two significant figures.

76. The raster files from the **NOAA Atlas 14 Volume 1 (Semiarid Southwest): Precipitation frequency estimates: Annual Maximum Series** data were downloaded at each DDF interval and unzipped

    a. *Annual exceedance probability:* 1/10   (10 year)
        i. *Duration:* 30-minute, 60-minute and 2-hour

    b. *Annual exceedance probability:* 1/25   (25 year)
        i. *Duration:* 30-minute, 60-minute and 2-hour

77. After layers were brought into ARCMap 10.1, the **Define Projection Tool** was used to put the DDF grids into the same projection (GCS North American 1983) as the HUC 12 layer created in **Step 59** *(Data Management -> Projections and Transformations -> Define Projection)*

78. To achieve the DDF means for each of the six intervals within each HUC 12 drainage area, the **Zonal Statistics as Table Tool** was used *(Spatial Analyst Tools ->Zonal -> Zonal Statistics as Table);* Batch tool expedited this step; these tables were saved as *sw10y30m, sw10y60m, sw10y2hr, sw25y30m, sw25y60m,* and *sw25y2hr*, respectively

    a. *Input raster or feature zone data:* HUC 12 (with GCS North American 1983 projection)
    Zone field: HUC_12
    Input value raster: **1 of the 6 DDF grids**
    Statistics type (optional): MEAN

---

[15] NOAA Atlas 14 Precipitation Frequency Estimates in GIS Compatible Format: NOAA Atlas 14 Volume 1 – Semiarid Southwest (sw) (http://hdsc.nws.noaa.gov/hdsc/pfds/pfds_gis.html)

[16] USGS: Atlas of Depth-Duration Frequency of Precipitation Annual Maxima for Texas: http://pubs.usgs.gov/sir/2004/5041/ (Asquith & Roussel, 2004)

79. The MEAN precipitation values for each HUC 12 unit from the 6 tables created in **Step 78** were joined back to the *main* HUC12 shapefile

    a. Adding 6 new Fields (**Step 15**, Figure 5)

        i. *Name:* sw10y30m, sw10y60m, sw10y2hr, sw25y30m, sw25y60m, sw25y2hr
        Type: Float

    b. Join each table separately (**Step 16**, Figure 6)

    c. The following formulas were used in Field Calculator (**Step 17**) to convert the precipitation to mm and round it to the nearest tenth of a millimeter

        i. *sw10y30m* = **Round(([sw10y30m:MEAN]/1000*25.4), 1)**

        ii. *sw10y60m* = **Round(([sw10y60m:MEAN] /1000*25.4), 1)**

        iii. Et cetera…

    d. Each join was removed (**Step 18**, Figure 7)

80. Fort Bliss required an extra step where the *USGS: Atlas of Depth-Duration Frequency of Precipitation Annual Maxima for Texas* contour maps were used

    a. The DDF images were saved as a jpeg, then uploaded into ARCMap 10.1

    b. The images were georeferenced by adding at least 4 control points to each of the 6 DDF maps, (*Customize tab -> Toolbars -> Georeferencing*)

    c. **Editor Tool** was used on the HUC12 layer *(Right click on layer in Table of Contents-> Edit Features -> Start Editing)*

        i. The main HUC 12 layer was overlaid on each of the DDF contour map jpg

        ii. The average value for each DDF map was inputted into each HUC 12 polygon that overlaid with Texas in mm; Roughly in between the contour lines, DDF values were averaged; all values were rounded to 2 significant figures

Annual Flood Frequency, Drainage Condition Index, Hydrologic Group, K Factor (Catchment)

The Annual Flood Frequency, Drainage Condition Index, Hydrologic Group and K Factor variables are products of the STATSGO and SSURGO datasets that were acquired per region of interest through the NRCS Geospatial Data Gateway Portal[17]. The STATSGO GIS data is given on state scales, while the SSURGO data has a much finer resolution and is frequently mapped at the county level but is not continuous throughout the US.   Where the SSURGO dataset was absent, the STATSGO dataset was used.

---

[17] http://datagateway.nrcs.usda.gov/ or
    http://websoilsurvey.nrcs.usda.gov/app/WebSoilSurvey.aspx (Soil Survey Staff)

Annual Flood Frequency (see Supplement B) estimates the approximate number of times flooding occurs over a time period for a given area (USDA n.d., 618.30). There are a total of six Flood Frequency Classes, however majority of the areas observed in this study have very little flooding possibilities and fall into the *None* (< 1% chance of occurring within 100 yrs, but >1% occurring in 500yrs) flood frequency class, occasionally areas have slightly higher flood frequency potentials and are documented by the *Very Rare* (<1% chance of occurring within 100yrs) and *Rare* (1-5% chance of occurring within 100yrs) flood frequency classes. Fort Huachuca has a few regions that fall within the *Occasional* Flood Frequency Class where flooding has a 5-50% chance of occurring within 100 years (USDA n.d., 618.30). The flood frequency variable derived in this analysis is based off of the dominant Annual Flood Frequency class within each SSURGO/STATSGO mapunit.

The Drainage Condition Index consists of 7 classes that are based off of landscape position and soil morphology and refers to the natural drainage condition of the soil. The classes range from Excessively Drained to Very Poorly Drained (See Supplement B) which provides information regarding the limitations and potentials of soil (USDA n.d., 618.18). The drainage variable used in this analysis was based off of the dominant Drainage Condition within each SSURGO/STATSGO mapunit.

The Hydrologic Groups are split into four distinct categories (A, B, C, or D) that display similar runoff patterns (See Supplement B). These classes are based off of information pertaining to intake and transmission of water under the conditions of maximum yearly wetness, unfrozen soil, bare soil surface and maximum swelling of expansive clays; with the principle idea that soils found within a climatic region should be similar in the following factors: depth of a restrictive layer (includes water table), transmission rate of water, soil texture, structure and degree of swelling when saturated (USDA Natural Resources Conservation Services, 2007). To summarize, Group A soils generally allow water to flow freely through the soil, has a low runoff potential even when soil is thoroughly wet and generally has less than 10% clay and more than 90% of sand or gravel; Group B soils generally allow water to transmit through soil unimpeded, therefore having moderately low runoff potential even when thoroughly wet, and generally consist of 10-20% clay and 50-90% sand with some loamy sand or sandy loam textures; Group C soils have constrained water transmission rates causing a moderately high runoff potential when thoroughly wet, and are usually 20-40% clay and less than 50% sand with possibilities of loam, silt loam, sandy clay loam, clay loam, clay loam, and silty clay loam present; Group D soils have very poor water transmission rates through the soil causing high runoff potential when thoroughly wet, with greater than 40% clay, less than 50% sand and have clayey textures (USDA Natural Resources Conservation Services, 2007).

The KF factor is considered a soil erodibility factor that quantifies the ability of soil less than 2.0 mm (fine earth) to detach from the substrate via runoff and raindrop impact (USDA, n.d., 618.58). The KF factor is based off the interactions between five soil properties:

       1) Percent of silt plus very fine sand
       2) Percent of sand greater than 0.10mm
       3) Organic matter content
       4) Soil structure
       5) Saturated Hydraulic Conductivity

The KF factor is a categorical data made up of 14 classes; 0.02. 0.05, 0.10, 0.15, 0.17, 0.20, 0.24, 0.28, 0.32, 0.37, 0.43, 0.49, 0.55 and 0.64; where the spread of these classes represents the uncertainty associated with the K value, such that 0.10 has $\pm$ 0.025 units of uncertainty (USDA, n.d., 618.58).

Both the SSURGO and STATSGO spatial and tabulated data per region of interest were downloaded. The tabulated data was opened in the Microsoft Access SSURGO template supplied with the download through the NRCS Data Gateway website (http://datagateway.nrcs.usda.gov/). After the tabulated database was connected to Microsoft Access, it was then usable in ARCmap. The *muaggatt component* and *chorizon* files hold the relevant fields.

81. Download all relevant SSURGO and STATSGO data from the NRCS Data Gateway site

82. The soils data were unzipped as well as the soildb_US_2002 zip folder that is nested within

83. The Access database files were opened and the location of the tabulated folder was inputted into the SSURGO Import GUI (this enabled the soils databases to be useable in ARCMap

84. The spatial data of the STATSGO/SSURGO dataset as well as the corresponding *muaggatt, component,* and *chorizon* tables from the soildb_US_2002 access database were brought into ARCMap 10.1

85. Five new fields were added to the soils shapefile (**Step 15**, Figure 5)

    a. *Name:* HydroGrp
       Type: Text
       Length: 5

    b. *Name:* Drainage
       Type: Text
       Length: 50

    c. *Name:* FldFreq
       Type: Text
       Length: 25

    d. *Name:* cokey
       Type: Text
       Length: 30

    e. *Name:* KFfact
       Type: Text
       Length: 5

86. The *muaggatt* table was joined (**Step 16**, figure 6) through the mukey field to the soils shapefile; field calculator (**Step17**) was used to transfer the *hydgrpdcd* to the newly created HydrGrp field,

drclassdcd to the newly created Drainage field, and *flodfreqdcd* to the new FldFreq field; then the join was removed (**Step 18**, Figure 7)

87. Similarly to **Step 86**, the *component* table was joined to the soils shapefile through the *mukey* so that the cokey could be transferred to the newly created cokey field; then the join was removed

88. Similarly to **Step 86**, the *chorizon* table was joined to the soils shapefile through the *cokey* from the previous step, which allowed the *kffact* field to be transferred to the KFfact field in the soil shapefile; then the join was removed

89. **Steps 81** to **88** were repeated for each soils layer in the study areas; a **Merge Tool** *(Data Management -> General -> Merge)* was used to merge all of the SSURGO shapefiles together and where there was a lack of coverage from the SSURGO dataset, the STATSGO dataset was added (the **Erase** and **Merge Tool** was used to add in the non-overlapping dataset)

90. The final product of **Step 89** was re-projected in the comparable HUC extent projection (Table 2, **Step 10**) then clipped to the NHDPlus WBD extents (**Step 19**, Figure 8)

91. The merged soils shapefile was dissolved on each of the following fields: *HydroGrp, Drainage, FldFreq* and *KFfact fields* individually by using the **Dissolve Tool** *(Data Management Tools -> Generalization -> Dissolve)* to create four new shapefiles

    a. *Input Features:* Soils shapefile
    Dissolve Field: check one of the four fields mentioned above, individually

92. For each of the four dissolved layers created in **Step 91**, the **Select Tool** *(Analysis Tools -> Extract -> Select)* was used to remove the category with no data or in the case of the KF factor, the zeros; this was done by selecting all the non-empty categories (Figure 12)

FID	Shape *	Drainage
0	Polygon	
1	Polygon	Excessively drained
2	Polygon	Moderately well drained
3	Polygon	Poorly drained
4	Polygon	Somewhat excessively drained
5	Polygon	Somewhat poorly drained
6	Polygon	Well drained

Figure 12: Using Select Tool to remove out the empty data.

93. Each of the four dissolved shapefiles were transferred to a raster using the **Polygon to Raster Tool** *(Conversion -> To Raster -> Polygon to Raster)*

    a. *Input Features:* one of the four dissolved shapefile from **Step 92**
    Value field: the corresponding dissolved field (HydroGrp, Drainage, FldFreq or KFfact)

    CellSize: 20

94. To link up each of the soils data to each of the Catchment layers, the **Zonal Statistics as Table Tool** was used *(Spatial Analyst Tools -> Zonal -> Zonal Statistics as Table)*

    a. *Input raster or feature zone data:* Catchment
       Zone field: GRIDCODE
       *Input value raster: **Each Raster layer created in Step 92, individually***
       Statistics type (optional): MAJORITY

95. The output tables from **Step 94** had to have the categorical data transfer back into them

    a. Each table had a new field added (**Step 15**, Figure 5)
       i. *Name:* maj
          Type: Text
          Length: 50

    b. Each table was joined (**Step 16**, Figure 6) to the corresponding raster grid using the *MAJORITY* field from the Table and the *VALUE* field from the raster

    c. Field calculator was used to transfer the categories from the raster to the *maj* field for each table (**Step 17**)

    d. Each join was removed (**Step 18**, Figure 7)

96. The same fields in **Step 85** were added to the Catchment Layer

97. Each table was joined individually (**Step 16**, figure 6) to the Catchment layer through the GRIDCODE field; field calculator (**Step 17**) was used to transfer the *maj* to the corresponding newly created fields in the Catchment layer; then the joins were removed (**Step 18**, Figure 7)

Reach Metrics

Rock Type and Lithology

    The Rock Type and Lithology can be important metrics in indentifying the type and character of the substrate and can also suggests distinctive weathering patterns. Within the USGS Mineral Resources Program: Geology Datasets, these metrics portray the dominant Rock or Lithology types and are displayed in a hierarchal order ranging from ROCKTYPE1 to ROCKTYPE2 and LITH 1 to 5, where ROCKTYPE1 and LITH1 document the most dominant type. The USGS does note that the Geology Map Units are mapped on a relatively large scale (by state) and may force certain groupings to generalize the data at these scales and therefore may cause a generalization of the lithology categories; consequently, it is common that many of the Map Units contain more than one lithology (Lundington et al., 2007 & Stoeser, et al., 2007). Here LITH1 and LITH2 are assigned to each reach to help display the multiple lithologies.

Previously, ROCKTYPE1 was consolidated into the Weathers Texture Products in **Steps 65 - 75**. The same *XXgeol_dd_polygon* layers that were downloaded for the WPT metric from the USGS Mineral Resources Program: Geology Datasets were also used here. On the same website, the dbf file for each geology dataset was downloaded[18]. This dbf zipfile contains the lithology information that was linked to the geology shapefile through the UNIT_LINK field in both tables.

98. The same shapefile that was downloaded (for Fort Bliss, Texas and New Mexico were merged) and re-projected in **Steps 65 – 68** was uploaded into ARCMap 10.1

99. Three new fields were added to the geology shapefile at each base (**Step 15**, Figure 5)

    a. *Name:* LITH1
       Type: Text
       Length: 50
    b. *Name:* LITH2
       Type: Text
       Length: 50
    c. *Name:* LITH_FORM
       Type: Text
       Length: 50

100. The [State] .dbf file that was downloaded from the same USGS website (see footnote 18) as the geology shapefile was unzipped and the *XX*LITH.dbf file was uploaded into ARCMap 10.1

101. A join was created between the shapefile and the *XX*LITH.dbf file through the UNIT_LINK field (**Step 16**, Figure 6)

102. The LITH1, LITH2 and LITH_FORM fields were transferred to the geology shapefile through Field Calculator (**Step 17**) and the join was removed (**Step 18**, Figure 7)

103. A point shapefile was created that contained the midpoints of each reach by

    a. Creating an x and y field (float) within the reach layer

    b. Using calculate geometry tool (**Step 30**, Figure 10) to acquire the x and y coordinates of the midpoints of each reach

    c. Exporting the attribute table as a dbf file (Select the menu button   attribute table, then ***Export…*** and save as a **dBASE Table**)

---

[18] California Geology Layers (http://pubs.usgs.gov/of/2005/1305/#CA): *California dbf files;*
Arizona Geology Layers (http://pubs.usgs.gov/of/2005/1305/#AZ): *Arizona dbf files;*
New Mexico Geology Layers (http://pubs.usgs.gov/of/2005/1351/#NM): *New Mexico dbf files;*
Texas Geology Layers http://pubs.usgs.gov/of/2005/1351/#TX): *Texas dbf files*

d. In ARC Catalog, the mouse was moved over the exported file; right clicked; then ***Create Feature Class*** and ***From XY Table…*** was selected (Figure 13); in the next GUI, the x and y fields were selected accordingly.
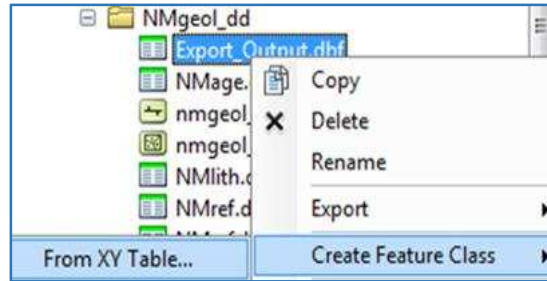
Figure 13: Creating a Feature Class from a dbf file.

    i. The new point layer was projected into the same projection as the geology layer

104. The point layer was intersected with the geology layer *(Analysis Tools -> Overlay -> Intersect)*

105. The ROCKTYPE1, ROCKTYPE2, LITH1, LITH2 and LITHFORM of the intersected point layer was transferred back to the main reach Flowline layer by

    a. Adding the fields (**Step 15**, Figure 5) to the Reach Flowline layer

        i. *Name:* ROCKTYPE1
        Type: Text
        Length: 50

        ii. *Name:* ROCKTYPE2
        Type: Text
        Length: 50

        iii. *Name:* LITH1
        Type: Text
        Length: 50

        iv. *Name:* LITH2
        Type: Text
        Length: 50

        v. *Name:* LITH_FORM
        Type: Text
       Length: 50

    b. Joining the tables through the *UniqueID* (**Step 16**, Figure 6)

    c. Using Field Calculator to transfer each of the 5 geology metrics to the reach network (**Step 17**)

    d. Removing the join (**Step 18**, Figure 7)

Rainfall Seasonality and Modified Fournier Index

The monthly PRISM grid layers were used to determine the Rainfall Seasonality (RS) and the Modified Fournier Index (MFI) of each reach. Calculating this metric at the reach scale may show more subtle changes within the differences in the average precipitation than as generalized at the Watershed (HUC 12) scale. Similar methods were utilized as described in the *Rainfall Seasonality and Modified Fournier Index* of the HUC 12 layer (**Steps 58 – 64)**; however, here the tool *Extract Multi Values to Points* was employed with the reach midpoint shapefile.

106. The Annual and Monthly 30-Tear Normals[19] (.asc) data at the 800m resolution that were download in **Step 58**, were uploaded into ARCMap 10.1 (13 ASCII layers)

107. The midpoint shapefile that was created in **Step 103** was transferred into the same projection as the PRISM datasets (GCS North American 1983) by using the **Project Tool** *(Data Management -> Projections and Transformations -> Feature -> Project)*

    a. *Input:* Reach Midpoint Layer
       Output Coordinate System: GCS_North_American_1983
       Output Transformation (otional): WGS_1984_(ITRF00)_To_NAD_1983

108. **Extract Multi Values to Points Tool** was used to add the monthly and annual precipitation values as each point *(Spatial Analyst Tools -> Extraction -> Extract Multi Values to Points)*

    a. *Input point features:* Reach Midpoint Layer in GCS projection
       Input rasters: Annual and All months (together), named appropriately

109. The same methods were followed as described in **Steps 61 -64**; except the attribute table of the layer that was created in **Step 108** was used instead of the HUC 12 layer

---

[19] http://www.prism.oregonstate.edu/normals/ (PRISM Climate Group, 2010)

Reach Width at 0.25, 0.5, 1, 2 and 3 meters

The widths of streams at varying depths (Figure 14) can be an important indicator of channel hydro-geomorphology and may be able to measure hydrologic influences such as bankfull width or channel incision. In this study, the mean widths at the various inundation depths were calculated at each reach segment. The HGVC (Hydro-Geomorphic Valley Classification) extension tool (Carlson E.A., 2009) was used in ARCmap 10.1 to calculate the width at different assigned inundated depths. To create these layers, a DEM (LiDAR or 10m DEM) and flowline shapefile were used with the *Optional Inundation Depth Tool*. The widths were calculated for 0.25, 0.5, 1.0, 2.0 and 3.0m.
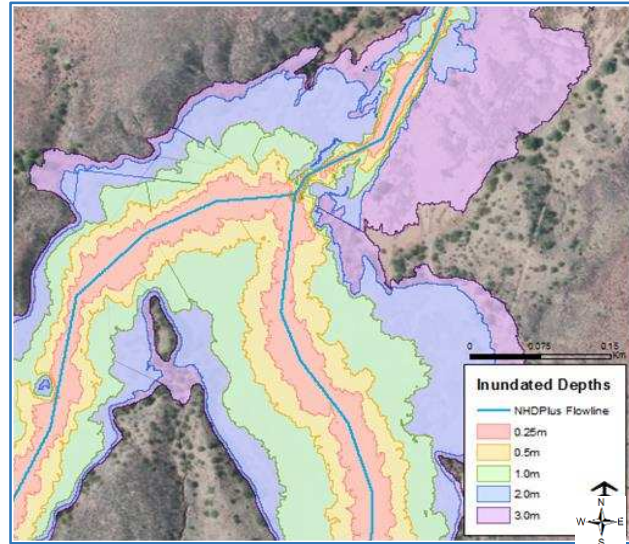
Figure 14: Inundated polygons at different depths at Fort Huachuca using the HGVC tool and LiDAR as the Digital Elevation Model.

110. The Reach Flowline Layer and DEM were uploaded into ARCMap 10.1

111. The LiDAR or DEM were re-projected into the associated spatial reference listed in Table 2

112. The HGVC 9.3 Toolset was added into ARCToolbox (by right clicking in ARCToolbox, selecting *Add Toolbox…* and navigating to location on computer), then the **Optional: Inundation Tool** was opened (*HGVC 9.3 Toolset -> Valley Segment Creation -> Optional: Inundation Depth*)

   a. *INPUT: Filled Surface Raster:* LiDAR or DEM (filled or unfilled)
      INPUT: Stream Network Raster: Reach Flowline Layer
      INPUT: Unique Valley Analysis Area Shapefile: Base Boundary
      Flood Depth (m) (optional): 3, 2, 1, 0.5, 0.25 (individually)

      i. NOTE: a filled surface raster will generally produce larger polygons in areas where pools exist; this may be more prominent in other regions where water is less ephemeral

113. A 200 m buffer of the flowline was created to segment the inundated layers back into the reach segments *(Analysis Tools -> Proximity -> Buffer)*

   a. *Input Features:* Reach Flowline
      Distance [value or field]: 200 meters
      Side Type (optional): FULL
      End Type (optional): FLAT
      Dissolve Fields (optional): NONE

114. The Inundation Layer was clipped to the Reach Buffer Layer *(Analysis Tools -> Extract -> Clip)*

    a. *Input Features:* Buffered Reach Layer (**Step 113**)
       Clip Features: 3m Inundation Layer (**Step 112**)

115. The output layer from **Step 114** was manually edited to remove extraneous portions of the stream segments that were clipped near adjacent streams or confluences

    a. The Intersect tool was useful here to find areas of overlap within the inundated reach polygon layer *(Analysis Tools ->Overlay -> Intersect)*; Input Features: the inundation reach layer by itself

116. Once the 3m inundation layer was completely edited, the 2m Inundation Layer was clipped *(Analysis Tools -> Extract -> Clip)*

    a. *Input Features:* Edited 3m Inundation Layer (**Step 115**)
       Clip Features: 2m Inundation Layer (**Step 112**)

    b. **Step 115** was re-executed for the 2m Inundation Reach output

117. **Step 116** was repeated for the 1, 0.5, and 0.25m using the corresponding Input and Clip features for each inundation depth

118. Two new Fields were added into each of the finalized inundation layers (**Step 15**, Figure 5)

    a. *Name:* Area_sqm; *Type:* Float
    b. *Name:* Width_m; *Type:* Float

119. For the *Area_sqm* field, Calculate Geometry was used to determine the area of each reach polygon (**Step 30**, Figure 10)

    a. *Property:* Area
       Units: Square Meters [sqm]

120. For the *Width_m* field in each Inundated Reach Layer, Field Calculator (**Step 17**) was used

    a. *Width_m=* **[Area_sqm] / [Length_m]**

121. In the main Reach Flowline Layer, five new fields were added (**Step 15**, Figure 5)

    a. *Name:* Width3m, Width2m, Width1m, Width0_5m, and Width0_25m
       Type: Float

122. The inundated widths were transferred to the main Reach Flowline Layer by

    a. Joining each Inundated Table through the *UniqueID* (**Step 16**, Figure 6)

    b. Using Field Calculator (**Step 17**) to transfer the *Width_m* field to the associated field created in **Step 121**

    c. Each Join was removed (**Step 18**, Figure 7)

National Flood Frequency: Linear Regression Equations

The relevant documents that display the Linear Regression Equations were downloaded through the USGS Publications Warehouse. The documents used for Fort Bliss were The *Analysis of the Magnitude and Frequency of Peak Discharge and Maximum Observed Peak Discharge in New Mexico and Surrounding areas[20]* and *The National Flood-Frequency Program – Methods for Estimating Flood Magnitude and Frequency for Natural Basins in Texas, 2001[21]*. For Fort Irwin, the document used was *Methods for Determining Magnitude and Frequency of Floods in California, Based on Data through Water Year 2006[22]*. For YPG and Huachuca, the document *The National Flood-Frequency Program – Methods for Estimating Flood Magnitude and Frequency in Rural Areas in Arizona[23]* was used*.*

Contributing Area

The Contributing Area (CA) of a channel is defined as the area of the hillslopes above the channel that can carry water during rain events into the channel. In a substantial rain event, the precipitation that falls across the CA of a channel can drastically increase the discharge within the portion of the channel. Therefore, larger CAs are likely to exhibit larger flows during a substantial rain storm. However, it is important to note that many of the ephemeral streams in the arid southwest tend to be influenced by high rates of infiltration especially in the flat, sandy areas. Some of the stream channels that have larger CA may actually experience less frequent and lower discharge quantities than channels with less CA, especially as the stream moves away from the mountainous and often shallow bedrock regions.

The CA used in this methodology was derived from the FAC grid layers supplied by the NHDPlus Version 2 Dataset which counts the number of cells within the HydroDEM that drains into each cell based (Figure 15). Each cell in the FAC grid is 30 by 30 meters and therefore has an area of 900m^2 or 0.0009km^2.   The CA values are used in the Flood Peak Discharge, Total Stream Power and Unit Stream Power Equations in the following sections.

123. The Flow Accumulation (FAC) Grid layers that were downloaded through the Horizon Systems NHD Plus website[24] in the Data Acquisition section were unzipped and uploaded into ARCMap 10.1 (Refer to Table 1: XXX_*FdrFac_01.7z.)*; at some bases, multiple grids were needed

---

[20] http://pubs.usgs.gov/sir/2008/5119/   (Waltemeyer, 2008)
[21] http://pubs.er.usgs.gov/publication/fs02201 (Sumioka, 2001)
[22] http://pubs.usgs.gov/sir/2012/5113/   (Gotvald, 2012)
[23] http://pubs.er.usgs.gov/publication/fs11198   (Mason, et al. 1999)
[24] http://www.horizon-systems.com/nhdplus/NHDPlusV2_home.php (Horizon Systems Corporation)
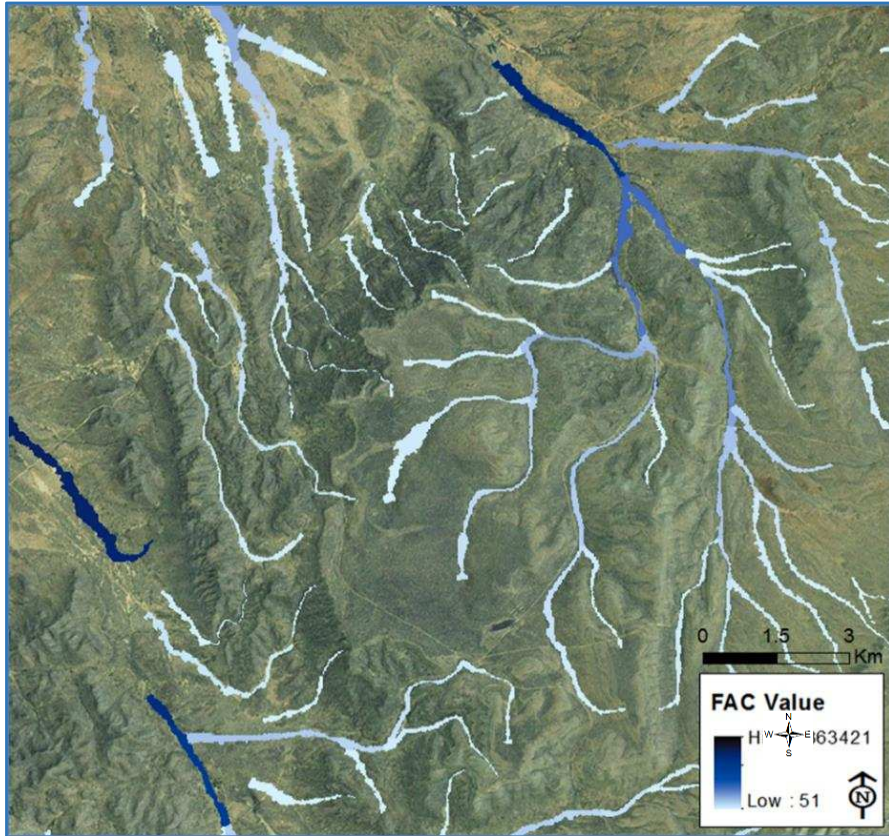
Figure 15: Flow accumulation values from the NHDPlus Version 2 dataset for each Reaches at Fort Bliss. The FAC values are were multiplied 0.0009 to get the contributing area (km^2).

124. The 1m Inundation Layer that was created in **Steps 110 – 117** was used to find the max FAC value of each reach

    a. The confluences of the 1m reach polygons were removed to eliminate processing errors

        i. **Intersect** the 1m Inundation Layer on itself *(Analysis Tools ->Overlay -> Intersect)*

        ii. **Erase** the intersected area *(Analysis Tools ->Overlay -> Erase)*

            1. *Input Features:* 1m Inundation Layer
               Erase Features: Intersected layer from **Step 124.a.i**

            2. This step inevitably erases some polygons to the extent that they do not pick up the correct FAC value, but this was mitigated in a later step

125. The newly created inundation layer was re projected into the same projection as the FAC grid layers *(Data Management Tools -> Projections and Transformations -> Feature -> Project)*

    a. *Output Coordinate System:* NAD_1983_To_WGS_1984_1
      Geographic Transformation (optional): NAD_1983_To_WGS_1984_1

126. **Zonal Statistics as Table** was used to find the max FAC value within the reach polygons *(Spatial Analyst Tools -> Zonal -> Zonal Statistics as Table)*

   a. *Input raster or feature zone data:* 1m Inunadated layer from **Step 125**
   Zone field: UniqueID
   Input value raster: FAC Grid
   Statistics type (optional): MAX

   b. This was completed for all overlapping grids in the study area

127. The values were transferred back to the original 1m Inundation Layer by

   a. Adding a new field to the Inundation Layer (**Step 15**, Figure 5)

      i. *Name:* fac
      Type: Long

   b. The tables were joined (**Step 16**, Figure 6) by the *UniqueID* field

   c. Field calculator was used to transfer the *max* field to the *fac* field (**Step 17**)

   d. The join was removed (**Step 18**, Figure 7)

128. Errors were corrected by using the *Symbology* Tab (Right click on the feature class, then select *Properties…*), selecting the *Graduated Colors* under the *Quantities* tab, then choosing the *fac* field as the Value class; this assisted the detection of incorrect or missing FAC values along the flowline network; any errors found were manually inserted into the *fac* field using the **Editor Tool**

129. After the FAC values were corrected, the attribute table was exported to a .dbf file and uploaded into excel

130. The fac values of each reach were converted into square miles to be used in the Discharge Linear Regression Equations by using the equation:

   Contributing Area (mi^2) = *fac value* * $0.009km^2$ * $0.386102mi^2/km^2$

Flood-Peak Discharge

   The Linear Regression equations found in the corresponding state Magnitude and Frequency documents that are described in the **National Flood Frequency Program** introduction were applied to calculate the Flood-peak Discharge for the recurrence intervals 2, 5, 10, 25, 50, and 100 years and were displayed in cms. It is important to note that the equations are delivered in US Customary units – cfs – and we reported the Flood-Peak Discharge in SI units – cms. Therefore, the Contributing Area for each reach is inputted into the equation in mi^2 and the equation then delivers Q in cfs. If elevation was needed, the elevation at the midpoint (in feet) of the reach was used. After the magnitude of discharge was calculated, the volume was then transformed back into cms (by multiplying by 0.028316).

131. In Excel, the Contributing Area for each reach that was calculated in **Step 130** was inserted into the Regional Discharge Equations associated with each installation at the 2, 5, 10, 25, 50, and 100 year recurrence interval (**Table 5)**

132. The Discharge values were converted into cms by multiplying the results by $0.028316 m^3/ft^3$

Table 5: Regional Discharge Equations where A stands for Contributing Area and Q_x is the Discharge at a specific recurrence interval.

Recurrence Interval	Fort Bliss	Fort Huachuca & YPG	Fort Irwin
Q_2	$= 146.5 \times A^{0.454}$	$= 10(6.38 - 4.29A^{-0.06})$	$= 10.3 \times A^{0.506}$
Q_5	$= 277.7 \times A^{0.468}$	$= 10(5.78 - 3.31A^{-0.08})$	$= 60.0 \times A^{0.506}$
Q_{10}	$= 387.8 \times A^{0.477}$	$= 10(5.68 - 3.02A^{-0.09})$	$= 151 \times A^{0.506}$
Q_{25}	$= 553.7 \times A^{0.488}$	$= 10(5.64 - 2.78A^{-0.10})$	$= 403 \times A^{0.506}$
Q_{50}	$= 695.5 \times A^{0.497}$	$= 10(5.57 - 2.59A^{-0.11})$	$= 760 \times A^{0.506}$
Q_{100}	$= 851.8 \times A^{0.506}$	$= 10(5.52 - 2.42A^{-0.12})$	$= 1,350 \times A^{0.506}$

Total Stream Power

The Total Stream Power (TSP) is an estimate of the ability for a stream to transport sediment and can be influential within fluvial systems. The equation for TSP in kW/m is

$$\Omega = \rho g Q S$$

Where ρ is the density of water at 1.0 kg/m³, g (gravity) = 9.81m/s², Q = Flood-Peak Discharge for the given frequency event (m³/s), S is slope (m/m). This calculation was completed for the same time intervals as the Flood-Peak Discharge by using the corresponding Q variable (2, 5, 10, 25, 50, and 100 years) that was calculated in the Flood-Peak Discharge section.

133. In Excel, the Discharge values (cms) per each recurrence interval were inserted into Equation 3, where Ω = kW/m

Equation 3: $\qquad \Omega = 1.0\,^{kg}/_{m^3} \times 9.81\,^{m}/_{s^2} \times Q\,^{m^3}/_{s} \times Slope\,^{m}/_{m}$

Unit Stream Power

The Unit Stream Power (USP) is an estimate of the rate of energy expenditure per unit area of channel bed and has relevance in bed sediment entrainment, bedload transport rate and stream stability. The equation used for USP in kW/m² is

$$\omega = \frac{\rho g S \sqrt{Q}}{a}$$

Where ρ, g, S and Q are the same variables in the Total Stream Power equation and *a* is a constant between 3.0 and 4.7 depending on the substrate. In this case, *a = 3.6* $\sqrt{s/m}$ was used. Again, this equation was used to calculate the corresponding Q variables in the Flood-Peak Discharge section.

134. In Excel, the Discharge values (cms) per each recurrence interval were inserted into Equation 4, where ω =kW/m²:

Equation 4: $\quad \omega = 1.0\ ^{kg}/_{m^3} \times 9.81\ ^{m}/_{s^2} \times Slope\ ^{m}/_{m} \times \dfrac{\sqrt{Q\ ^{m^3}/_{s}}}{3.6\sqrt{^{s}/_{m}}}$

135. The Discharge, Total Stream Power and Unit Stream Power were made into a geodatabase table with the associated *UniqueID,* which can be joined to the reach Flowline layer to map these quantities across each base

REFERENCES

Asquith W. H. and M. C. Roussel, 2004. Atlas of Depth-Duration Frequency of Precipitation Annual Maxima for Texas. U.S. Geological Survey Scientific Investigations Report 2004-5041. TxDOT Implementation Report 5-1301-01-1.

Bonnin, G. M., D Martin, B. Lin, T. Parzybok, M. Yekta, D. Riley. 2011. NOAA Atlas 14 Volume 1 Version 5.0, Precipitation-Frequency Atlas of the United States. Semiarid Southwest (Arizona, Southeast California, Nevada, New Mexico, Utah). NOAA, National Weather Service, Silver Spring, MD.

Dunne, T., and L.B, Leopold. 1978. Water in Environmental Planning, 2nd edn. W.H. Freeman, San Francisco.

Elagib, N. A. 2011. Changing Rainfall, Seasonality and Erosivity in the Hyper-Arid Zone of Sudan. *Land Degradation & Development* **22(6)**:505-512.

ET SpatialTechniques: ET GeoWizards, Version 10.2. Faerie Glen, South Africa.

Gap Analysis Program: Metadata. 2010. National Land Cover Gap Analysis Project. Version 1.

Gotvald, A.J., Barth, N.A., Veilleux, A.G., and Parrett, Charles. 2012. Methods for determining magnitude and frequency of floods in California, based on data through water year 2006: U.S. Geological Survey Scientific Investigations Report 2012–5113, 38 p., 1 pl., available online only at http://pubs.usgs.gov/sir/2012/5113/.

Hooke, J. M. 2007. Monitoring morphological and vegetation changes and flow events in dryland river channels. *Environmental Monitoring and Assessment* **127(1-3)**:445-457.

Horizon Systems Corporation: National Hydrography Dataset Plus (NHDPlus Version 2). Herndon, Virgina.

Carlson, E.A. 2009. Fluvial riparian classification for national forests in the western United States. M.S. Thesis. Colorado State University.

Lundington, S., B. Moring, R. J. Miller, P. A. Stone, A. A. Bookstrom, D. R. Bedford, J. G. Evans, G. A. Haxel, C. J. Nutt, K. S. Flyn, M. J. Hopkins. 2007. Preliminary Integrated Geologic Map Databases for the United States, Western States: California, Nevada, Arizona, Washington, Oregon, Idaho and Utah. Version 1.3. U. S. Geological Survey: Open-File Report (2005-1305). (http://pubs.usgs.gov/of/2005/1305/).

Mason, R. R. Jr., J. N. King, O. Jr. Wilbert. 1999. The National Flood-Frequency Program—Methods for Estimating Flood Magnitude and Frequency in Rural Areas in Arizona. U.S. Geological Survey Fact Sheet 111-98.

National Hydrography Dataset Plus - NHDPlus Version 2. U.S. Environmental Protection Agency (USEPA) and the U.S. Geological Survey (USGS).

Newman, B. D., B. P. Wilcox, S. R. Archer, D. D. Breshears, C. N. Dahm, C. J. Duffy, N. G. McDowell, F. M. Phillips, B. R. Scanlon, and E. R.Vivoni. 2006. Ecohydrology of water-limited environments: A scientific vision. *Water Resources Research* **42(6)**.

Office of Hydrologic Development, NWS, NOAA. April, 2014. Hydrometeorological Design Studies Center Quarterly Progress Report. Silver Spring, Maryland. (http://www.nws.noaa.gov/oh/hdsc/current-projects/progress/201404_HDSC_PR.pdf)

Perica S., S. Dietz, S. Heim, L. Hiner, K. Maitaria, D. Martin, S. Pavlovic, I. Roy, C. Trypaluk, D. Unruh, F. Yan, M. Yekta, T. Zhao, G. Bonnin, D. Brewer, L. Chen, T. Parzybok, and J. Yarchoan. 2011. NOAA Atlas 14 Volume 6 Version 2.0, Precipitation-Frequency Atlas of the United States, California. NOAA, National Weather Service, Silver Spring, MD.

PRISM Climate Group. 2010. Gridded climate data for the contiguous USA. http://prism.oregonstate.edu

Ravi, S., D. D. Breshears, T.E. Huxman, and P. D'Odorico. 2010. Land degradation in drylands: Interactions among hydrologic–aeolian erosion and vegetation dynamics. *Geomorphology* **116(3)**: 236-245.

Salford Systems: Salford Predictive Modeler (SPM). San Diego, California.

Soil Survey Staff, Natural Resources Conservation Service, United States Department of Agriculture. U.S. General Soil Map (STATSGO2).

Soil Survey Staff, Natural Resources Conservation Service, United States Department of Agriculture. Soil Survey Geographic (SSURGO).

Stoeser, D. B., G. N. Green, L. C. Morath, W. D. Heran, A. B. Wilson, D. W. Moore, and B. S. Van Gosen. 2007. Preliminary Integrated Geologic Map Databases for the United States, Central States: Montana, Wyoming, Colorado, New Mexico, North Dakota, South Dakota, Nebraska, Kansas, Oklahoma, Texas, Iowa, Missouri, Arkansas, and Louisiana. Version 1.2. U. S. Geological Survey: Open-File Report (2005-1351). (http://pubs.usgs.gov/of/2005/1351/).

Sumioka, S. S., K. G. Reis III. 2001. The National Flood-Frequency Program – Methods for Estimating Flood Magnitude and Frequency for Natural Basins in Texas, 2001. USGS Fact Sheet: 022-01.

USDA 2007. Natural Resources Conservation Services. Part 630 Hydrology National Engineering Handbook. Chapter 7: Hydrologic Soil Groups. Accessed: June 16, 2014. (http://directives.sc.egov.usda.gov/OpenNonWebContent.aspx?content=17757.wba)

USDA n.d. Natural Resources Conservation Services. National Soil Survey Handbook (NSSH): Part 618 (Subpart A). Accessed: June 16 2014. (http://www.nrcs.usda.gov/wps/portal/nrcs/detail/soils/survey/?cid=nrcs142p2_054223#39)

US Geological Survey. n.d. Gap Analysis Program (GAP). August 2011. National Land Cover, Version 2.

US Geological Survey. n.d. (b). National Hydrography Dataset: High Resolution.

US Geological Survey. n.d. (c). The National Map Viewer.

Waltemeyer, S.D. 2008. Analysis of the magnitude and frequency of peak discharge and maximum observed peak discharge in New Mexico and surrounding areas: U.S. Geological Survey Scientific Investigations Report 2008–5119, page 105.

Rock Type reclassified into the Weathered Products Texture parameter. Note: if a Rock Type is not included in this table then it can be classified as an "Unknown"

Rock Type	WPT	Rock Type	WPT
Alkaline Basalt	Fine	Granite	Coarse
Alluvial Fan	Unconsolidated	Granodiorite	Coarse
Alluvium	Unconsolidated	Gravel	Unconsolidated
Andesite	Fine	Intermediate Volcanic Rock	Fine
Argillite	Fine	Lake or Marine Deposit (Non-Glacial)	Unconsolidated
Basalt	Fine	Lava Flow	Fine
Carbonate	Fine	Limestone	Fine
Clastic	Coarse	Metasedimentary Rock	Fine
Clay or Mud	Unconsolidated	Mica Schist	Fine
Conglomerate	Coarse	Mudstone	Fine
Coarse Grained Mixed Clastic	Coarse	Plutonic Rock (phaneritic)	Coarse
Dacite	Fine	Quartz Monzonite	Coarse
Dolostone (dolomite)	Fine	Quartz-Feldspar Schist	Fine
Dune Sand	Unconsolidated	Rhyolite	Fine
Eolian	Unconsolidated	Sand	Unconsolidated

Felsic Volcanic Rock	Coarse	**Sandstone**	Coarse
Fine-Grained Mixed Clastic	Fine	**Schist**	Fine
Gabbro	Coarse	**Sedimentary Rock**	Fine
Gneiss	Coarse	**Shale**	Fine

	Flood Frequency	**Drainage Condition Index**	**Hydrologic Group**	**K Factor**
Description	The annual probability of a flood event	The natural drainage condition of the soil refers to the degree, frequency and duration of wet periods.	A group of soils having similar runoff potential under similar storm and cover conditions.	An erodibility factor which quantifies the susceptibility of soil particles to detachment by runoff and raindrop impact.
Data Type	Categorical	Categorical	Categorical	Categorical
Classes	6	7	4	14
Variables	**1 = None** (possibility of flood occurring <1 time in 500 yrs) **2 = Very Rare** (possibility of flood occurring <1 time in 100yrs) **3 = Rare** (possibility of flood occurring 1-5 times in 100yrs) **4 = Occasional** (possibility of flood occurring 5-50 times in 100yrs) **5 = Frequent** (possibility of flood occurring is >50 times in 100yrs, but less than 50% chance of flood occurring in all mon/yr) **6 = Very Frequent** (possibility of flood occurring is >50 times in 100yrs, but more than 50% chance of flood occurring in all mon/yr)	**1 = Excessive** **2 = Somewhat Excessive** **3 = Well Drained** **4 = Moderately Drained** **5 = Somewhat Poorly Drained** **6 = Poorly Drained** **7 = Very Poorly Drained**	**A** = low runoff potential **B** = moderately low runoff potential **C** = moderate runoff potential **D, A/D, B/D, C/D** = high runoff potential	0.02 0.05 0.10 0.15 0.17 0.20 0.24 0.28 0.32 0.37 0.43 0.49 0.55 0.64
Table Name	muaggatt	muaggatt	muaggatt	chorizon
Field Name	flodfreqdcd	drclassdcd	hydgrpdcd	kffact
NHHS Source (USDA n.d.)	618.30 Flodding Frequency Class	618.18 Drainage Class	618.39 Hydrologic Group	618.58 Soil Erodibility Factors
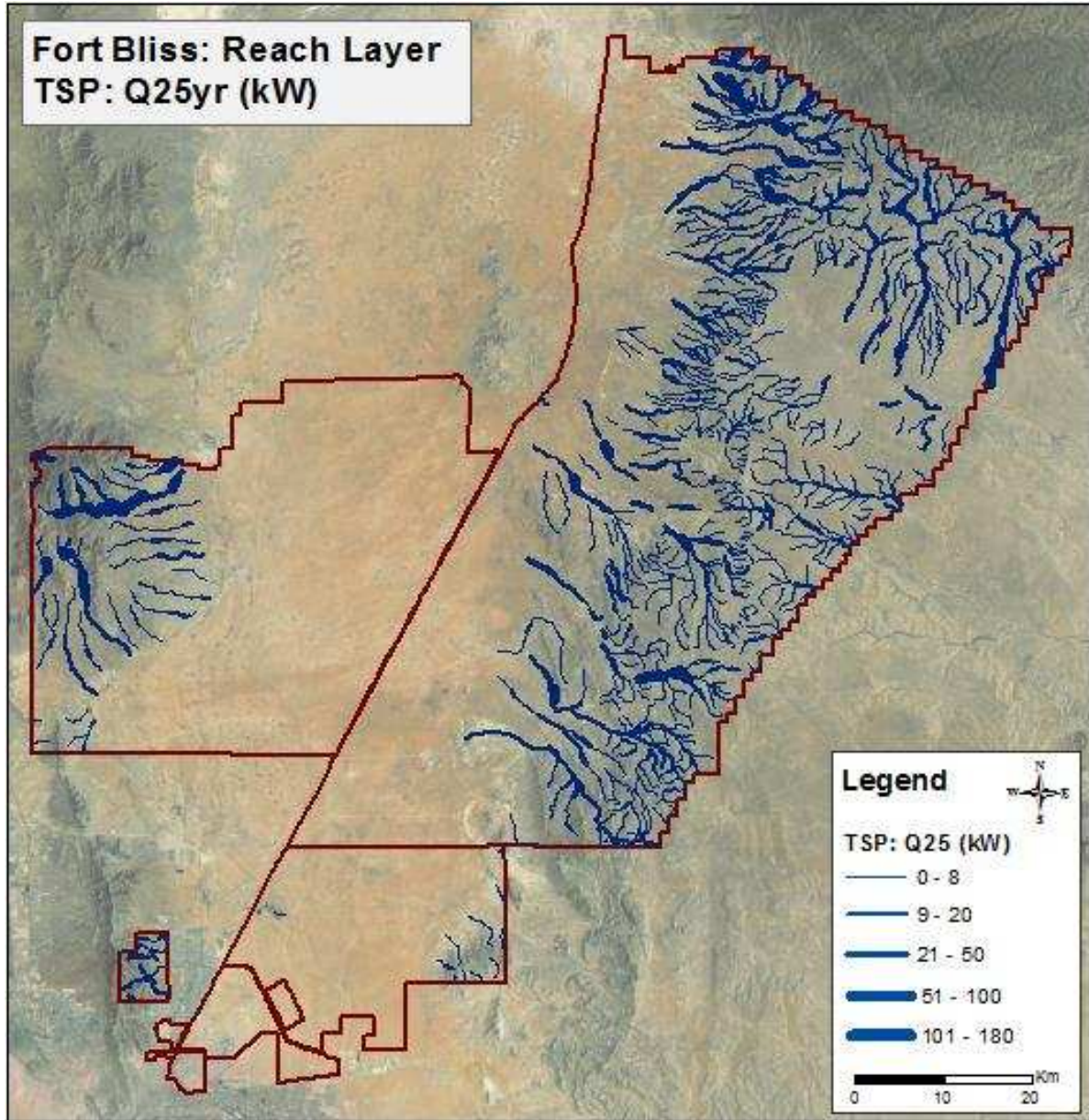
Fort Bliss: Catchment Layer KF Factor

Fort Bliss: HUC 12 Layer
Modified Fournier Index

Legend

Modified Fournier Index

- 25 - 33
- 34 - 39
- 40 - 45
- 46 - 54
- 55 - 66
- 67 - 85
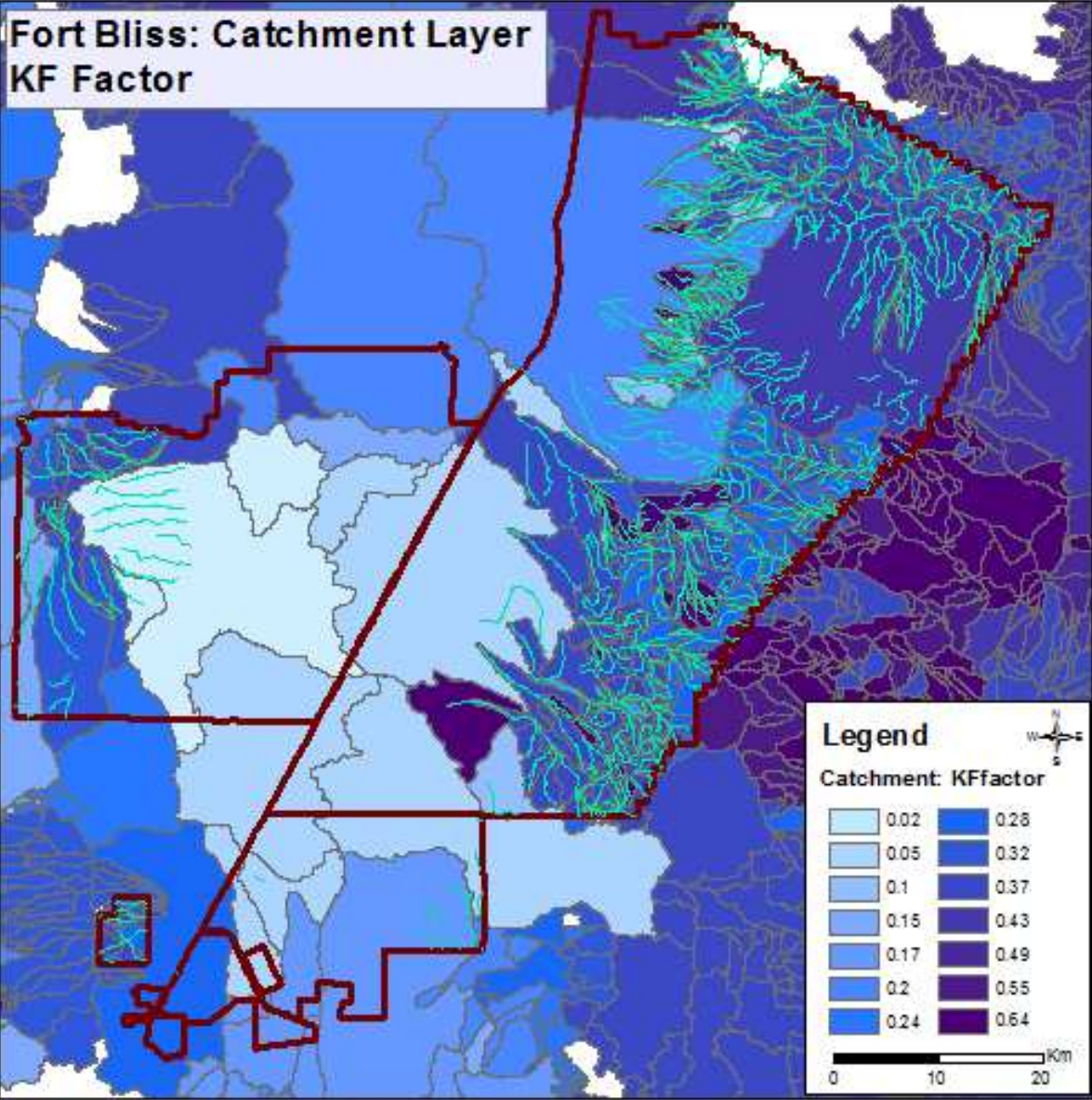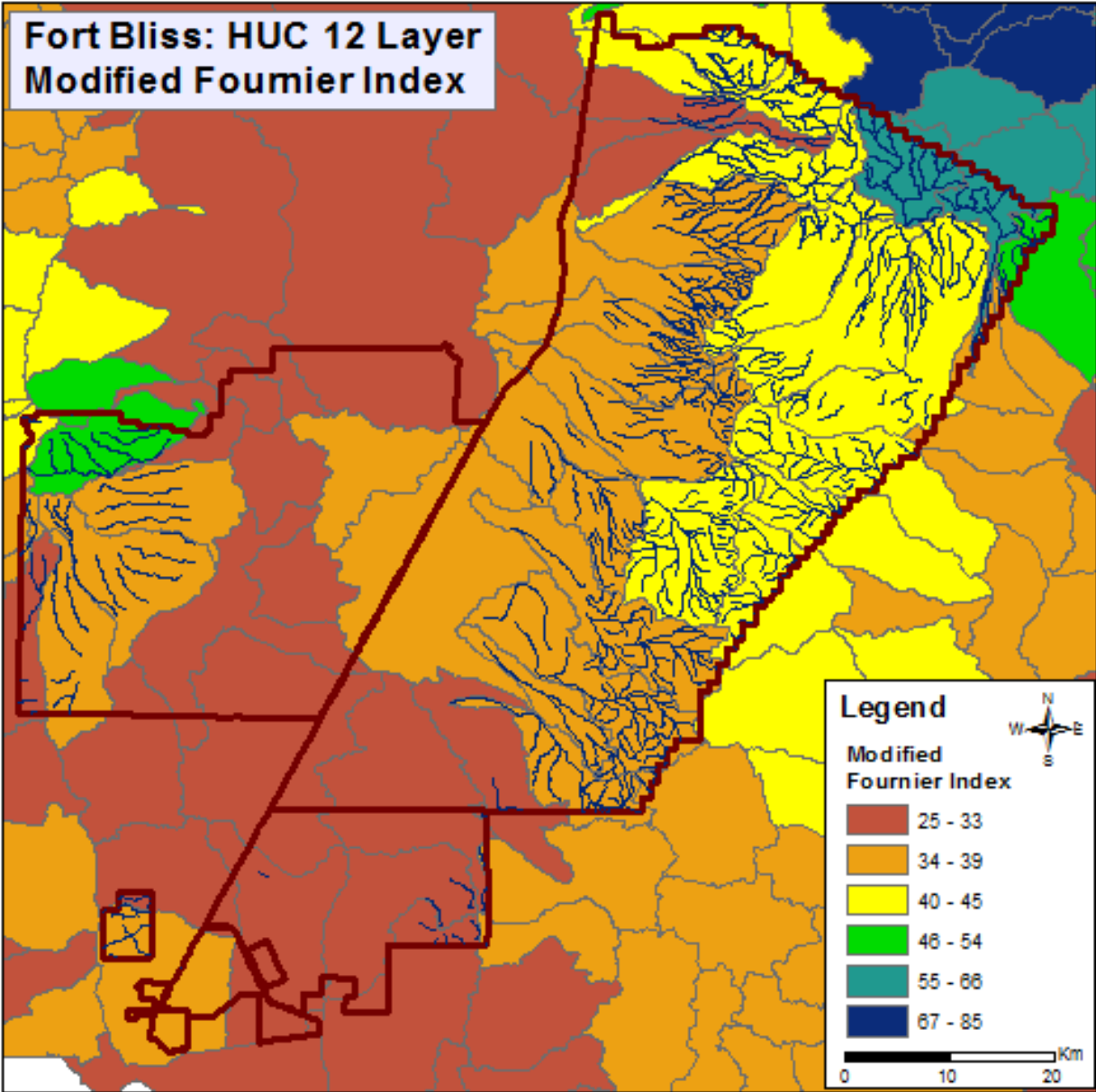
Fort Huachuca: Reach Layer
Unit Stream Power at Q10 (kW)

Legend

USP Q10 (kW)

0.03 - 0.15
0.16 - 0.30
0.31 - 0.50
0.51 - 0.80
0.81 - 1.20
1.21 - 2.07

Fort Huachuca: HUC 12 Layer
SW25yr2hr: Design Storm

Legend

SW25y2hr
Design Storm (mm)

52 - 58
59 - 62
63 - 66
67 - 71
72 - 78

Km
0   3   6

Fort Huachuca: Catchment Layer
Percent Slope

Legend

Percent Slope

0.00 - 0.03
0.04 - 0.06
0.07 - 0.10
0.11 - 0.15
0.16 - 0.20
0.21 - 0.30
0.31 - 0.40
0.41 - 0.61

Km
0   3   6

Fort Irwin: Reach Layer Discharge (cms)

Legend

Q50 (cms)

— 2 - 20
— 21 - 40
— 41 - 80
— 81 - 120
— 121 - 180
— 181 - 260
— 261 - 410

0   10   20
Km

Fort Irwin: HUC 12 Layer Drainage Density

Legend

Drainage Density

- 0.03 - 0.30
- 0.31 - 0.50
- 0.51 - 0.75
- 0.76 - 1.00
- 1.01 - 1.25
- 1.26 - 1.60

Fort Irwin: Catchment Layer Hydro Group

Legend

Hydro Group
A
B
C
C/D
D

Yuma Proving Grounds: Reach Layer 3m Inundation Width (m)

Yuma Proving Grounds: Catchment Layer KF Factor

Legend

KF Factor
0.00
0.01 - 0.25
0.26 - 0.35
0.36 - 0.45
0.46 - 0.55

0   10   20
Km

Yuma Proving Grounds:
HUC 12 Layer
Rainfall Seasonality

Legend
Rainfall Seasonality

■ 0.14		■ 0.17		■ 0.20	
■ 0.15		■ 0.18		■ 0.21	
■ 0.16		■ 0.19		■ 0.22	

0   10   20
Km